CYCLIC PITCH TURBINES

by

JUBILEE PRASAD RAO

A dissertation submitted to the

School of Graduate Studies

Rutgers, The State University of New Jersey

In partial fulfillment of the requirements

For the degree of

Doctor of Philosophy

Graduate Program in Mechanical and Aerospace Engineering

Written under the direction of

Prof. F. Javier Diez

And approved by

_____

_____

_____

_____

New Brunswick, New Jersey

October, 2018

ABSTRACT OF THE DISSERTATION

Cyclic Pitch Turbines

By JUBILEE PRASAD RAO

Dissertation Director:

Prof. F. Javier Diez

Vertical axis type wind turbines, which offer promising solutions for distributed power generation, have not received adequate attention due to technological drawbacks which need to be addressed. In the present work, a vertical axis drag based turbine is proposed that allows for an improved turbine performance by eliminating recovery stroke losses. This is achieved by optimizing the cyclic drag forces on its blades. The turbine's blades are flat plates; the projected area of which can be drastically varied by varying its pitch angle. To utilize this effect, the turbine blades pitch by 90° between the two turbine strokes manipulating their effective area using a novel cyclic blade pitching mechanism. This passive mechanism orients the blades vertically during the drive stroke for maximum effective area and horizontally during the recovery stroke for minimum effective area with respect to the fluid flow. These blade orientations maximize the positive drive stroke force and minimize the recovery stroke losses to allow for maximum net energy capture and an improved turbine performance. The turbine, owing to its blade movements is called the Cyclic Pitch

Turbine (CPT) and its working principle resembles that of an oar blade in the sport of shell rowing.

A theoretical model of the CPT turbine is developed to predict the performance and optimize the turbine parameters and it is validated using wind tunnel and water channel experiments. The turbine is self-starting at all turbine orientations and has a better and more uniform static torque coefficient than the popular Savonius turbine. The dynamic analysis also indicates a higher performance for CPT and the predicted values for torque and power coefficients match very closely with those from water channel and wind tunnel experiments on a fabricated prototype. Optimization of the turbine parameters is performed which clearly shows that, a shorter drive stroke ($\sim 140^{\circ}$) and a tip speed ratio value close to 0.5 results in optimal power generation. Several blade shapes are tested in the wind tunnel and the results indicate that airfoil section blades with long and narrow continuous shapes that have less area towards the blade's tip result in higher performance. This thesis stands as a proof of concept work on cyclic pitch turbines which can be used to efficiently harvest wind energy in residential areas and also hydro-kinetic energy from tides and river streams.

Acknowledgements

First and foremost I would like to thank God for giving me this opportunity, the strength and perseverance to be here today.

About four and a half years ago, Prof. Javier Diez took me in as a master's student and towards its end, encouraged me to pursue a Ph.D. by instilling confidence in me while I was not so sure. Through my interactions with him and opportunities and people that I was exposed to, as a result, have taught me and make me who I am today. He has been kind and supportive of my needs, ideas, and actions as a student. For this, I am very grateful to him.

I would also like to thank Prof. Cook Chennault, Dr. Arturo Villegas and especially Prof. Edward DeMauro for readily accepting to be part of my dissertation committee, being patient, supportive and giving their valued suggestions through the process. I appreciate and am thankful for the effort Prof. Edward DeMauro put into thoroughly reviewing and giving extensive comments to improve the quality of my dissertation. I would like to thank Prof. Xiaoli Bai and her students for allowing me to extensively use the wind tunnel in their laboratory. In addition, I would also like to thank the program director, Prof. Jerry Shan, program chair, Prof. Alberto Cuitino and professors for whom I worked as a teaching assistant. Special thanks to Prof. Haim Baruh for encouraging me with kind words and gestures.

I am also very thankful to my lab mates during the course of my research at Applied Fluids Lab at Rutgers University, including Dr. Arturo Villegas, Dr. Mena Tawfik, Dr. Marco Maia and Dr. Diego Ravell who have actively given very useful and key

inputs. I would like to thank Mr. Christopher Sacelaris, Mr. Diego Fung and Mr. Matthew Woodward who have helped and have been part of this research. I would also like to extend thanks to Mr. Rohan Paleja and all my lab mates.

Several student organizations have enriched my life at Rutgers during the course of the last five years including Rutgers fencing and salsa clubs, ICF and especially A-Life fellowship which lifted me up during the most difficult of times and made me realize that He(God) already has "Made A Way." I'm also grateful to my friends Rick Castellano, Mustafa Mozael, Ashish Alex and Melissa among many others for their encouragement and the many fun and rich experiences we had together. In all, I am very thankful to Rutgers University and the USA for the experiences I never could have dreamt of.

I am immensely grateful to my family members, especially my Dad who believed in me and supported me financially, emotionally and spiritually, my Mom and all my siblings who in their own way made it possible for me to be here. Chitty aunty, Julie uncle, and Vijju anna, Emily akka have always been there for me for which I am very grateful to them. I also want to thank Aria, who has been more than a friend to me and for sharing many life's experiences and its valuable lessons with me. I also want to acknowledge my love for my dogs and best friends Jacky and Jacksy and Jimbo.

Finally, I would like to acknowledge a small grant sponsored by the University Research Council Grant Program at Rutgers University towards this project.

Table of Contents

List of Tables

List of Figures

Chapter 1

Introduction

Energy is one of the most basic necessities for any form of life to exist. Different energy forms like thermal, electromagnetic, sound, gravitational, chemical, electric energy exist and each has its own function. Electric energy and the electric grid is a national security concern as the modern day human life depends on it for most if not all of our needs. Without electrical energy, we would be set back by a few hundred years. Power generation stations, small and large, exist all across the world working continuously to generate electricity for almost every human activity including communication, transportation, manufacturing, computing, banking, lighting, heating, and refrigeration. Such is the importance of energy in our lives and electric power has and is shaping our lives to extents more than necessary sometimes. In view of electric power being such a critical asset, every country tries to ensure a safe, reliable and continuous generation of electric power.

Electric power generation is carried on at different locations primarily through the use of fossil fuels like coal, natural gas, and nuclear fuel (EIA, 2017). Power generation plant capacities range from a colossal 22 GW, the Three Gorges Dam in China (Gleick, 2009), to as small as a few KW. Large power plants using fossil and nuclear fuels are known to release excessive amounts of harmful toxins into the atmosphere which include carbon dioxide, sulfur compounds, oxides of nitrogen and nuclear wastes among others (Demin, 2002), which have been polluting the Earth for several decades. In addition, these energy sources have large capital as well and running costs and are

expected to deplete in a few decades considering constant production rates (Singh & Singh, 2012). In view of such disadvantages associated with traditional energy sources, the solution lies with renewable energy sources.

Power generation using renewable energy sources has been a topic of utmost interest in recent years as a result of the aforementioned consequences like pollution, global warming, and others due to fossil fuel combustion and nuclear waste disposal. The major renewable energy sources are solar and wind which are harvested extensively using solar photovoltaic cells and wind turbines respectively. Though wind turbines have existed for many centuries and used in many applications, an increased interest and an exponential annual cumulative growth in them for power generation has been observed in the last two decades with global cumulative installed wind capacity increasing from 17 GW in 2000 to 432 GW in 2015 (GWEC, 2014). Wind turbines are also predicted to grow at an average of about 12% in the next few years (GWEC, 2014) and more renewable energy capacity is being added every year in the world than the net capacity additions due to new fossil fuel power plants (Adib *et al.*, 2015). Other renewable methods like energy harvesting from the movement of water in oceans and rivers have also been gaining a lot of attention due to the higher energy density of those resources as well as the very high level of predictability (Rourke *et al.*, 2010). And turbine designs similar to wind turbines are being used to harness energy from the tidal currents.

1.1 History of Wind Turbines

Wind energy has become one of the major and irreplaceable forms of renewable energy that is being harvested commercially across the World. The movement of air needed to produce wind energy is a result of differential heating of the Earth's surface by the Sun (Bianchi *et al.*, 2007) causing a pressure difference which drives the motion of air. Wind energy has been used by humans for centuries and it started as early as 5000 BC

to sailboats (Carter, 2006). Windmills came into existence around 1,700 BC (Moretti & Divone, 1986) to pump water and some vertical axis windmill designs were used to grind grain in the Middle East and Persia as shown in Fig. 1.1. Over the last few decades, windmills have been used to generate electrical power. The wind turbines capture and convert the kinetic energy available in wind to mechanical energy of rotating blades and then to electrical power using generators. The power generation capacities of these machines range from a few Watt which can be used to supplement a residential house's electric needs to a few mega Watt which are used commercially. The power output P, from a wind turbine mainly depends on parameters like swept area of the turbine$A$, air density ρ, wind velocity u, and its operational efficiency popularly known as the coefficient of power C_P as indicated in Eq. 1.1. Also, these turbines are used either as stand-alone systems or exist as wind farms where hundreds of large wind turbines are carefully placed considering wind direction and interactions between turbines. The energy generated from these wind farms is monitored by wind farm operators who maintain them and the necessary transmission systems.

$$P = \frac{1}{2} C_P \rho A u^3 \tag{1.1}$$

(a) (b)

Figure 1.1: Wind mills built 1000 years ago and still in use. Representation of wind energy usage for agricultural purposes. References: Howard (2017), Age of Empires pc game

1.2 Classification of Wind Turbines

Several wind turbine classifications (Kumar *et al.*, 2018) exist to differentiate the hundreds of wind turbine designs that exist today some of which are commercially available. Changes and upgrades to wind turbines like rotor size, blade profiles, control methodologies, etc. are performed to make them economically more appealing and energy efficient. These turbines also vary based on power generation capacity, rotor diameter, sensors onboard, hub height, blade pitch control among many other differences. The two major and the most general wind turbine classification (Tummala *et al.*, 2016) criteria are described below.

1.2.1 Based on Orientation of Turbine Axis

This most visually obvious distinction among wind turbines is the rotation axis of a turbines' blades. According to the orientation of the axis, wind turbines are classified as horizontal and vertical axis turbines (Bianchi *et al.*, 2007) as described below.

Horizontal axis wind turbines (HAWT)

In horizontal axis turbines, as shown in Fig. 1.2, the turbine blades are mounted on a tall support tower and rotate about a horizontal axis. The blades of the turbine rotate about a center hub while transmitting energy to a generator shaft which produces electric power. The power is then regulated to match that of the grid for either residential or commercial use. For commercial operations, these turbines are laid out in large wind farms in specific engineered layouts to maximize the farm's total energy production. These turbines are more popular than the vertical axis type turbines and are available for residential use as well as large-scale commercial use.

Figure 1.2: Horizontal axis wind turbines harvesting energy from the wind. Reference: publicdomainpictures.net

Vertical axis wind turbines (VAWT)

The vertical axis wind turbines are the second type and have their blades rotate about a vertical axis as seen in Darrieus turbine shown in 1.3. These are far less popular and exist only in smaller sizes and power generation capacities. Yet, they offer promising solutions for distributed generation away from integrated power grid systems (Bhutta *et al.*, 2012). These turbines also have several other advantages which include less noise, no need for a yawing mechanism, being independent of wind direction, small ground height and others (Bhutta *et al.*, 2012) which make them well suited for residential locations including buildings rooftops. Also, VAWT turbines like Savonius are less affected by turbulence in the air flow and can be packed much closer to each other, unlike horizontal axis wind turbines which are affected by the turbulence from the turbine in front of it.

Figure 1.3: A vertical axis Darrieus "egg beater" type wind turbine. Reference: wind-turbine-models.com

1.2.2 Based on Utilized Forces

According to the second type of classification, wind turbines are divided as lift based turbines and drag based turbines (Schubel & Crossley, 2012). This classification is based on the type of force that the turbines utilize to generate the necessary torque to rotate the turbine blades.

Lift based wind turbines

Lift based wind turbines use lifting forces developed by air flowing over specifically shaped blade sections to generate the required torque. A HAWT turbine which is lift based and the principle involved in lift force generation are depicted in Fig. 1.4. All the horizontal axis wind turbines (HAWT) (Hau, 2006) and some vertical axis wind turbines (VAWT) (Ragheb, 2011) like Darrius are lift based and have airfoil shaped blade cross sections (Schubel & Crossley, 2012), (Mohamed, 2012). The used airfoils range widely from 4 and 6 digit NACA series (Abbott *et al.*, 1945) to more recent DU airfoils developed at the Delft University in Netherlands (Timmer & Van Rooij, 2003). These turbines rotate and generate electric power when sufficient wind velocity is available.

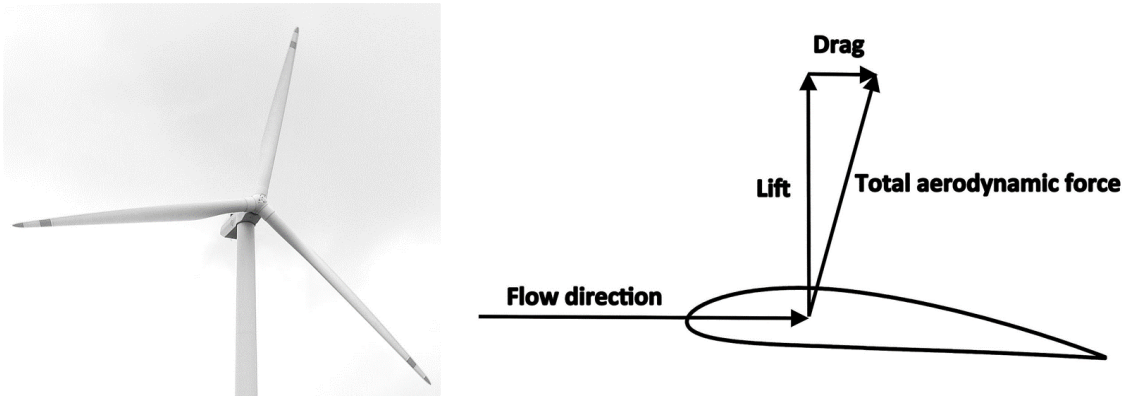

Figure 1.4: A lift based turbine and an illustration of lift force generation across an airfoil blade section. Reference: Wikipedia

Drag based wind turbines

Drag-based turbines, on the other hand, use drag forces developed by resisting airflow motion (Gasch & Twele, 2012) to generate the required blade torque. An example of a drag based turbine and drag force generation on its blades is depicted in Fig. 1.5. A few small-scale turbines like the one depicted, Savonius among a few others use drag force to produce electric power or sometimes even to pump water for energy storage.

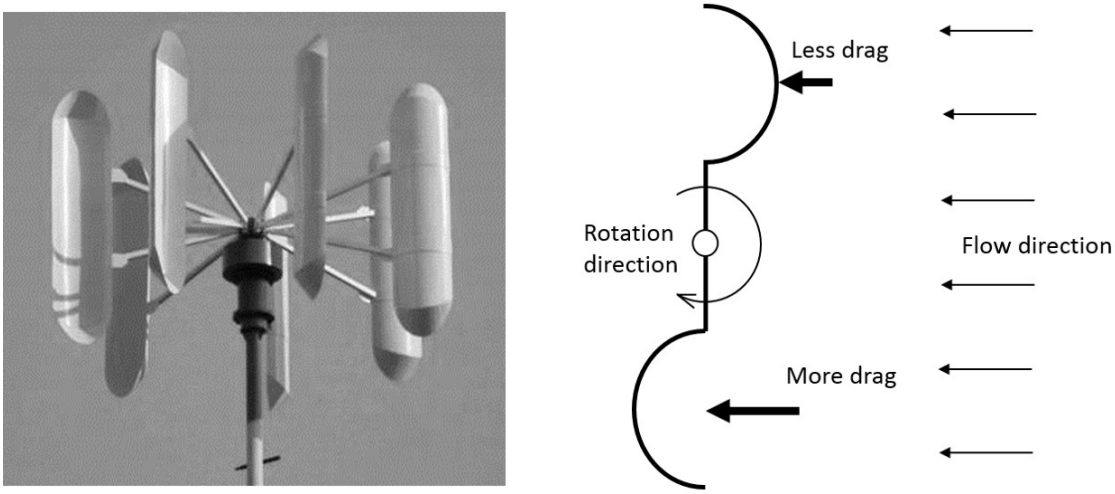

Figure 1.5: A drag based wind turbine and an illustration depicting the forces acting on its blades during operation. Reference: twinkletoesengineering.info

1.3 Savonius Turbine

Savonius turbine (Savonius, 1931) is the most popular vertical axis drag based turbine (Deb *et al.*, 2014). The turbine rotates about a vertical axis and used mostly in residential areas with rated capacities usually less than 2kW (Kang *et al.*, 2014). The turbine is invented by S.J. Savonius in 1922. A typical Savonius turbine has two concave/x buckets with an 'S' shaped cross section looking from the top. The concave shape of its blades causes it to experience a positive drag force in the downwind direction. When the same bucket is observed from the opposite direction, it has a

convex form which results in an adverse negative drag in the upwind direction. The drag coefficient of the concave shape is larger than that for the convex shape and leads to a higher positive drag force than the adverse negative force. This differential drag force causes a net torque in the direction of rotation of the turbine as illustrated in Fig. 1.6. Several Savonius designs with structural modifications exist (Tang *et al.*, 2013) with varying design complexity and performance implications.

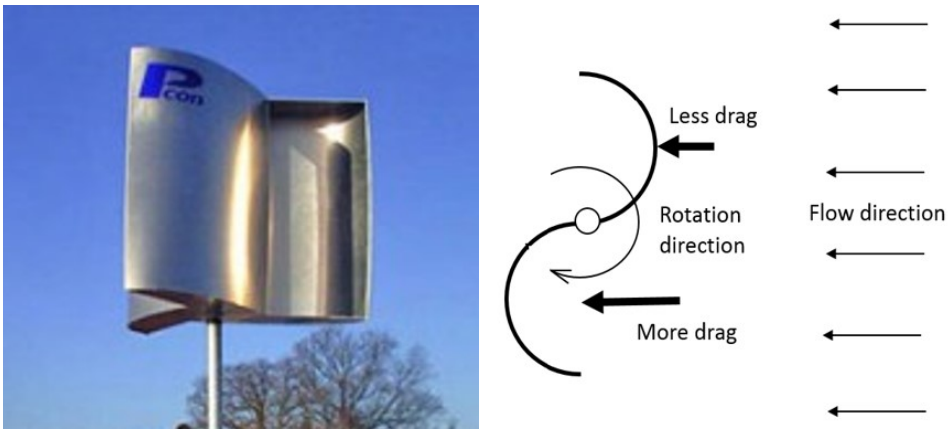

(a) (b)

Figure 1.6: Savonius turbine installed on a roof top and an illustration indicating the its principle of operation. Reference: Tummala *et al.* (2016)

1.3.1 Advantages of Savonius

Savonius turbines have many advantages due to their simplicity in design and vertical orientation. Due to its simple design, they are easier and less expensive to construct and assemble (Ricci *et al.*, 2016). They are also cheaper to maintain as a result. They can also be used to harness energy from water flow in rivers, tides, etc. It is a self-starting turbine (DAlessandro *et al.*, 2010) and does not need a motor to initialize rotation as observed in other vertical axis turbines like Darrieus turbine, a lift based turbine, with poor self-starting capabilities (Kumar *et al.*, 2017), (Sharma *et al.*, 2013). The blade shape also allows the turbine to operate independently of wind direction (Akwa *et al.*, 2012). The direction of rotation stays the same even

when the wind flows in an opposite direction which makes power generation simpler. The effect of turbulence, which is a norm in urban environments, on drag turbines like Savonius is also found to be very low (Ricci *et al.*, 2016) compared to that of horizontal axis or lift based wind turbines. As a result, Savonius turbines can be closely packed together without much loss in energy output. As an added benefit, when the wind direction is known, proper spacing and orientation of Savonius turbines can lead to increased performance (Sun *et al.*, 2012). Savonius turbines are also known for their high starting and operating torques. These are less noisy and rotate at lower rotational speeds when compared to horizontal axis turbines.

Savonius turbine enjoys additional benefits of being a vertical axis wind turbine. The turbines are at easily accessible heights and do not need very tall towers. These can be used on tall buildings to make use of roof space. The gearbox and generator of a Savonius turbine are on the ground unlike for horizontal axis turbines which have them at hub height. This allows for easy access and inexpensive maintenance of the machines when necessary. The various advantages of a Savonius turbine are:

- Simplicity in design
- Easy and less expensive construction
- Self-starting and operate even at low wind speeds
- Wind direction independent operation
- Low turbulence effects on performance
- Higher packing density
- Easy access to gearbox and generator
- Easy maintenance
- Low turbine speed and low noise pollution
- High torque generation

1.3.2 Drawbacks of Savonius

Despite several advantages, there exist a few areas where the Savonius turbine can be improved upon. One of the biggest drawbacks is the existence of adverse drag force on the turbine blades during the recovery stroke. As shown in Eq. 1.2, the net positive drag force, F_D on the blades at any instant is the difference between the positive drive stroke drag force, F_d and the adverse recovery stroke drag force, F_r on the blades/buckets. The final goal for any drag based wind turbine including Savonius turbine is to maximize the net positive drag force F_D by maximizing the drive stroke drag force F_d and minimizing, if not eliminating, the recovery stroke drag force F_r (Golecha *et al.*, 2011). Lower net positive force translates to a lower torque, lower power output and consequently a lower coefficient of power for the turbine. Also, the forces, either drag or lift forces, acting on an object are proportional to the relative velocity between the incoming fluid and the rotating blades. When the blades start to rotate faster, the relative velocity between the upstream blade reduces while that for the downstream blade increases. This effect lowers the positive drag force and increases the negative drag force which ultimately adversely affects the coefficient of power, C_P of the turbine as shown in Fig. 1.7 from wind tunnel experiments done on a 2 blade Savonius turbine (Hayashi *et al.*, 2005). The plot shows that the efficiency of a Savonius turbine drops very quickly with an increase in tip speed ratio, λ (Ragheb & Ragheb, 2011), a non-dimensional turbine parameter given by Eq. 3.24 at wind speeds varying from 6 m/s to 18 m/s.

$$F_D = F_d - F_r \tag{1.2}$$

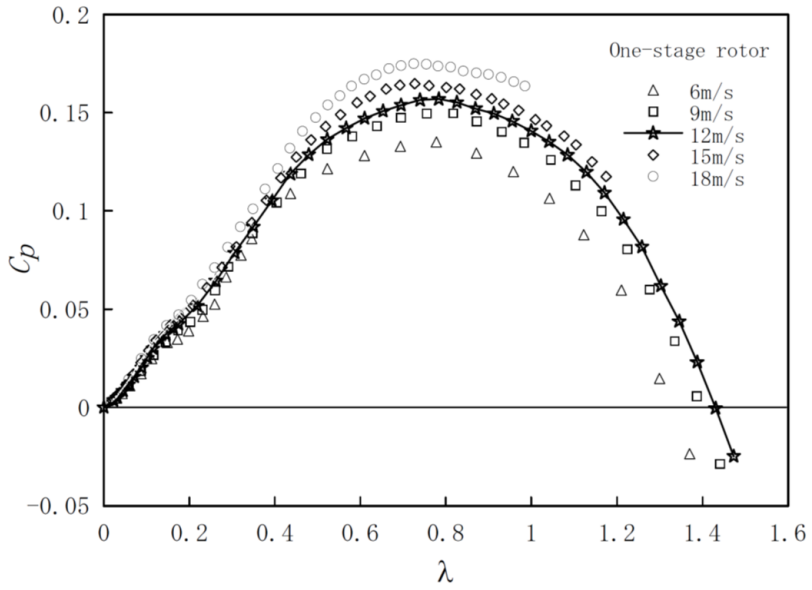

Figure 1.7: Coefficient of power for a 2 bladed Savonius turbine from wind tunnel experiments. Reference: Hayashi *et al.* (2005)

Another drawback in Savonius turbines is its variation in the torque coefficient which changes significantly in each cycle as the blades of the turbine rotate about a vertical axis (Hayashi *et al.*, 2005). The static torque coefficient is a non-dimensional measure of the torque generated by the turbine when the turbine is kept stationary at any specific turbine blade location around the turbine axis. At some blade orientations with respect to the wind flow (azimuth angles), very small and even slightly negative static torque coefficient values are also observed. In wind tunnel experiments conducted on a 2 bladed Savonius, in one rotation cycle, at different azimuth angles given by α, a maximum coefficient of static torque value of close to 0.4 and a minimum value of negative 0.1 was observed. This drastic variation can be attributed, also to the recovery stroke drag. A solution suggested for such variations is using multiple stages of Savonius, one on top of another which are symmetrically offset by azimuth angle. For example, Hayashi *et al.* (2005) showed that, when three stages are used, the wind tunnel experiments showed a drastic reduction in the static torque coefficient, C_{ts}

variation as shown in Fig. 1.8 compared to a single stage Savonius turbine. A three-stage Savonius turbine implies having three individual Savonius turbines connected and lying one on top of another and offset by a certain angle.

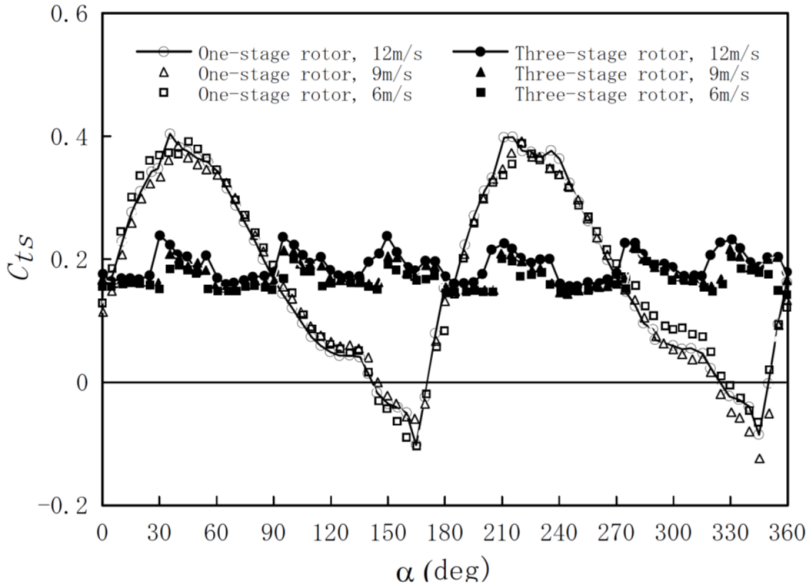

Figure 1.8: Variation of static torque coefficient for a 2 bladed Savonius turbine and compared to a 3 stage Savonius. Reference: Hayashi *et al.* (2005)

The present work aims to minimize the recovery stroke losses and optimize the blade working cycle by maximizing positive drag while simultaneously minimizing adverse drag, thus increasing the power output and turbine efficiency.

1.3.3 Modifications to Savonius

Modifications to the Savonius turbine and several variations to its blades are investigated by several researchers in the past through experiments, numerical investigations (Roy & Saha, 2013) and CFD simulations to improve the turbines performance. Some of the approaches used were, to use helical buckets that have slanted buckets instead of straight buckets (Kamoji *et al.*, 2009), use elliptical shaped blades (Kacprzak *et al.*, 2013), use end plates on top and bottom of the buckets (Mohamed *et al.*, 2010), have

vertical slotted buckets (Alaimo *et al.*, 2013), change the number of buckets on the turbine (Wenehenubun *et al.*, 2015), have a central intersection swirling chamber between the buckets (Al-Faruk & Sharifian, 2016), change the aspect ratio, which is the ratio of height of the buckets to its diameter, among several others. These methods attempted to find the best Savonius configuration but did not directly attempt to reduce the recovery stroke drag which is a cause for its low efficiency. Some of the approaches to reduce recovery stroke drag were to use deflector plates to shield returning blade (Mohamed *et al.*, 2010), (Golecha *et al.*, 2011) or use a curtain design which involves two plates in front of the Savonius turbine to direct air flowing onto the returning bucket onto the bucket undergoing drive stroke (Altan *et al.*, 2008). Both designs improved the performance and eliminated the negative starting torque observed at some azimuth angles. Yet, the turbine design became more complex as the deflector plate adds more parts to the complete design. The design also makes the turbines dependent on wind direction requiring the deflector plate to be placed in front of the turbine. Instead of using a deflector plate, a second Savonius turbine was placed in close proximity to the first Savonius to observe the interactions and coupling effects (Sun *et al.*, 2012) through numerical simulations. Particle image velocimetry (PIV) technique is also used to observe the time and phase-averaged flow fields and to determine the effects of using two closely spaced Savonius turbines (Shigetomi *et al.*, 2011) compared to a lone Savonius turbine. Even though some configurations of the Savonius pair resulted in slightly better performance, similar to the deflector plate, the performance is highly dependent on the wind direction. Another design uses buckets with several flaps which swing open while in the return stroke to let air pass through during the recovery stroke and reduce adverse drag (Alaimo *et al.*, 2013) which resulted in undesirable inertial effects of moving parts at high speeds while also significantly increasing the complexity in design. Multiple stages of Savonius (Hayashi *et al.*, 2005) were experimentally tested in a wind tunnel mainly to minimize the cyclic variations in the static torque coefficients and eliminate negative

values associated, at a few azimuth angles as discussed in previous sections. Some hybrid designs which combine Savonius with a Darrius a lift based turbine, have also been studied to reach a compromise between high torque drag turbine and high powered lift turbine respectively (MacPhee & Beyene, 2012). The hybrid designs include Darrieus and Savonius built one inside of the other (Freeman, 2012), (Gavalda *et al.*, 1990) or as a two-stage system with one fixed on top of another (Gupta *et al.*, 2008). These works improved the performance slightly but failed to minimize the recovery stroke drag or did so with major limitations to the Savonius design.

1.3.4 Other Turbine Designs

To circumvent the limitations seen in Savonius, some novel vertical axis wind turbines based on drag forces are developed and investigated as well. These turbines (Weiss, 2010) , (Cooper & Kennedy, 2004) have flat, almost flat or airfoil section blades which rotate about a vertical blade axis different from the turbine rotation axis. They use chain or belt drives to connect the driven shaft to the blades to rotate the blades. This complicates the design for construction. Also, the blade rotation and the rotation rate are constrained by the chain/belt drive and give no leeway for optimization of the blade pitch rates or timing. In addition to these limitations, these turbines do not completely eliminate the recovery stroke drag as the blades are feathered (completely passive) at only one azimuth angle during their recovery stroke. As a result, some negative drag is being generated at all other azimuth angles during the recovery stroke. Additionally, the drive stroke is also loosing on energy generation. Another flat plate turbine (Muller *et al.*, 2009) for use on building roof edges utilizes the walls of the building to shield the blades in the recovery stroke. It works only for one wind-direction and requires a sturdy and large structure to redirect the air into the turbine.

1.4 Proposed Solution

Multiple vertical axis turbine designs and alterations to the existing Savonius turbine have unsuccessfully attempted to eliminate recovery stroke losses, as described in section 1.3.3 and 1.3.4. A novel vertical axis turbine, which uses flat plate blades as illustrated in 1.9, is proposed that aims at completely eliminating the recovery drag through the use of a blade pitching mechanism. It is called "Cyclic Pitch Turbine" (CPT) owing to the pitching motion of the blades which happens twice for every turbine rotation cycle. The three blades of the turbine, as indicated in the figure, are at different stages of a rotation cycle, one blade is absorbing energy by maximizing its frontal area with respect to the wind flow. This stroke can be termed as the drive stroke. A second blade on the opposite side of the turbine is projecting minimal frontal area resulting in minimum drag possible. This stroke is termed as the recovery stroke where the blades are passive. The third blade in between the two mentioned blades is undergoing a pitch change, transitioning from a drive stroke to a recovery stroke. The blade shape indicated in the picture is not necessarily the most optimal one but shown as a representation. The overall principle utilized by the turbine is to project maximum area to generate maximum driving force during the drive stroke and then use the pitch mechanism to pitch the blades to achieve minimum possible projected area to eliminate adverse drag force during the recovery stroke (Rao & Diez, 2015).

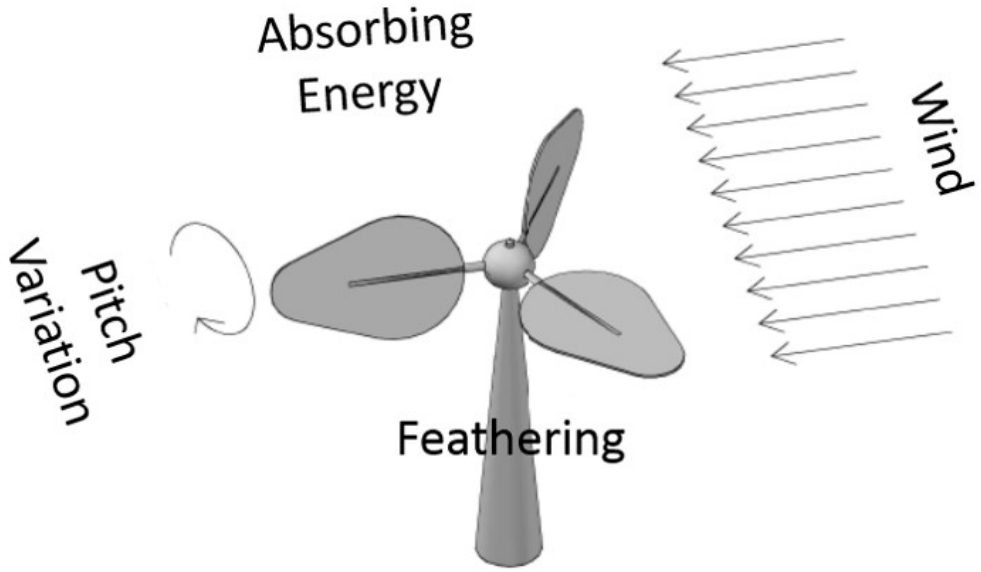

Figure 1.9: Illustration of the working principle and the different blade stages of a model cyclic pitch turbine.

1.5 Inspiration

Variations of the principle utilized by the proposed turbine to harness energy from a fluid flow can be observed in very old sports like shell rowing and kayaking. The motion of the oar or paddle blade in water and air resemble the turbine blade motions and is described in more detail below. A similar principle is also observed in nature in bird flight and specifically in the flapping of birds' wings.

1.5.1 Kayaking

In the sport of kayaking, the motion of a kayak paddle in the water to generate propulsive force resembles the drive stroke for the suggested cyclic pitch turbine. The kayak paddle has two blades at the two ends of a shaft which are used to propel, turn or stop a kayak. The different strokes of the paddle performed by a kayaker to propel a kayak forward are indicated in order in Fig. 1.10. At the beginning of the drive stroke, one of the blades of a paddle is pierced into the water in front of the kayaker. Then it is pulled back while pushing the water onto the back of the kayak. This motion is repeated alternatively on right and left sides and it produces a drag force onto the kayak's blade which transmits through the shaft of the paddle, into the hands of the kayaker to push the kayak forward. Drag force is the primary mechanism used to generated the propulsive force. The drag force on the paddle is caused as a result of the kayaker moving the paddle's blade in the water and causing a relative motion between the usually stationary water and the paddle blade. The drag force is proportional to the blade area and varies according to the cosine of the yaw and pitch angle of a blade (Sumner *et al.*, 2003) with respect to the water and also the relative velocity between the blade and the water. When one of the two blades is being used to push the water back, the other oar is lifted out of the water and follows oppositely, the motion of the other blade since the paddle shaft is solid. Even though the other blade is undergoing an opposite motion, it does not counteract and nullify the drag force of the blade in water because the drag force generated by the blade in the water is much much higher than that generated by the blade in the air. This is because, the drag force F_D is proportional to the density, ρ of the medium as indicated in Eq. 1.3 and the density of water is higher and more precisely 1000 times to that of air. The equation also shows that the drag coefficient of the blade oar, C_D, the projected area of the blade, A and the square of the relative velocity u between the fluid and the blade oar are directly proportional to the total drag force on an object.

$$F_D = \frac{1}{2} C_D \rho A u^2 \tag{1.3}$$

Figure 1.10: Series of movements of a kayak paddle needed to propel a kayak forward. Reference: https://youtu.be/vrwz8UhkX4Q

During normal kayak operation, a kayak's blade is always oriented perpendicular to the water surface as shown in Fig. 1.11. The figure shows the two blades on either side of the shaft in a rest state. It also shows a sweep stroke which is used to rotate and change the direction of a kayak. This is achieved by a circular motion of the kayak's blade from far front to the back end of the kayak while it is held perpendicular to the water surface to have maximum drag effect. This sweeping motion more closely resembles the rotary motion seen in the CPT turbine as indicated in 1.9

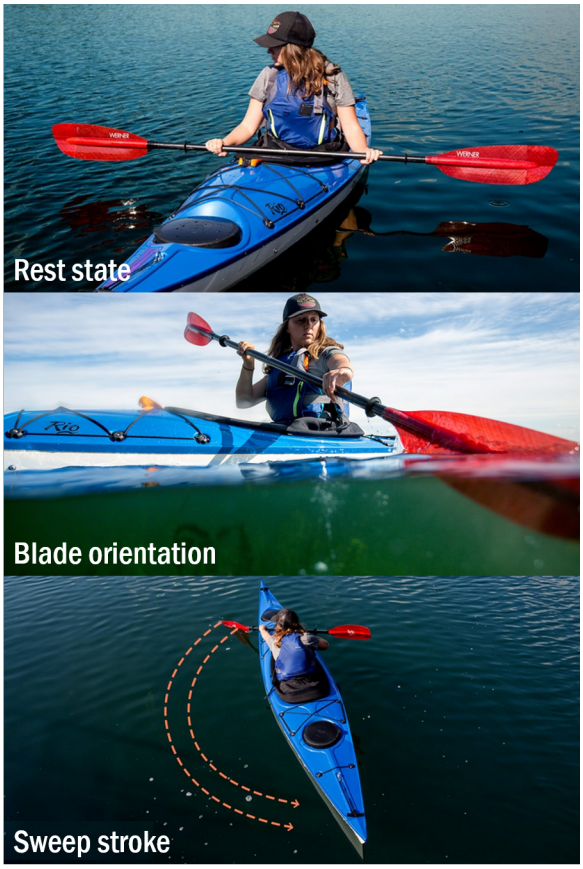

Figure 1.11: Photorgraphs showing a kayak paddle during rest state, its orientation before a drive stroke and the path followed by the blade during a sweep stroke. Reference: rei.com

1.5.2 Shell Rowing

The sport of shell rowing indicates a closer similarity to the cyclic pitch turbine's blade movements. Each oar used in rowing only has one blade at the end of a shaft compared to two blades seen in kayak's paddle. The other end of the oar ends in the hands of a crew member rowing the shell. In order to propel the shell/boat forward, a blade is squared/ oriented perpendicular to the water surface and used to push the water back which is called the drive stroke. Similar to the reaction observed in kayaking, the drag force on the blades pushes the shell forward. Then the oar's blade is brought out of the water and since the other end of the oar does not have a blade,

the second stroke includes bringing the oar's blade back to its initial position. This can be done while the blade is oriented in the same perpendicular orientation to the water surface and it would still create a net positive propulsive force because the density of water is much higher and results in a higher force while in water than in air as mentioned in the above section 1.5.1. Yet, in order to increase aerodynamic efficiency, the oar's blade is pitched by 90° and feathered as seen in Fig. 1.12 so that the relative motion between the blade and the air does not cause a negative drag on the oar blade and a loss in net propulsive force. This too follows the principle stated through the drag force equation that the drag force is proportional to the frontal area of the blade. And by tilting the blade from being perpendicular to being parallel, the frontal area is drastically reduced.

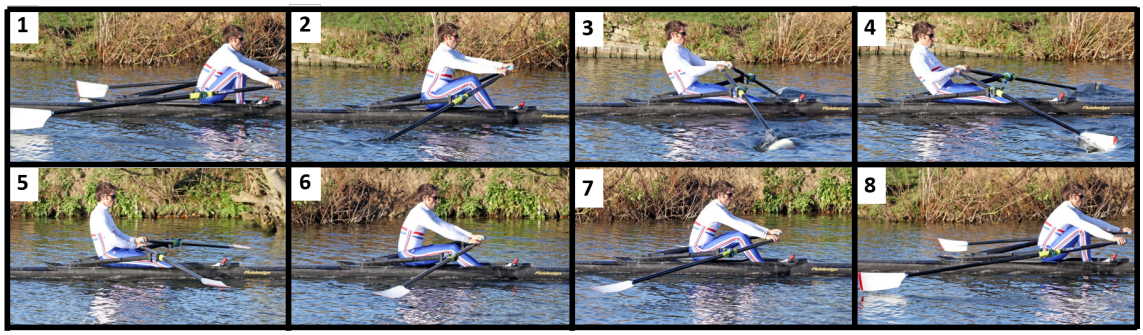

Figure 1.12: The sequence of oar blade orientations and movements involved in the sport of shell rowing to move forward. Reference: www.britishrowing.org

The orientation of an oar blade during the drive and the recovery strokes are depicted in Fig. 1.13. The oar blade is perpendicular to the water surface projecting maximum area to the flow of water to create maximum drag force during the drive stroke. At the end of the drive stroke, the blade is brought out from underwater, pitched by 90° and is held parallel to the water surface projecting minimum area and consequently minimum air drag during the recovery stroke. Oarsmen practice and perfect this elegant and complex rowing technique of pitching/rolling an oar to the right angles and at the right times to maximize their performance by achieving high mean boat speeds (Caplan & Gardner, 2007).

Figure 1.13: The vertical and horizontal orientations of an oar blade in water and air during the drive and the recovery strokes respectively in the sport of shell rowing. Reference: www.britishrowing.org

1.5.3 Bird Flight

A similar principle is also observed in nature in the flapping of the wings in some birds. In bird flight, there is no change in the medium of the fluid as opposed to the cases with kayaking and rowing where both air and water are involved. When a bird is performing flapping flight, the most obvious wing motions observed are the up-stroke and down-stroke of the wings. During the down-stroke birds spread their wings to exercise maximum wing area which produces the maximum lift. And before the wings transition into the up-stroke, which is analogous to the recovery stroke, to bring the wings back to their initial position, the bird folds the wings inwards to reduce the downward drag as seen in small birds like sparrows, finches, etc. (Brown, 1963). Folding in of the wings reduces the effective wing area and thus minimize lift loss during this recovery stroke.

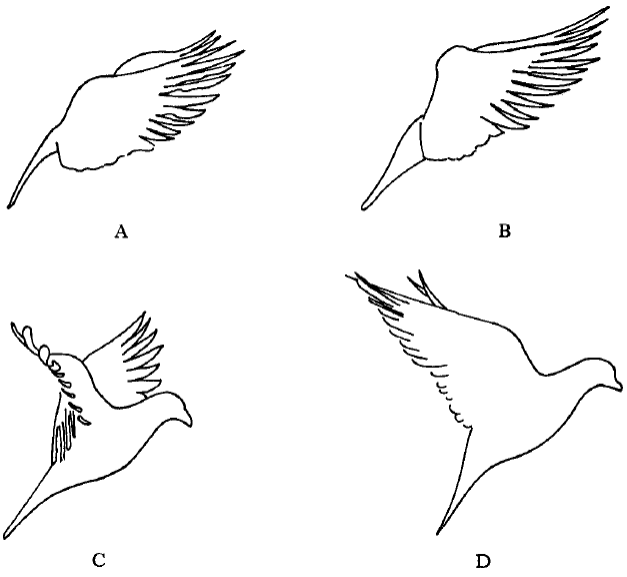

Figure 1.14: The folding and pitching movements of pigeon's wings during flapping flight. Reference: Brown (1963)

The three examples indicated above which include, pitching and folding of wings in birds, the motion of paddle in kayaking and the rolling maneuvers seen in shell rowing are examples where the area of the active control surface is being manipulated with respect to the relative velocity between the surface and the fluid flow. This change in effective area between the two strokes increases net lift for birds and generates a higher net thrust for rowing. And in both cases, changing the effective area of the blade between strokes improves performance and efficiency. The proposed cyclic pitch turbine uses the same principle and optimizes the drive and recovery stroke blade forces resulting in maximum net positive force as indicated through Eq. 1.2, to harnesses energy efficiently from a fluid flow.

Chapter 2

Cyclic Pitch Turbine Concept

2.1 Conceptualization

The proposed novel fluid turbine harnesses energy from fluid motion using principles similar to shell rowing and bird flight. Despite the similarities, they differ due to the fact that the aforementioned examples are techniques used to generate thrust or lift and not to capture the energy available in fluid flow. The principle of the proposed turbine is to have a simple yet smart design that takes advantage of the variation in drag force on a body as a result of pitching/ rolling the body and use it to efficiently harness energy from a fluid flow. The blades of the turbine always remain in the same medium either air or water for the complete cycle and it is critical that the recovery stroke needs to entail the least possible drag force to achieve maximum efficiency. In the following sections, the working principle and the mechanism necessary to achieve the cyclic blade pitching are introduced.

2.1.1 Drag on a Flat Plate

The drag force is the frictional resistance to relative motion between a body and a surrounding fluid and is given by Eq. 1.3. The equation says that the resistance drag force is proportional to the square of the relative velocity, projected/ effective area (Sadraey, 2009) and density of the fluid medium. Also the coefficient of drag term, C_D indicates that the drag force also depends on the shape of the object being considered.

For a flat plate, which is the blade shape being considered, the drag coefficient changes when the blade pitches resulting in a change in the effective frontal area. The change in drag coefficient can be ascribed instead to the pitch angle, also called the angle of attack of the flat plate (Ortiz *et al.*, 2012) as shown through experiments in Fig. 2.1. In the plot, C_D, C_L and C_S refer to the coefficients of drag, lift and span-wise forces on a flat plate tested in a wind tunnel.

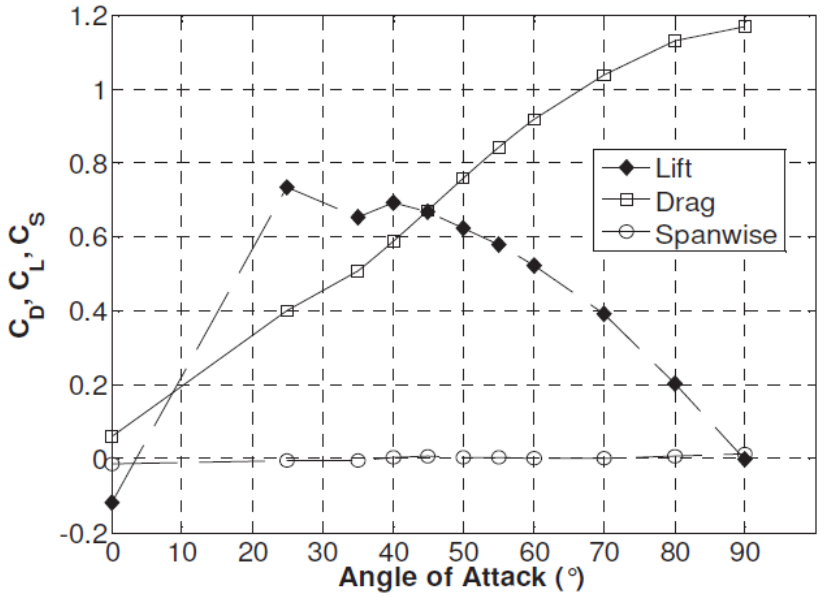

Figure 2.1: Experimental results showing variation of coefficient of drag and lift for a flat plate while angle of attack is increased from 0° to 90°. Reference: Ortiz *et al.* (2012)

Vertical orientation

A flat plate is said to be in a vertical orientation when the angle of attack is 90°. The analytical solution, as well as the empirical data, shows that the drag force on a flat plate is the highest and close to a value of 1.2 (Ortiz *et al.*, 2012), (Munson *et al.*, 1998) for vertical orientations with respect to the fluid flow as shown in Fig. 2.1.

Horizontal orientation

A flat plate is said to be parallel to the flow or in a horizontal orientation when the angle of attack is at its lowest value of 0°. The drag coefficient, then is very close to zero (Mueller & Torres, 2001), (Ortiz *et al.*, 2012) as seen in Fig. 2.1 and can be considered negligible when compared to the maximum drag force possible obtained at 90°. The drag force on a flat plate parallel to the flow is caused by the negligible thickness of the blade which manifests itself as the frontal area and due to shear forces acting over the surface of the flat plate on either side of it. The drag coefficient, C_D due to the shear force for a laminar flow on a smooth plate depends on the Reynolds number Re and is given by the Blasius solution shown in Eq. 2.1 (Cengel & Ghajar, 2011) which when calculated, turns out to be about 1% of the vertical orientation drag coefficient. Disturbances in free stream flow can affect the drag forces, but they are impossible to quantify and are not considered in the analysis.

$$C_D = 1.328 Re^{-\frac{1}{2}} \tag{2.1}$$

2.1.2 Linear Actuation

The orientation of a flat plate with respect to the flow changes the drag coefficient and consequently the drag force acting on it. This variation in drag force is used to harness energy by changing the orientation of a flat plate appropriately and allowing it to move back and forth in a laminar flow field. Assume a vertically oriented flat plate of finite length l and thickness t where $l \gg t$ being pushed from left to right in a steady laminar fluid flow as shown in Fig. 2.2 between t_1 and t_3 through a distance d. And the same plate pitches by 90° at t_4, attains a horizontal orientation and retraces the path back to its initial position as shown in Fig. 2.2 between t_5

and t_7. One complete cycle is achieved when the plate, at t_8, pitches again by 90° to attain its initial orientation and position. This is analogous to the cycle followed by an oar blade in rowing. As mentioned above, for a flat plate, like an oar blade, the drag force is maximum, F_{max} when the plate is vertical for $t_1 - t_3$ positions and it is minimum, F_{min} when the plate is horizontal for $t_4 - t_7$ as indicated in Fig. 2.2. A simple linear energy harnessing device, with a flat plate, harnesses energy while the plate is vertical and is being pushed from t_1 to t_4 and this can be termed as the drive stroke. And it uses a very small portion of that energy to trace back the same path from t_5 to t_8, termed as the recovery stroke, in a horizontal orientation to attain its initial position as illustrated in Fig. 2.2. During the drive stroke, since the drag force, F_{max} is maximum, maximum energy W_1, given by Eq. 2.2 is harnessed and during the recovery stroke, since F_{min} is the smallest possible force, minimum energy possible W_2, given by 2.3 is spent to attain its initial position. It is clear through the above analysis, that $W_1 \gg W_2$ and that the net amount of energy, W_{net}, given by Eq. 2.4, is the maximum energy that can be harnessed in each such cycle. And this cycle repeats itself over and over again to continuously harness energy efficiently from the fluid flow. Yet, the linear to and fro mechanism requires quick reversals in the direction of motion of the plate at t_3 and t_7 as illustrated in Fig. 2.2 which may necessitate a complex mechanisms. It might also lead to a loss of momentum and/or uneven power output variations.

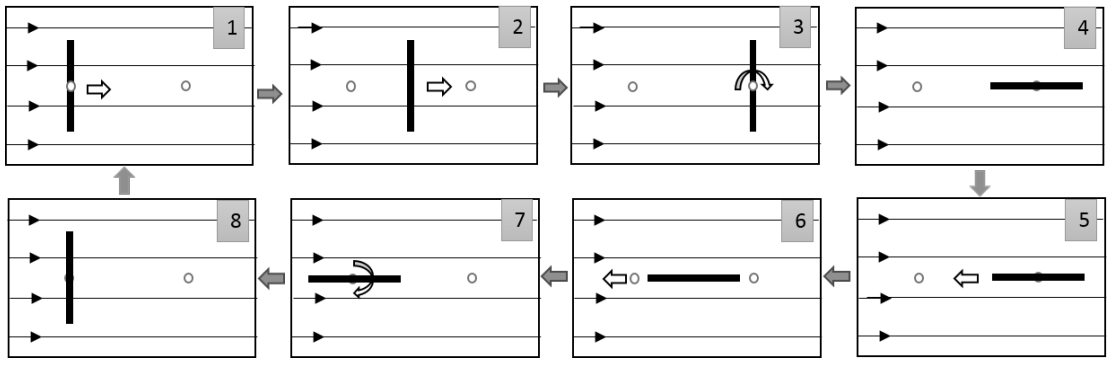

Figure 2.2: Sketch showing the sequence of movements and orientations experienced by a flat plate in one cycle to harness energy from fluid flow.

$$W_1 = F_{max} \cdot d \tag{2.2}$$

$$W_2 = F_{min} \cdot d \tag{2.3}$$

$$W_{net} = W_1 - W_2 \tag{2.4}$$

2.1.3 Rotary Actuation

The linear mechanism of the flat plate can be modified into a rotary design, typical of wind turbines, as shown in Fig. 2.3 to achieve a very similar result. The rotary mechanism has the advantage that the direction of rotation is continuous while providing a smooth pitching motion and power generation. For the rotary system, the plate is vertically oriented and rotates in the flow direction (downstream) for 180° about the turbine rotation axis which is the drive stroke. The plate then, pitches by 90° and with a horizontal orientation rotates and moves into the flow (upstream) for the remaining 180° of one rotation cycle which forms the recovery stroke. The flat plate again pitches by 90° to attain the initial orientation to complete one complete turbine cycle.

The two strokes of a rotary cycle are shown in Fig. 2.3(b) separated by a separation plane. Transitioning from the drive stroke to the recovery stroke and vice-versa in the rotary system is analogous to reversing the direction of motion of a blade in a linear system discussed in 2.1. Also, similar to the linear cycle, the rotary cycle involves

two 90° blade pitching motions per cycle, one at the end of each stroke as shown in Fig. 2.3(a), one in between t_1 and t_2 and the second one in between t_5 and t_6. As a result of the cyclic pitching motion of the turbine blades, the turbine is named as the "Cyclic Pitch Turbine". A model of the turbine, its different blade orientations, and the working principle are shown in fig: 2.4.

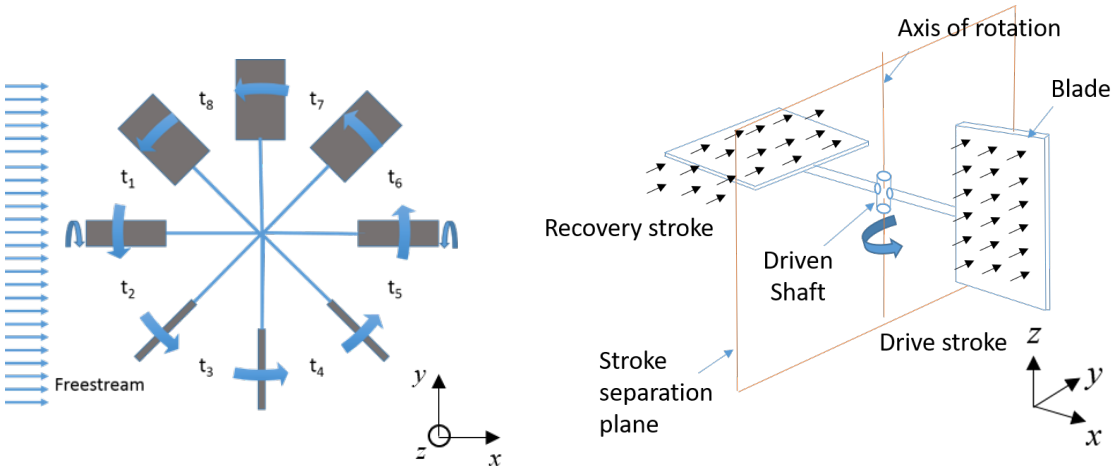

(a) (b)

Figure 2.3: Sketch of a cyclic pitch turbine in top view showing the different blade orientations and an isometric sketch showing the drive stroke and recovery stroke blade orientations.

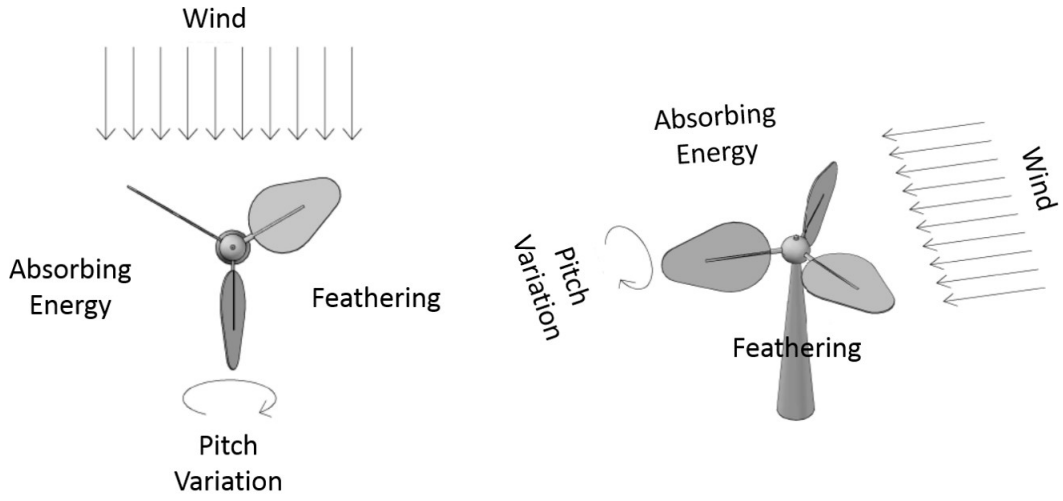

(a) (b)

Figure 2.4: Top and isometric view illustrations of a model CPT turbine describing its working principle.

2.2 Blade Pitching Mechanisms

The pitching motion of the blades that happens twice every turbine rotation cycle can be achieved easily using active systems as observed in large HAWTs. These large HAWTs use hydraulic or electro-mechanical devices located in the turbine hub to change the pitch angle of the blades through a gear system (Wu *et al.*, 2011). This is done to limit the turbine power generation to rated values at higher wind speeds and to feather the blades for maintenance and in severe weather conditions. For the proposed solution, it is not desirable to increase the complexity and also, a readily usable mechanism is not available. Hence, a customized mechanism called "dual cam mechanism" which is passive and can be tuned to optimize turbine performance is developed. This mechanism is a combination of several existing mechanisms like swash plates observed in helicopters and cams seen in automotive engines and automation industry.

2.2.1 Swash Plate

A swash plate indicated in Fig. 2.5 has some similarities to the proposed rotary cyclic pitch motion. It is used in helicopters to regulate its blade's pitch, for flight control, by converting linear input from the pilot into a rotary output. The output is a continuous pitch variation of the helicopter blades spread uniformly over 360° of rotation about the rotation center. The difference between what is required and the swash plate's output is that the swash plate mechanism produces a continuous pitch variation, while the proposed turbine requires two discontinuous and quick 90° rotations when the blade changes from upstream to downstream position and vice versa (i.e. between t_1 - t_2 and between t_5 - t_6 in Fig. 2.3). To produce these quick rotations, a mechanism that holds the blade in vertical and horizontal positions during the drive and recovery strokes respectively and rotates them quickly and smoothly

by 90° in between the two strokes is required.

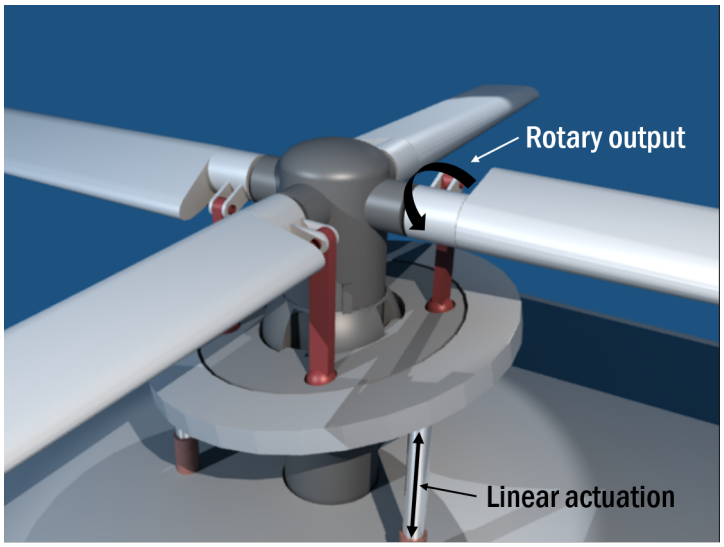

Figure 2.5: A model of a swashplate, used in helicopters, uses linear actuation to pitch its blades for attitude control. Reference: Wikimedia

2.2.2 End Cams

End cams are a category cam mechanisms which are usually seen in internal combustion engines to convert the rotary input into a linear output. End cams have a hollow cylindrical form with the contact surface on one edge of the cylinder. The contact edge is smoothly raised at some locations more than others. When the cylindrical end cam rotates about its center axis, a roller/follower moves up and down on the edge. End cams are not commonly used due to the cost and complexity in manufacturing the contour (Zhang *et al.*, 2006). An end cam follower pair is depicted in 2.6. There also exist cylindrical cams where a roller follower follows a groove on the outer surface of a cylinder as also shown in the figure.

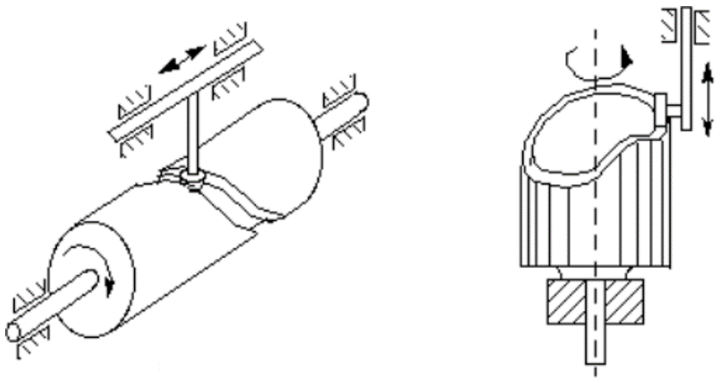

Figure 2.6: Cylindrical cam and an end cam showing rotary follower input motion and the resulting translating follower output motion. Reference: Zhang *et al.* (2006)

The followers commonly observed in cam-follower mechanism undergo either oscillating or translating motion. The blades of the turbine will be mounted onto the ends of the follower and are required to rotate by 90° at the end of each stroke. Hence, the available followers are not directly suitable for our application and require some modifications.

2.2.3 Gear Drives

Gear systems are also a probable solution wherein a rotary input results in a rotary output at increased or reduced speeds. For the proposed turbine, since two 90° rotations of the blades are required for each rotation of the turbine itself, we would require a 4:1 gear ratio. Still, it does not suffice to use a gear train since gears output smooth and continuous rotations. This will lead to reduced drive stroke drag and increased adverse drag as the blades will not hold a specific (90° during drive stroke and 0° during recovery stroke) angle during its operation. And hence a gear train, similar to swashplate and cam mechanisms fall short of delivering the right blade motions required by the CPT turbine and a custom mechanism is needed which is developed in the following section.

2.3 Proposed "Dual Cam Mechanism"

A mechanism called the "Dual Cam Mechanism" is developed to generate the necessary blade motion. The mechanism converts the rotary motion of the turbine into controlled pitching motion of the follower-arms at specified angular locations on the fixed cams. The mechanism has two concentric end cams and the operation principle is explained by using one cam and one follower first.

2.3.1 Cams and Followers

A cam has an elevated surface and a lower surface with a sharp rise and a sharp fall between the two surfaces as shown in Fig. 2.7. The follower for the mechanism has a lobe and it is shown to start on the lower surface in the figure. It slides on the lower surface until it reaches the ridge (rise in cam surface) where it acts like a mechanical switch and rotates by 90° about the follower shaft axis. The follower moves onto the elevated surface and holds that angle until it travels through the entire elevated surface as shown in Fig. 2.7. The follower then needs to rotate again by 90° (total 180° which is similar to 0° orientation for a flat plate) to operate continuously in cycles.

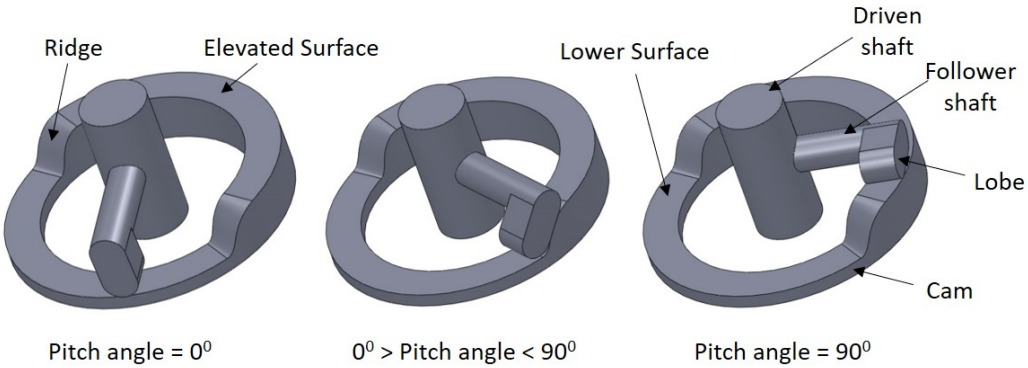

Figure 2.7: Cam and follower models showing three sequential locations and the resulting pitch angles of a follower with respect to the cam surface describing the pitching mechanism.

Continuous operation of the mechanism is achieved by adding a second cam and its own follower lobe that rotates the follower arm again by another 90°. Also, since the followers are rotating continuously in the same direction, each follower requires another lobe opposite to the first on both cams to continue pitching motions. The result is a dual cam mechanism with two concentric end cams facing the same direction with each cam having one follower with two opposite lobes as shown in Fig. 2.8. A follower arm in total has 4 lobes and three of the lobes are active at any given time and are in contact with the cam surfaces while one lobe is facing away from the cams.

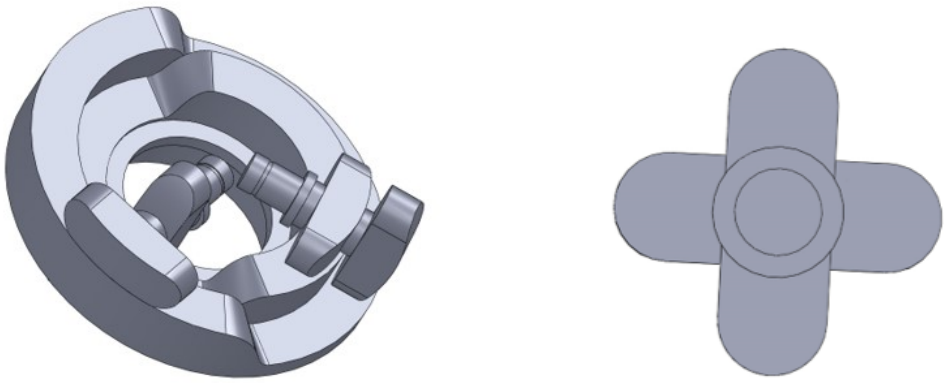

(a) (b)

Figure 2.8: Model of a dual cam mechanism with two pairs of followers at opposite orientations and the four lobed follower which provide blade pitching motion for the CPT turbine.

The two cam surfaces, if they face the same direction, the blades rotate progressively in the same direction and if they face opposite directions, the blades rotate back and forth between 0° and 90°. The cams facing the same direction is selected for the present design. Also, it should be noticed that the second cam is out of phase with respect to the first cam by 180°. And consequently, the follower of the second cam extending from the first follower is out of phase with respect to the first one by 90°. The 180° offset between the cams and the 90° offset between the followers make the elevated surface on the first cam exactly coincide with the lowered surface on the

second cam and vice versa which allows the two followers to roll without interference. This mechanism holds the turbine blades vertical for the first 180° during the drive stroke, pitches them by 90° when the followers move across a ridge, holds the blades parallel to the flow during the recovery stroke for the remaining 180° before pitching them again by 90° when the followers hit the second ridge to attain the initial position and orientation of the blades. These 4 blade and follower motions are depicted in Fig. 2.9

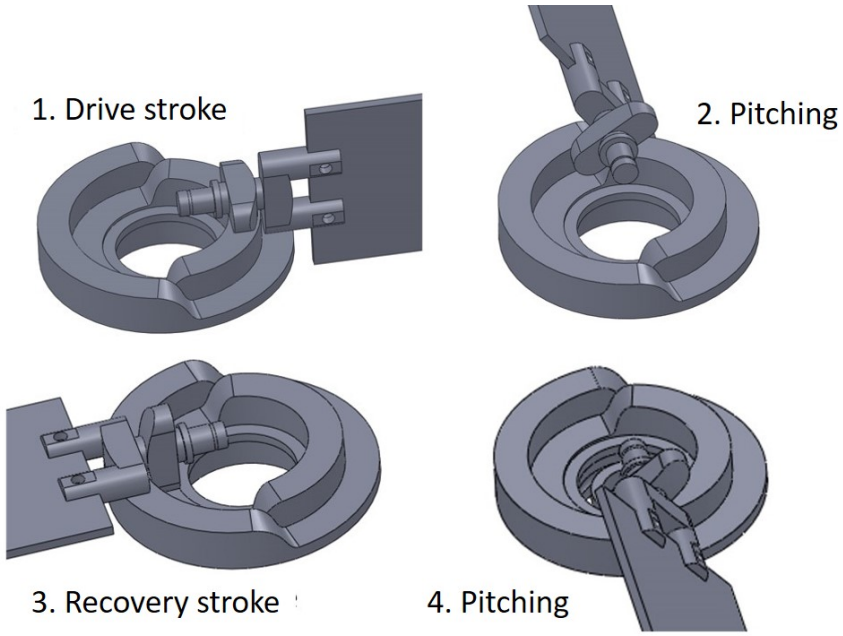

Figure 2.9: CPT model depicting the four different phases of the turbine blade and the attached follower arm.

2.3.2 Central Hub

The central hub holds the three followers in place and equidistant from each other as shown in Fig. 2.10 and is located at the center of the cams. The central hub rotates along with the followers and absorbs energy from all the three blades. In addition, the followers also rotate inside the hub on a bearing while the blades pitch. The central hub rotates freely about the turbine axis on a bearing located on the inner cam surface and transmits power to a coupled driven shaft.

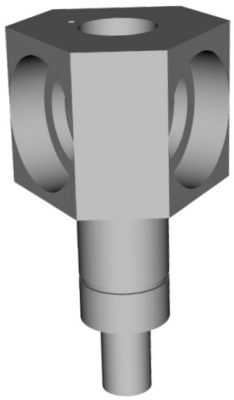

Figure 2.10: Model of central hub of the CPT turbine to which all the blades forces are transmitted.

2.4 Assembly

All the parts that make up the cyclic pitch turbine, including the central hub, dual cams, followers and turbine blades are assembled together as shown in Fig. 2.11. The central hub-cap shown in figure and C-clips on the follower shafts prevent the followers from coming out loose from the hub. A C-clip on the central hub's shaft prevents the central hub from being detached from the cams. The central hub extends into a driven shaft at the bottom of the assembly which can be connected to a generator to convert fluid motion energy into electric power.

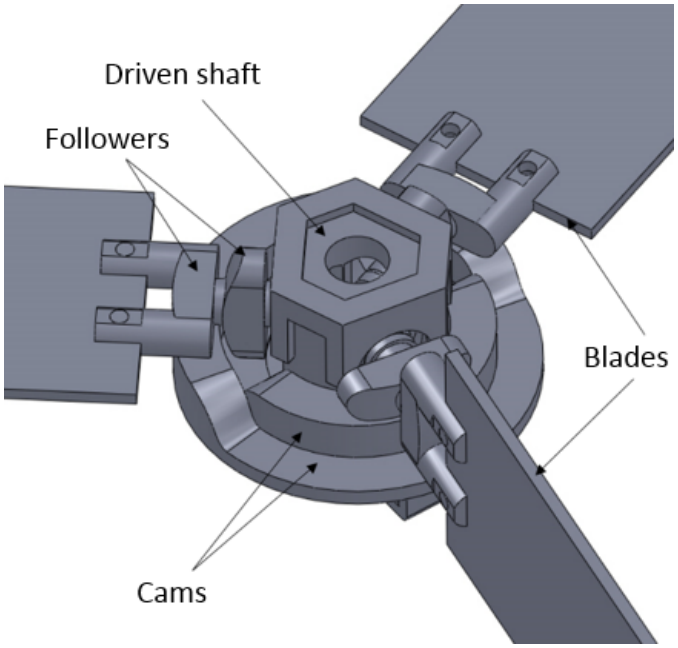

Figure 2.11: Assembly of the CPT turbine model indicating the different parts.

Chapter 3

Theoretical Formulation

Theoretical models to predict the performance of drag based turbines are not available due to the complex, turbulent and transient flow around vertical axis turbines. At the same time, such models for lift based turbines are widely available. Blade element theory is simple and popularly used technique to predict HAWT performance (Ingram, 2005). It considers the momentum balance and the lift and drag force equations to determine the coefficient of power, C_P of the turbine.

3.1 Modelling

An analytical approach at predicting the performance of the cyclic pitch turbine to model the turbine's static and dynamic characteristics is proposed. Force, torque and power outputs from each blade are determined from which turbine's coefficient of torque and power are calculated by analyzing blade forces. The cyclic pitch turbine is then optimized based on parameters like turbine speed, pitching location, stroke duration etc.

The turbine blade is represented by a thin flat plate with square edges for the analysis which extends from the turbine rotation axis to its maximum blade length, R. The velocity diagram of a cyclic pitch turbine blade during a drive stroke is shown in top view by Fig. 3.1. The figure shows the components of the relative velocity between the flow and the turbine blade. The free stream velocity u is split into radial, u_r,

and normal, u_n, velocity components with respect to the blade. The turbine blade is positioned at an azimuth angle of θ with respect to the location where the blade surface is exactly perpendicular to the flow. The blade is assumed is be rotating at a constant angular velocity, ω and the tangential force on the blade acting on the blade is given by F. The analysis assumes the azimuth angle to be 0° when one of the three blades is perpendicular to the free stream as shown in Fig: 3.2 and it increments in the counter clockwise direction.

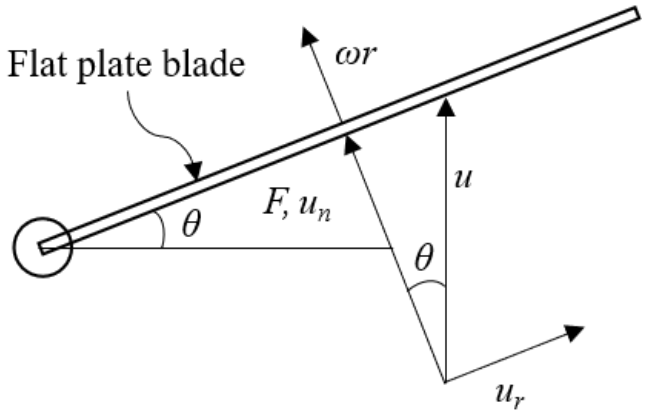

Figure 3.1: Relative velocity diagram between the blade and the free stream flow indicating the normal and radial components of fluid velocity and the normal force on the turbine blade.

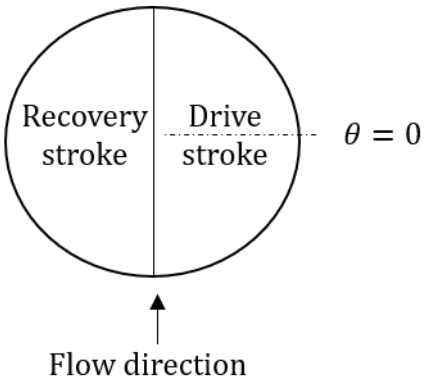

Figure 3.2: Illustration indicating the drive and recovery strokes and the location of the reference zero degree azimuth angle shown from a top view orientation.

3.2 Static Analysis

Static analysis of the turbine sheds light on the blades forces and torque generated by the turbine while it is in a braked condition or when sufficient wind is not available for operation. The static characteristics of the proposed cyclic pitch turbine are also compared to that of the most popular drag turbine, Savonius, mentioned in section 1.3.

3.2.1 Relative Velocity

For a static condition, the angular velocity of the turbine, ω is zero. As a result, the relative velocity between the fluid motion and the turbine blade at azimuth angle θ are given by Eq. 3.1. The relative radial velocity along the blade is given by u_r and the relative normal velocity which is of more significance is indicated as u_n. It shows that, in such cases, the relative velocities are a function of only the free stream velocity and the blade location with respect to the fluid motion.

$$\begin{aligned} u_r &= u \sin\theta \\ u_n &= u \cos\theta \end{aligned} \tag{3.1}$$

And the dynamic pressure q, a measure of the available kinetic energy in the fluid, of density ρ and moving at a velocity u, per unit volume is given by Eq. 3.2.

$$q = \frac{1}{2}\rho u^2 \tag{3.2}$$

3.2.2 Blade Forces

The drag force on a flat plate in a fluid flow depends on the drag coefficient C_D which is close to 1.2 (Ortiz *et al.*, 2012), (Nedić *et al.*, 2013), (Munson *et al.*, 1998) for an angle of attack of 90° for Reynolds number ranging from 1.0×10^4 to 1.0×10^7. At the same time, the drag coefficient for a typical Savonius bucket is 2.3 during a drive stroke (concave) and 1.2 during the recovery stroke (convex) (Lindsey, 1938), (Sadraey, 2009). The total drag force, F can be calculated for any object including the flat plate during its drive stroke by using Eq. 3.3 where A refers to the blade area, ρ is the density of fluid and u_n is the relative normal velocity between the object and the free stream. This is the force that acts on the blade perpendicular to its surface which directly aids in the rotation of the blades and consequently the turbine. This equation holds for all azimuth angles ranging from $-90°$ to $+90°$. And during the recovery stroke which ranges from $+90°$ to $+270°$ azimuth angles, the blade is assumed to precisely hold its horizontal orientation for which the adverse drag force coefficient is very close to zero (Ortiz *et al.*, 2012), (Mueller & Torres, 2001) and hence the recovery stroke force is considered to be zero. At those angles, the blade is parallel to the flow causing negligibly small effective area. Also, the shear drag on the blade surface is insignificant and can be ignored as indicated in 2.1.1 when compared to the pressure drag (Kundu *et al.*, 2009) in the drive stroke.

$$F = \frac{1}{2} C_D \rho A u_n^2 \tag{3.3}$$

The equation updates to Eq. 3.4 when the equations for the area of the blade and relative normal velocity are substituted as blade width H, blade length R, and azimuth angle θ.

$$F = \frac{1}{2} C_D \rho R H u^2 \cos^2 \theta \tag{3.4}$$

3.2.3 Torque Output

From the force equation, the torque T due to a turbine blade can be calculated by multiplying the total force F by half the radius of the turbine blade as shown in 3.5. Since the blade is not moving, the drag force is equally distributed across the blade area and the resultant force acts at the center of the blade located at $R/2$ units away from the turbine's center axis.

$$\begin{aligned} T &= F \frac{R}{2} \\ T &= \frac{1}{4} C_d \rho R^2 H u^2 \cos^2 \theta \end{aligned} \tag{3.5}$$

3.2.4 Coefficient of Static Torque

Static torque coefficient, C_{TS} of a turbine is an indication of starting characteristics (Ali, 2013) and determines whether or not a turbine starts to rotate on its own when sufficient fluid motion is available. The static torque coefficient is dependent for a vertical axis turbine on the azimuth angle, θ. At some azimuth locations, it could have negative values as well, as discussed for Savonius turbine which indicated that the turbine tries to rotate in the opposite direction for a given wind direction. The static torque coefficient for the cyclic pitch turbine is then calculated using the total torque by dividing the total product of dynamic pressure and the blade area as shown in Eq. 3.6. Since the turbine is not rotating, the work done is zero and therefore no power is generated and marks the end of the static analysis. It needs to be noted that

the above analysis pertains to a single blade and the turbine level parameters can be calculated by adding the forces or torques for all the blades of the turbine.

$$C_{TS} = \frac{T}{qA}$$
$$C_{TS} = \frac{2T}{\rho H R u^2} \tag{3.6}$$

3.3 Dynamic Analysis

Dynamic analysis, as the name indicates, involves the prediction of cyclic pitch turbine performance while the blades rotate and harness positive power from the fluid motion. The magnitude of the force acting on the turbine blades and as a result, torque output and power output vary between the static and dynamic analysis and is described in sections below.

3.3.1 Relative Velocity

The difference between the static and dynamic analysis is the changing relative normal velocity as the blades start to move. Relative normal velocity component between the turbine blade and the fluid motion varies considerably as we move from the root of the blade to its tip. The radial component u_r and normal component u_n of relative velocities are given by Eq. 3.7 for a given fluid free stream velocity of u. The angular velocity of the blade, ω is not equal to zero and is held constant, indicating that the turbine rotates at fixed speeds irrespective of the location of the blades. It shows that the normal component of relative velocity is maximum at the root of the turbine blade and reduces as we move towards the blade tip. This affects the blade forces and the consequent parameters as well.

$$u_r = u \sin\theta$$
$$u_n = u \cos\theta - \omega r \tag{3.7}$$

3.3.2 Blade Forces

The total blade force cannot be calculated using the drag force equation directly since the normal relative velocity is changing along the blade length. Hence the drag force dF on an infinitesimal blade element as indicated in Fig. 3.3 of thickness dr at a distance of r units from the turbine center axis at an azimuth angle θ is calculated using Eq. 3.8. The area of the infinitesimal blade element is given by the product of element thickness dr and the constant width of the blade H. Drag coefficient, C_D for a vertical plate is observed to remain constant for a wide range of Reynolds numbers (Nedić *et al.*, 2013) and the same is considered true for all radial locations of the CPT blade.

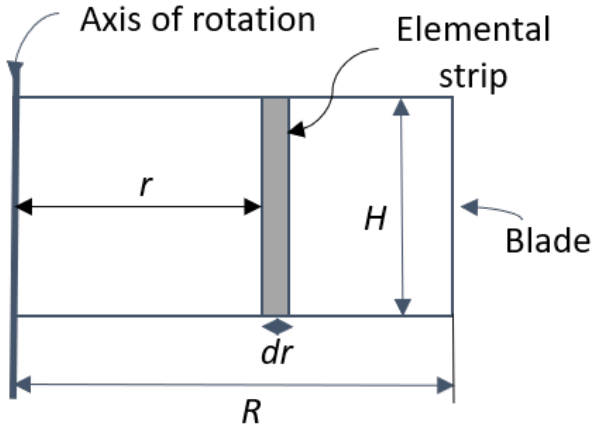

Figure 3.3: An infinitesimally thin vertical section of the cyclic pitch turbine's blade considered for analysis.

$$\begin{aligned} dF &= \frac{1}{2} C_D \rho dA u_n^2 \\ dF &= \frac{1}{2} C_D \rho H (u\cos\theta - r\omega)^2 dr \end{aligned} \tag{3.8}$$

The total instantaneous force, F, acting on the whole blade at a given azimuth angle, θ, is obtained by substituting the relevant terms and integrating dF over the entire length of the blade from its root to its tip at a distance R units from turbine axis as shown in Eq. 3.9 and Eq. 3.10.

$$\begin{aligned} F &= \int_0^R dF \\ F &= \frac{1}{2} C_D \rho H \int_0^R (u\cos\theta - r\omega)^2 dr \end{aligned} \tag{3.9}$$

$$\begin{aligned} F &= \frac{1}{2} C_D \rho H \int_0^R (u^2\cos^2\theta - 2\cos\theta r\omega + r^2\omega^2) \\ F &= \frac{1}{2} C_D \rho H (u^2 R\cos^2\theta - u\omega R^2\cos\theta + \frac{\omega^2 R^3}{3}) \end{aligned} \tag{3.10}$$

3.3.3 Torque Output

The infinitesimal torque generated by the force on a blade element on the turbine can be calculated using 3.11 similar to that in static analysis.

$$\begin{aligned} dT &= dF\frac{r}{2} \\ dT &= \frac{1}{2} C_D \rho H (u\cos\theta - r\omega)^2 r dr \end{aligned} \tag{3.11}$$

Using the infinitesimal torque equations, and integrating them from the root of the

blade to its tip, the total instantaneous torque is calculated as shown in Eq. 3.12 and Eq. 3.13

$$\begin{aligned} T &= \int_0^R dT \\ T &= \frac{1}{2} C_D \rho H \int_0^R (u\cos\theta - r\omega)^2 r dr \end{aligned} \tag{3.12}$$

$$\begin{aligned} T &= \frac{1}{2} C_D \rho H \int_0^R (u^2 r\cos^2\theta - 2\cos\theta r^2\omega + r^3\omega^2) \\ T &= \frac{1}{2} C_D \rho H (u^2 \frac{\omega R^2}{2}\cos^2\theta - \frac{2\omega^2 R^3}{3} u\cos\theta + \frac{\omega^3 R^4}{4}) \end{aligned} \tag{3.13}$$

3.3.4 Coefficient of Torque

The coefficient of torque or the dynamic torque coefficient C_T is then calculated using the total torque generated by a blade as shown in Eq. 3.14

$$\begin{aligned} C_T &= \frac{T}{qA} \\ C_T &= \frac{2T}{\rho H R u^2} \end{aligned} \tag{3.14}$$

3.3.5 Power Output

Instantaneous power output

The infinitesimal instantaneous power output generated by a blade element is calculated by multiplying the torque output by the angular velocity ω as shown in Eq. 3.15.

$$\begin{aligned} dP &= dT\omega \\ dP &= \frac{1}{2}C_D\rho H(u\cos\theta - r\omega)^2 r\omega dr \end{aligned} \tag{3.15}$$

Instantaneous power output from a whole blade is obtained similarly by integrating over the entire radial length of the blade from radius $r = 0$ to $r = R$ as given by Eq. 3.16 and Eq. 3.17. It can be noticed that Eq. 3.17 is the same as Eq. 3.13 multiplied by angular velocity ω. This is due to the fact that ω is set to be constant and does not affect integration.

$$\begin{aligned} P &= \int_0^R dP \\ P &= \frac{1}{2}C_D\rho\omega H\int_0^R (u\cos\theta - r\omega)^2 r dr \end{aligned} \tag{3.16}$$

$$\begin{aligned} P &= \frac{1}{2}C_D\rho H\int_0^R (u^2\omega r\cos^2\theta - 2\omega^2 r^2 u\cos\theta + \omega^3 r^3)dr \\ P &= \frac{1}{2}C_D\rho H(u^2\frac{\omega R^2}{2}\cos^2\theta - \frac{2\omega^2 R^3}{3}u\cos\theta + \frac{\omega^3 R^4}{4}) \end{aligned} \tag{3.17}$$

Average power output

The average power output from a cyclic pitch turbine blade for one whole rotation is obtained from instantaneous power output by integration over the azimuth angle from $\theta = 0^\circ$ to $\theta = 360^\circ$. This entire rotation is split into the drive stroke (θ from $\frac{-\pi}{2}$ to $\frac{\pi}{2}$) and recovery stroke (θ from $\frac{\pi}{2}$ to $\frac{3\pi}{2}$) as shown in Eq. 3.18

$$P_{avg} = \frac{1}{2\pi}(\int_{\frac{-\pi}{2}}^{\frac{\pi}{2}} P d\theta + \int_{\frac{\pi}{2}}^{\frac{3\pi}{2}} P d\theta) \tag{3.18}$$

And, the second term in Eq. 3.18 corresponds to the recovery stroke where the drag force, torque and consequently power output according to our assumption is considered zero and the equation reduces to Eq. 3.19

$$P_{avg} = \frac{1}{2\pi}(\int_{\frac{-\pi}{2}}^{\frac{\pi}{2}} P d\theta) \tag{3.19}$$

Substituting instantaneous power integrals equation derived earlier from Eq. 3.16 we get Eq. 3.20 and Eq. 3.21.

$$P_{avg} = \frac{1}{2\pi}(\int_{\frac{-\pi}{2}}^{\frac{\pi}{2}} \int_{0}^{R} dP d\theta) \tag{3.20}$$

$$\begin{aligned} P_{avg} &= \frac{1}{4\pi} C_D \rho H (\int_{\frac{-\pi}{2}}^{\frac{\pi}{2}} \int_{0}^{R} (u\cos\theta - r\omega)^2 r dr d\theta) \\ P_{avg} &= \frac{1}{4\pi} C_D \rho H (\int_{\frac{-\pi}{2}}^{\frac{\pi}{2}} (u^2 \frac{\omega R^2}{2} \cos^2\theta - \frac{2\omega^2 R^3}{3} u\cos\theta + \frac{\omega^3 R^4}{4}) d\theta) \end{aligned} \tag{3.21}$$

Finally solving the integral over the drive stroke azimuth angles, we obtain Eq. 3.22 which is for average power output for cyclic pitch turbine that has only one blade.

$$P_{avg} = \frac{1}{4\pi} C_D \rho H (u^2 \frac{\omega R^2}{4}\pi - u\frac{4\omega^2 R^3}{3} + \frac{\omega^3 R^4}{4}\pi) \tag{3.22}$$

3.3.6 Coefficient of Power

The coefficient of power C_P is a non-dimensional parameter used to indicate turbine efficiency (Trevor, 2017), whose maximum value is limited theoretically by Betz limit of 59.26% (Ragheb, 2014). It is calculated by dividing the average power output of a turbine by the total power available in the fluid motion for the specific blade area, A as shown in Eq. 3.23. It is also equal to the product of tip speed ratio of the turbine λ (the non-dimensional relative velocity term for the blade speed), and the average coefficient of torque, C_T for the turbine. The tip speed ratio for a turbine is given by Eq. 3.24.

$$C_P = \frac{2P_{avg}}{\rho A u^3} = \lambda C_T \tag{3.23}$$

$$\lambda = \omega R/u \tag{3.24}$$

By substituting the expression for average power output C_P, we obtain Eq. 3.25 and then by concising it by using the expression for tip speed ration as shown in Eq. 3.24, we obtain the final expression for the coefficient of power for cyclic pitch turbine as shown in Eq. 3.26. The equation is simple and shows that the performance of the turbine is solely based on the drag coefficient of the flat plate which is a constant and the tip speed ratio λ which can be controlled by adjusting the load on the turbine.

$$C_P = \frac{1}{4\pi} C_D \left(\frac{\omega R}{4u}\pi - \frac{4\omega^2 R^2}{3u^2} + \frac{\omega^3 R^3}{4u^3}\pi \right) \tag{3.25}$$

$$C_P = \frac{1}{4\pi} C_D \left(\frac{\pi}{4}\lambda - \frac{4}{3}\lambda^2 + \frac{\pi}{4}\lambda^3 \right) \tag{3.26}$$

In addition, the expression for C_P changes if the turbine blade is not active/vertically oriented for the entire 180° (azimuth angle ranging from $-\pi/2$ to $\pi/2$) of rotation but only a part of it. For example, if the blades are active from $-\theta$ to θ, we determined the expression for C_P by integrating Eq. 3.21 from $-\theta$ to θ instead and the result is shown in Eq. 3.27

$$C_P = \frac{1}{4\pi} C_D \left(\frac{1}{2}\lambda(\theta + \frac{1}{2}\sin 2\theta) - \frac{4}{3}\lambda^2 \sin\theta + \frac{\theta}{2}\lambda^3 \right) \tag{3.27}$$

The expression for the coefficient of power developed for the CPT with 180° of drive stroke and 180° of recovery stroke is given by Eq. 3.26 and is plotted against tip speed ration λ in Fig. 3.4. It shows that the C_P for the cyclic pitch turbine increases monotonically increases and goes beyond 100% which is impossible for any real machine.

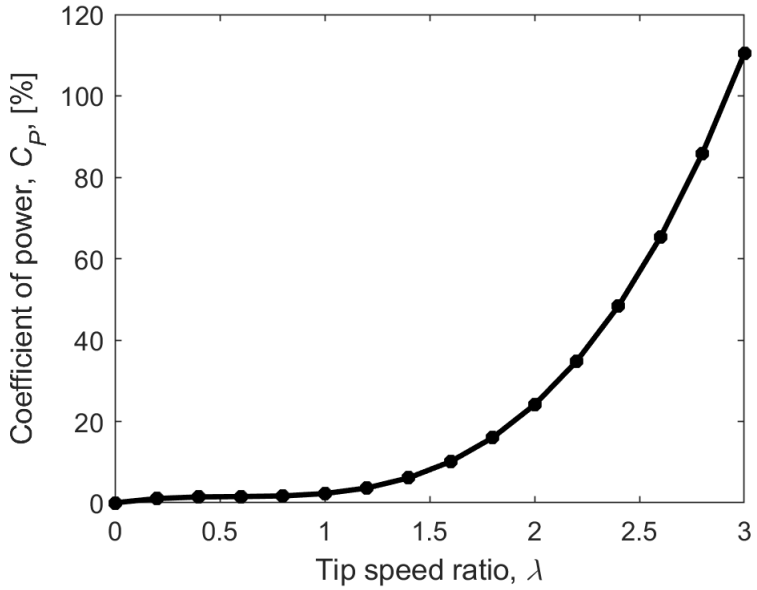

Figure 3.4: Coefficient of power plotted using the equations developed for the CPT turbine shows ever increasing C_P values.

3.3.7 Sign Term Correction

A closer look at the utilized equations for the relative normal component of velocity described by Eq. 3.7 gives a clue. The relative normal velocity, u_n changes along the length of the blade and also with azimuth angle θ. At some radial locations on the CPT blade, close to the blade's tip and for some steep azimuth angles close to $\pi/2$ and $-\pi/2$, the relative velocity is negative as shown in Fig. 3.5. The figure shows the negative relative velocity regions as a function of radial location and azimuth to be the area on the surface under the transparent red plane. It can be observed that the trend is symmetrical about the reference zero azimuth and that, at very steep angles, most of the blade length experiences negative normal component of relative velocity, u_n. Further, increasing the tip speed ratio of the blades adversely affects the blades by reducing the positive force generating locations and increasing the magnitude as well as the extent of locations where negative relative velocity is observed.

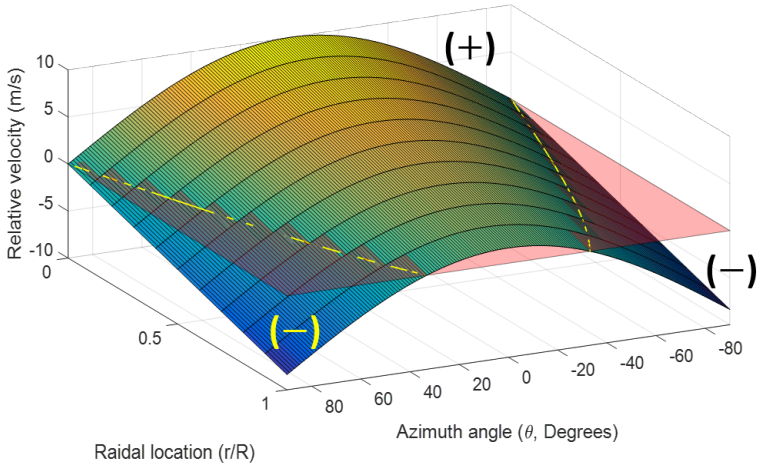

Figure 3.5: Relative velocity plot as a function of radial blade locations and azimuth angles shown as a surface indicating positive and negative values.

Consequently, the drag force at such locations on the blades, are expected to be negative and in the opposite direction to that of the regular turbine rotation. This adversely influences the total blade force, torque and consequently power generation and coefficient of power. Yet, using the equations, we obtain positive drag force values at the blade tip as shown in Fig. 3.6 which explains the continuously increasing C_P as shown in Fig. 3.4. Careful analysis of the drag force equation shows that the squared term, u_n^2 in Eq. 3.8 loses the information about the sign (+ or -) which corresponds to the direction of force when drag force is calculated. This explains the positive drag force at the blade tip if Fig. 3.6 and ever increasing C_P in Fig. 3.4. And corrective measures need to be taken.

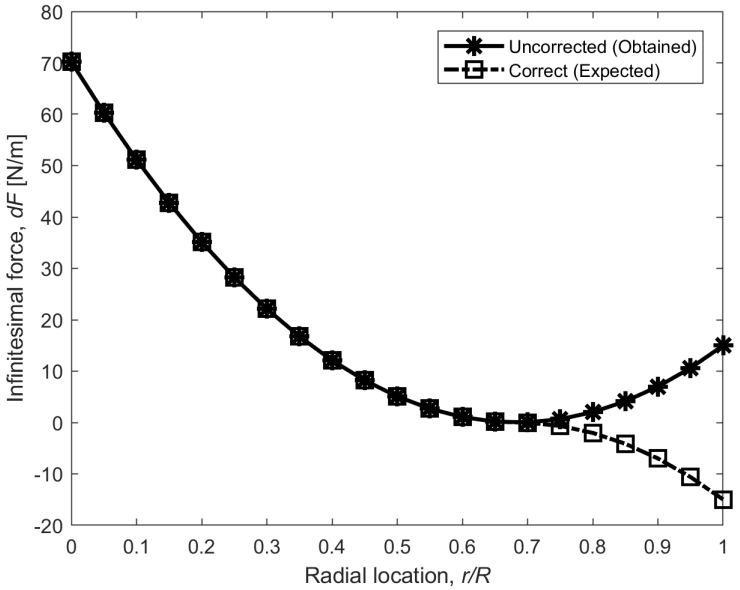

Figure 3.6: Illustrations showing a CPT blade producing strictly positive power across the blade length and both positive and negative power at different locations of the blade length.

As discussed above, a blade can experience both positive and negative drag forces at different regions of the blade. At a radial location on the blade at a distance, r_0 shown in Fig. 3.7, from the blade's root, the relative normal velocity is zero. From this radial location, r_0, the blade area closer to the root produces positive power while the rest of the blade area after this radial location generates negative power. The analysis can be split into two at this location and integrated separately to determine power output for each section. In order to separate the sections, the radial location, r_0 is determined as shown in Eq. 3.28 and it shows that r_0 depends on azimuth, θ, fluid velocity, u and the angular velocity ω of the turbine.

$$\begin{aligned} u_n &= u\cos\theta - r_0\omega = 0 \\ r_0 &= \frac{u\cos\theta}{\omega} \end{aligned} \tag{3.28}$$

At some azimuth angles, r_0 could be larger than the length of the blade R (as indicated in Eq. 3.29) and in such instances, the whole blade experiences positive relative velocity and generates positive power P_1. The location of r_0 for different azimuth angles are shown in Fig. 3.7 as a yellow line which is the intersection between the relative normal velocity plane and the zero value transparent red plane.

$$r_0 = \frac{u \cos\theta}{\omega} > R \tag{3.29}$$

This occurs up to a certain azimuth angle, θ_0 on either side of the reference zero for fixed angular velocity, ω, blade length, R and free stream velocity, u as shown in Fig. 3.7. This azimuth angle, θ_0 can be determined using Eq. 3.30.

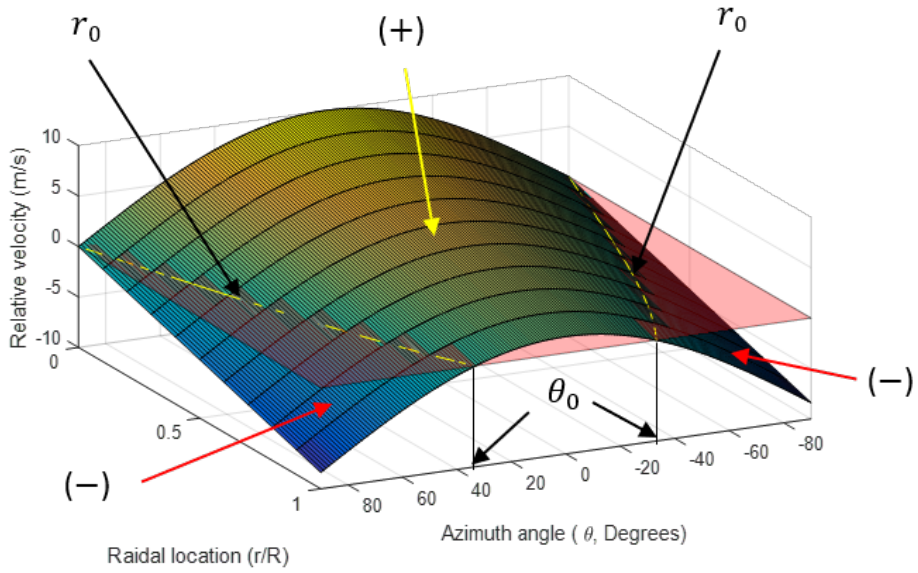

Figure 3.7: Location of r_0 and θ_0 depicted on relative velocity surface plot drawn as a function of blade's radial location and azimuth angle.

$$\theta_0 = \arccos\frac{\omega R}{u} = \arccos\lambda \tag{3.30}$$

In other cases, where $r_0 < R$, a part of the blade close to the root produces positive power P_p and the remaining part produces negative power P_n as indicated in Fig. 3.8.

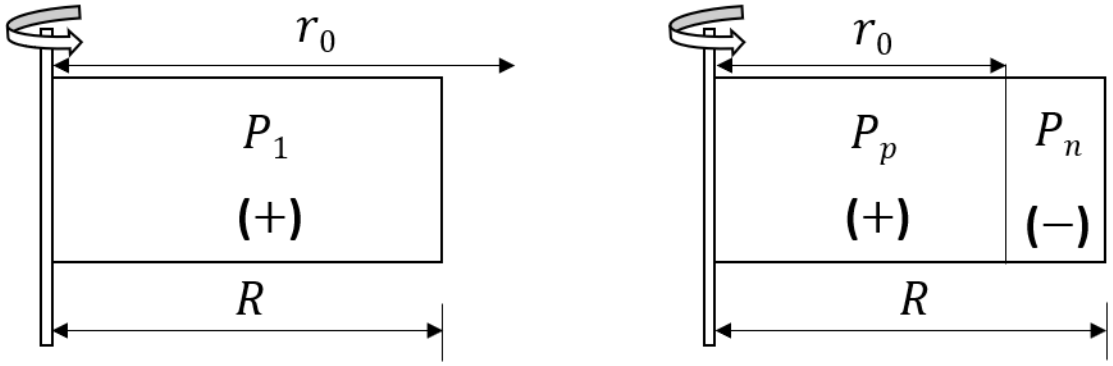

Figure 3.8: Turbine blades producing either just positive power or both positive and negative power at different locations on the blade.

The equations developed in previous sections are used again to determine the power output, P_1 from the entire blade up to azimuth angle, θ_0 as given in Eq. 3.31

$$P_1 = \frac{1}{2} C_D \rho H \left(u^2 \frac{\omega R^2}{2} \cos^2\theta - \frac{2\omega^2 R^3}{3} u \cos\theta + \frac{\omega^3 R^4}{4} \right) \tag{3.31}$$

For angles greater than θ_0, the positive power P_p generated from the root of the blade to a radial location r_0 and the negative power P_n generated by the rest of the blade up to the tip are calculated separately and are given by Eq. 3.32 and Eq. 3.33.

$$P_p = \frac{1}{2} C_D \rho H \left(u^2 \frac{\omega r_0^2}{2} \cos^2\theta - \frac{2\omega^2 r_0^3}{3} u \cos\theta + \frac{\omega^3 r_0^4}{4} \right) \tag{3.32}$$

$$P_n = \frac{1}{2} C_D \rho H \Big(u^2 \frac{\omega (R^2 - r_0^2)}{2} \cos^2\theta - \frac{2\omega^2 (R^3 - r_0^3)}{3} u \cos\theta + \frac{\omega^3 (R^4 - r_0^4)}{4} \Big) \quad (3.33)$$

It can be observed that, at any given azimuth angle, if we subtract the positive power P_p (Eq. 3.32) from total uncorrected power P (Eq. 3.17), we obtain the equation for the negative power P_n (Eq. 3.33).

Substituting the value of r_0 in the above equation for P_p, we get Eq. 3.34.

$$\begin{aligned} P_p &= \frac{1}{2} C_D \rho H \Big(\frac{u^4}{2\omega} \cos^4\theta - \frac{2u^4}{3\omega} \cos^4\theta + \frac{u^4}{4\omega} \cos^4\theta \Big) \\ P_p &= \frac{1}{2} C_D \rho H \Big(\frac{u^4}{12\omega} \cos^4\theta \Big) \end{aligned} \quad (3.34)$$

And similarly substituting r_0 for the negative power P_n, we obtain Eq. 3.35.

$$P_n = \frac{1}{2} C_D \rho H \left(\frac{1}{2} u^2 \omega R^2 \cos^2\theta - \frac{2}{3} u \omega^2 R^3 \cos\theta + \frac{1}{4} \omega^3 R^4 - \frac{1}{12} u^4 \frac{\cos^4\theta}{\omega} \right) \quad (3.35)$$

Now, the average power generated by one blade for one complete rotation about the turbine axis is obtained by integrating the corrected instantaneous power output as shown in Eq. 3.36.

$$P_{avg} = \frac{1}{2\pi} \Big(\int_{\frac{-\pi}{2}}^{\frac{\pi}{2}} P d\theta \Big) \quad (3.36)$$

The corrected instantaneous power output consists of three equations obtained in Eq. 3.31, Eq. 3.34 and Eq. 3.35 for their respective azimuth angles as shown in Eq. 3.37

$$
\begin{aligned}
P_{avg} &= \frac{1}{2\pi}\Bigg[\int_{-\theta_0}^{\theta_0} P_1 + \int_{\theta_0}^{\frac{\pi}{2}} (P_p - P_n) + \int_{\frac{-\pi}{2}}^{-\theta_0} (P_p - P_n)\Bigg] d\theta \\
P_{avg} &= \frac{1}{2\pi}\Bigg[\int_{0}^{\theta_0} 2P_1 + \int_{\theta_0}^{\frac{\pi}{2}} 2(P_p - P_n)\Bigg] d\theta
\end{aligned}
\tag{3.37}
$$

Substituting the equations for power and integrating with respect to azimuth angle θ, we get the average power output from a cyclic pitch turbine blade as given in Eq. 3.38.

$$
\begin{aligned}
P_{avg} = \frac{1}{2\pi} C_D \rho H \Bigg\{ & \frac{1}{2} u^2 \omega R^2 (\theta_0 - \frac{\pi}{2} + \frac{1}{2}\sin 2\theta_0) - \frac{2}{3}\omega^2 R^3 u (2\sin\theta_0 - 1) ... \\
... + \ & \frac{1}{4}\omega^3 R^4 (2\theta_0 - \frac{\pi}{2}) + \frac{1}{384\omega} u^4 \Big[12(\frac{\pi}{2} - \theta_0) - 8\sin 2\theta_0 - \sin 4\theta_0 \Bigg\}
\end{aligned}
\tag{3.38}
$$

We can use this equation to determine the coefficient of power, C_P as shown in Eq. 3.39

$$
\begin{aligned}
C_P &= \frac{2P_{avg}}{\rho H R u^3} \\
C_P &= \frac{1}{2\pi} C_D \Bigg\{ \frac{R\omega}{u} (\theta_0 - \frac{\pi}{2} + \frac{1}{2}\sin 2\theta) - \frac{2}{3}\frac{\omega^2 R^2}{u^2} (2\sin\theta_0 - 1) ... \\
&... + \ \frac{1}{4}\frac{\omega^2 R^3}{u^3} (2\theta_0 - \frac{\pi}{2}) + \frac{1}{384}\frac{u}{\omega R} \Big[12(\frac{\pi}{2} - \theta_0) - 8\sin 2\theta_0 - \sin 4\theta_0 \Bigg\}
\end{aligned}
\tag{3.39}
$$

The non-dimensional term tip speed ration, λ is used to simplify the above equation. Also considering the whole turbine instead of just one blade, the coefficient of power for a 3 bladed cyclic pitch turbine is determined by using Eq. 3.40. For a 3 bladed turbine, the blades are separated by 120° and when one of the three blades is close

to the middle of drive stroke (on either side of zero degrees azimuth angle) where most of the power is generated, the other two blades are passive and do not affect the flow onto the first blade undergoing the drive stroke. Hence, it is assumed for the CPT turbine having three or fewer blades, the shadowing effects between the blades are not considered. The equation is a function of just the tip speed ratio since C_D is a constant and θ_0 is also solely dependent on the tip speed ratio of the turbine. The theoretical model of the turbine follows the empirical wind turbine trend that its performance does not vary based on wind speed as long as the speed of rotation of the turbine is appropriately changed as well to maintain the same tip speed ratio. Hence the cyclic pitch turbine can be optimized to be operated at the best λ to achieve the highest possible coefficient of power.

$$C_P = \frac{3 \times 100}{2\pi} C_D \Bigg\{ \lambda(\theta_0 - \frac{\pi}{2} + \frac{1}{2}\sin 2\theta) - \frac{2}{3}\lambda^2(2\sin\theta_0 - 1)... \\ ... + \frac{1}{4}\lambda^3(2\theta_0 - \frac{\pi}{2}) + \frac{1}{384\lambda}\Big[12(\frac{\pi}{2} - \theta_0) - 8\sin 2\theta_0 - \sin 4\theta_0 \Bigg\} \tag{3.40}$$

3.3.8 Shorter Drive Strokes

The equations developed above consider that the turbine blades orient vertically and engage in drive stroke for 180° of rotation and rest of the rotation for the recovery stroke. It is observed in later chapters that, having a shorter drive stroke is beneficial than having it for the whole 180°. As a result, the 90° pitching of the blades initiates and finishes to become parallel to the flow before the blade moves into the upstream flow. Considering that the blades pitch and become passive at θ azimuth, then the average power output from a blade is determined by limiting the integration to the active azimuth angles as shown in Eq. 3.41. The equation holds when θ is greater than θ_0 which is the azimuth angle where the blade experiences both positive and

negative drag forces.

$$P_{avg} = \frac{1}{2\pi}\left[\int_0^{\theta_0} 2P_1 + \int_{\theta_0}^{\theta} 2(P_p - P_n)\right]d\theta \tag{3.41}$$

And if θ is less than θ_0, then, the second term in the above equation is zero and hence the equation reduces to Eq. 3.42. But doing so would be to not take advantage of the positive energy available and is not recommended.

$$P_{avg} = \frac{1}{\pi}\int_0^{\theta} P_1 d\theta \tag{3.42}$$

The solutions to the coefficient of power in such cases can also be determined numerically using the above two equations and integrating them over their appropriate azimuth angles.

The contributions from these three terms P_1, P_p and P_n can be individually plotted to observe the contribution from each of them at different azimuth angles.

Integration of the formulae indicated above is performed for a three bladed turbine and the parameters used are $H = 0.3$ m, $R = 1$ m, $\rho = 1000$ kg/m^3 (water), $u = 1$ m/s, $C_D = 1.2$, $\lambda = 0.45$. One aspect that needs to be considered when integrating dF and dT is whether the contribution from each of the infinitesimal blade elements is positive or negative. The information regarding the sign of the drag force on each blade element is lost when the relative velocity term in Eqs. 3.8 and 3.11 is squared. For a given azimuth angle location of the blade, based on the angular velocity and the free stream velocity, the relative velocity indicated by Eq. 3.1 becomes zero at a particular radius and is negative for the rest of the blade length. This is clearly apparent from Eq. 3.1 and also can be observed in the load distribution diagram along

the length of the blade as shown in Fig. 3.6. The figure is at an azimuth of $\theta = 70^{\circ}$ and it shows a positive force on the blade changing into a negative force towards the farther part of the blade from the turbine axis. This negative load distribution indicates that for the particular example analyzed, the tangential velocity for blade elements for r/R close to unity is higher than the normal component of the fluid velocity (*i.e.* $u\cos\theta - r\omega < 0$).

Chapter 4

Theoretical Results

The equations developed in the previous chapter are used to determine some of the static as well as dynamic characteristics of the cyclic pitch turbine. The static characteristics are also compared to a simple theoretical model of Savonius whose properties are described in section 3.2.2.

4.1 Static Characteristics

The static analysis of a turbine corresponds to the forces on stationary blades either voluntarily or not. It is used to predict a turbine's starting torque as a positive value indicates the ability to self-start from rest. The static torque coefficient, C_{TS}, is a good measure of the static characteristics of a turbine and is calculated using Eq. 3.6.

4.1.1 Comparision with Savonius

The static torque coefficient is calculated for both CPT and Savonius for one, two and three bladed turbine designs and compared with each other. The results are plotted as shown in Fig. 4.1. For the one bladed turbine comparison,a similar trend for both turbines is observed for the whole rotation (from 0° to 360°). The cyclic pitch turbine has an average C_{TS} that is 7% higher than that of the Savonius turbine. For the one bladed turbine configuration, as shown in Fig. 4.1 (a), the CPT has a zero C_{TS} during the recovery stroke while the Savonius turbines experience negative

torque values during the same period (azimuth angles $90^\circ \ll 270^\circ$). For the two blade configuration shown in Fig. 4.1 (b), the CPT follows closely with that of Savonius and shows a slightly higher C_{TS}. And for the three blade configuration in Fig. 4.1 (c), both turbines show an oscillating C_{TS}, with the CPT turbine having a lower amplitude fluctuation which is desirable for a more consistent and uniform power output. The Savonius turbine, in one rotation, has three instances of slightly negative torque values around $\theta = 60^\circ$, 180° and 300° where the turbine would not be self-starting. It can be observed from the above three plots that the average starting torque for this CPT turbine is always non-negative and is slightly higher and more consistent than that of Savonius turbine (Rao *et al.*, 2016).

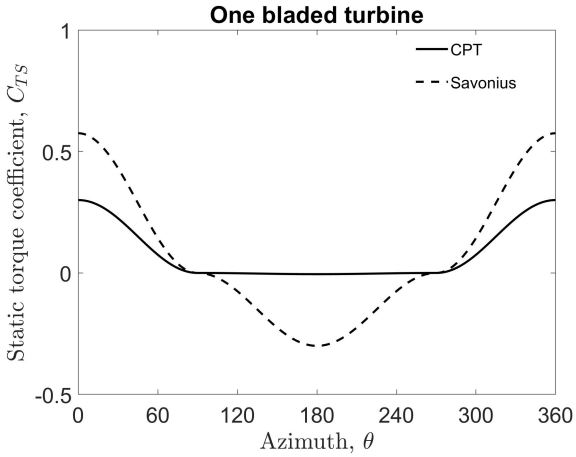

(a)

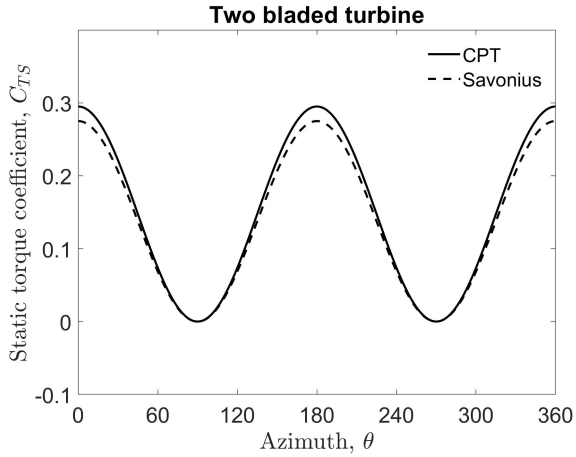

(b)

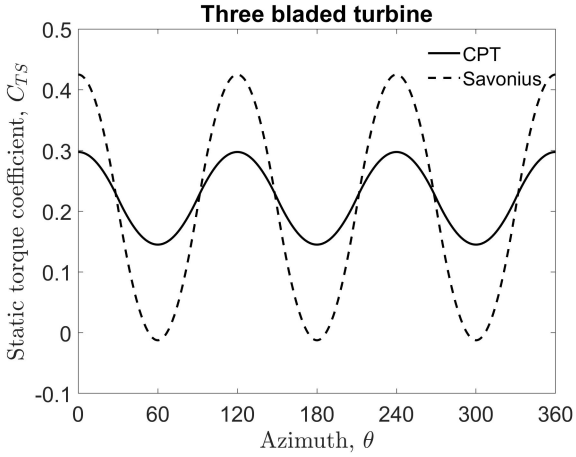

(c)

Figure 4.1: Coefficient of static torque, C_{TS} comparison between CPT and Savonius for 1, 2 and 3 bladed turbine configurations.

4.2 Dynamic Characteristics

The dynamic characteristics of the Cyclic pitch turbine for a fixed angular velocity are analyzed in this section to evaluate blade forces, torque, power output, torque and power coefficients. The turbine and flow parameters selected for the force, torque and power calculation representations are number of blades $n = 3$, blade width, $H = 0.3$ m, blade length, $R = 1$ m, density of fluid, $\rho = 1000$ kg/m^3 (water), flow velocity, $u = 1$ m/s (Reynolds number = 60,000), coefficient of drag, $C_D = 1.2$ and tip speed ratio $\lambda = 0.45$.

4.2.1 Comparison with Savonius

The blades of a turbine experience a change in relative velocities along the blade length when they abruptly start to rotate from a standstill. This also results in different magnitudes of force and the torque generated as well at different blade locations. The radial flow velocity component u_r has a negligible contribution to the aiding drag force or torque generated since it acts through the axis of rotation of the turbine. On the other hand, the relative normal flow velocity component u_n given by Eq. 3.7 interacts with the blade and is the main source of torque. Furthermore, the effect of the relative normal flow velocity on the drag force and torque can be evaluated from Eq. 3.8 and Eq. 3.11. The equations show that, in a dynamic setting, the magnitude of both force and torque decrease for both the CPT and Savonius turbines for the drive stroke. As the blades travel downstream in the flow direction, the relative normal flow velocity decreases. Meanwhile, the relative normal flow velocity increases for the recovery stroke since the blades are traveling upstream and opposite to the flow direction. The effect of an increase in relative normal flow velocity for the recovery stroke on the Savonius turbines is an increase in the adverse drag and negative torque values. On the other hand, the effect of a change in relative velocity during recovery stroke

on the cyclic pitch turbine is negligible. This is a result of negligible drag coefficient in the recovery stroke for CPT. This is the problem that is being solved and the advantage of a CPT turbine over a Savonius turbine.

In a simple and crude comparison between the CPT and Savonius, their coefficient of torques, for a two-bladed configuration, in a dynamic condition are tested and compared. The comparison is done when one blade is at an azimuth angle of zero degrees while the other is in the recovery stroke and at an azimuth angle of 180°. The analysis is conducted only on an infinitesimal blade element midway through the radius of a blade. The torque contribution by such a blade element and consequently its coefficient of torque is determined when the turbines start to abruptly rotate at different tip speed ratios λ varying from 0 to 1. The comparison is shown in Fig. 4.2. The equations and the figure predict a faster reduction in net positive drag and torque coefficient for the Savonius turbine. Although this is only a crude approximation, it gives an idea of how the two turbines might operate under dynamic conditions.

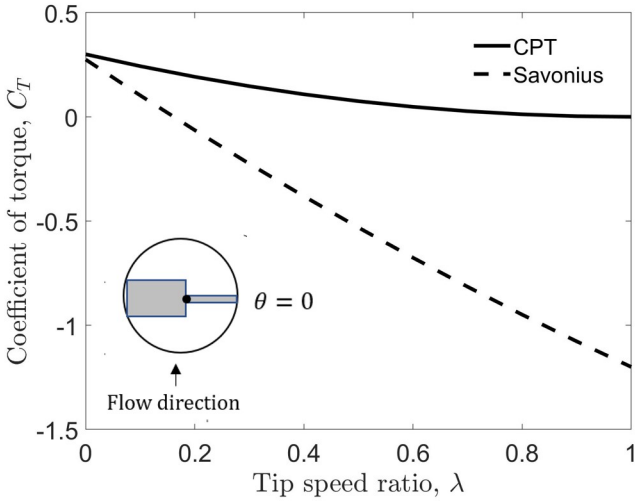

Figure 4.2: Plot showing the drop in coefficient of torque for CPT and Savonius with tip speed ratio for a two-bladed configuration with the two blades at azimuth angles 0° and 90°, as shown in the circle, considering only the midsection of the blades.

4.2.2 Azimuth and Spanwise Variations

Force, torque, and power generated by CPT blade elements at different spanwise locations and for different azimuth angles are calculated and shown as a surface grid in Fig. 4.3. This provides the blade span locations and the azimuth angles where maximum energy is being harnessed by the turbine. The figure shows the magnitudes for the three parameters for azimuth angles from 0° to 90° which is the second half of the drive stroke. The plot is symmetric and is the same for the first half of the drive stroke which is from −90° to 0°. Figure 4.3 (a) shows that the force on the blade is largest closest to the root of the blade and at zero azimuth where the blade experiences the maximum normal relative velocity. The force decreases as we move towards the blade tip and also as the azimuth angle increases. The force is zero where the relative normal velocity between the blade and fluid is zero and is negative where the blade travels faster than the fluid as observed at very high angles and near the blade tip. Similarly, Fig. 4.3 (b) shows the calculated torque values, with the maximum magnitude occurring at zero azimuth and at a radial location where the product of force and the radius is maximum which is at about a distance of 70% of radius R from blade's root. Its magnitude is lower everywhere else and is negative for negative relative velocities. And Fig. 4.3 (c) shows the instantaneous power output for the different elements of a blade for the second half of the drive stroke. It follows the same trend as torque since the power output, P is the product of torque, T and angular velocity, ω which is considered to be constant.

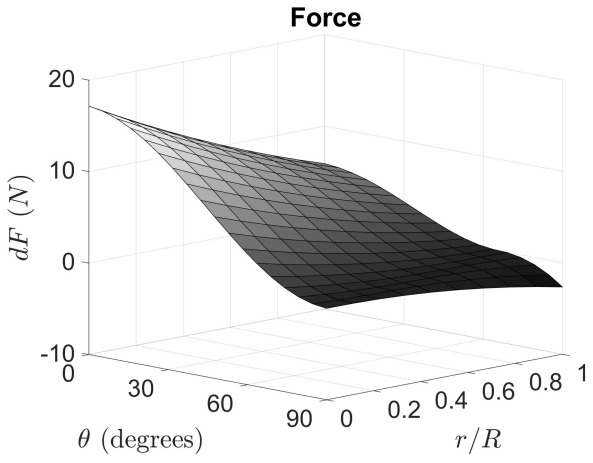

(a)

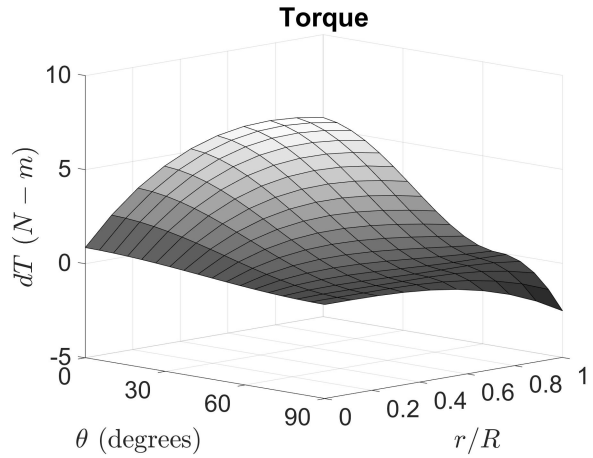

(b)

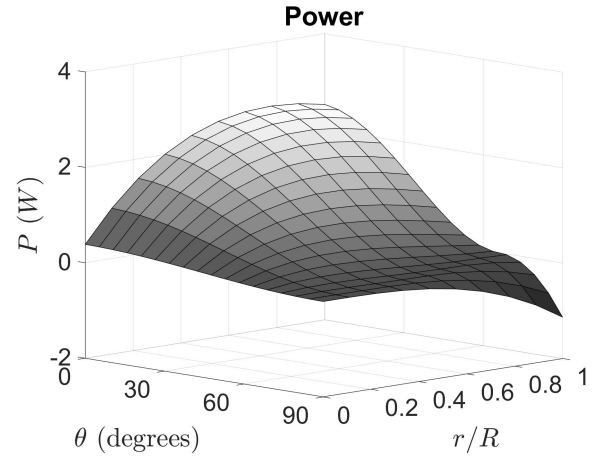

(c)

Figure 4.3: Surface grid plots showing the variation of force torque and power on a CPT blade at all radial locations and for the second half of the drive stroke.

4.2.3 Coefficient of Torque and Power

The coefficient of torque, C_T and power, C_P of the cyclic pitch turbine is calculated using the equations developed in the mathematical model of the CPT turbine and plotted as a function of tip speed ratio, λ and the active drive stroke angle β which are looked into in more detail in the following chapter.

Tip speed ratio

Tip speed ratio λ is the ratio of the tangential velocity ωr of the blade tip to the free stream velocity u. It is a non-dimensional independent parameter of the turbine which can be controlled by changing the load on a turbine. Figure 4.4 shows the variation of coefficient of torque, C_T as a function of tip speed ratio. The plot shows that the coefficient of torque decreases continuously from a value of about 0.35 at a tip speed ratio value of 0.1 to a value of 0.05 C_T for $\lambda = 01$. This gradual drop in torque coefficient is expected and typical of wind turbine especially Savonius (Akwa *et al.*, 2012). The plot indicates that, for a given free stream velocity, as the turbine rotates faster, its torque coefficient continuously reduces as a result. Figure 4.5 shows the variation of C_P as a function of λ. It can be seen that the coefficient of power reaches a maximum value of close to 9% at an intermediate tip speed ratio close to 0.5. Both these plots are given for an active drive stroke angles of 120° which is discussed in the next section.

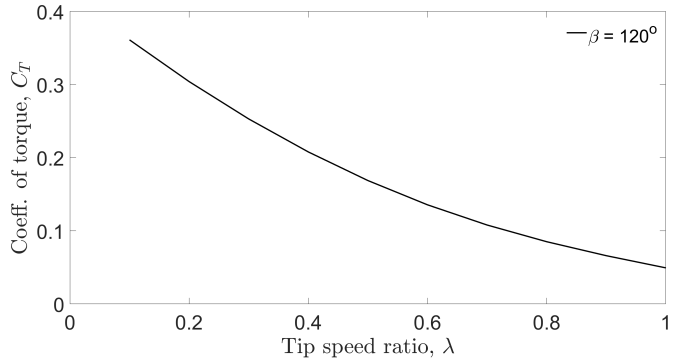

Figure 4.4: Variation of coefficient of power, C_P of a cyclic pitch turbine with tip speed ratio, λ.

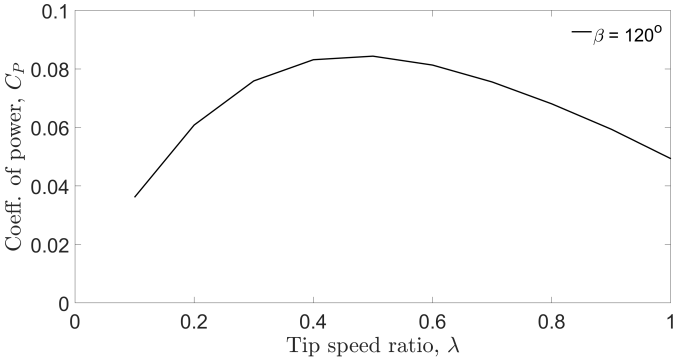

Figure 4.5: Variation of coefficient of power, C_P of a cyclic pitch turbine with tip speed ratio, λ.

Active drive stroke angle

The coefficient of torque and power are determined here as a function of active drive stroke angle β which is a measure of the duration of drive stroke of the cyclic pitch turbine in degrees. Its limits are 0° and 180° and a value of 0 for β means the blades are never active (no energy harnessed) and a value of 180° means that the blades are active for half of the entire rotation of a turbine blade. Figure 4.6 shows the variation of coefficient of torque, C_T of the CPT turbine for a fixed tip speed ratio of 0.55 while active drive stroke angle, β is changed from 0° all the way to 180°. It shows that optimal value of β for a given λ of 0.55, to achieve maximum possible C_T (0.15 in

this case) is around 140°. Figure 4.7 shows that, for a tip speed ratio of $\lambda = 0.55$, a maximum value of around 9% C_P is achieved while β is changed from 0° to 180°. Optimization of the coefficient of power and more details of the active drive stroke angle are given in the chapter 5.

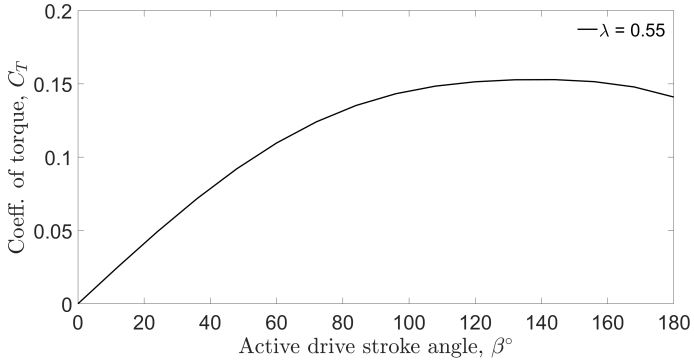

Figure 4.6: Variation of coefficient of power, C_P of a cyclic pitch turbine with active drive stroke angle, β.

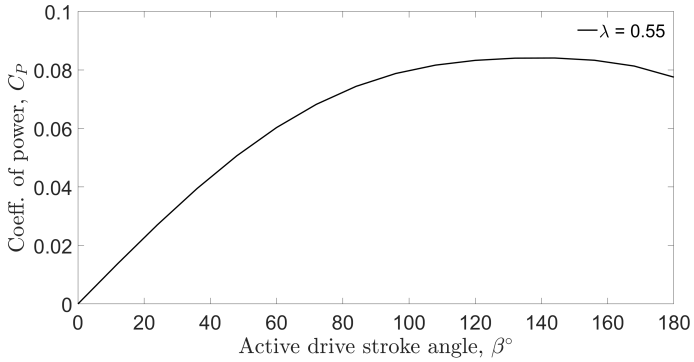

Figure 4.7: Variation of coefficient of power, C_P of a cyclic pitch turbine with active drive stroke angle, β.

Chapter 5

Optimal CPT Configuration

The performance of the developed Cyclic pitch turbine is optimized in this chapter using parameters like tip speed ratio λ and active drive stroke angle β. Different values for the two parameters are tested to determine their combinations where the coefficient of power is the highest for the turbine. Analysis of the variation in power output from a CPT blade for one rotation clearly shows the reasons for selecting these two parameters for optimizing turbine performance.

The power output from one blade of a CPT turbine varies with the azimuth angle for different tip speed ratios as shown in Fig. 5.1. The plot shows the power output during the drive and the recovery strokes. During the recovery stroke ($90° < \theta < 270°$), the blade is passive and uses minimum energy to power output is zero as expected. The maximum power output during the drive stroke is lowest for very low tip speed ratio like 0.1. As the tip speed ratio increases to 0.4 or 0.7, the power output increases and then it drops down as the tip speed ratio is further increased to a value of 1. Also, during the drive stroke, the power output which is expected to be mostly positive shows steeply increasing negative values at the beginning and right before the end of the drive stroke. These locations corresponds to azimuth angles approximately $270° < \theta < 285°$ (or $-90° < \theta < -75°$) and $75° < \theta < 90°$ respectively. For these ranges of azimuth angles, the relative normal velocity component of the flow is negative (i.e. $u\cos\theta - r\omega < 0$) for a large part of the blade length. This means that a large part of the blade is moving faster than the local flow and as a result,

energy is being spent to move the blade against the flow, instead of harnessing energy from the flow. Also, it is clear from the figure that, as the tip speed ratio increases, the blade is pushing against the fluid with a higher force and hence more power is consumed by the blade. Since the theoretical model assumes that the 90° blade pitching happens instantaneously, the power output changes from a negative value to zero instantaneously as well. The two parameters, β and λ and their effect of C_P is analyzed below.

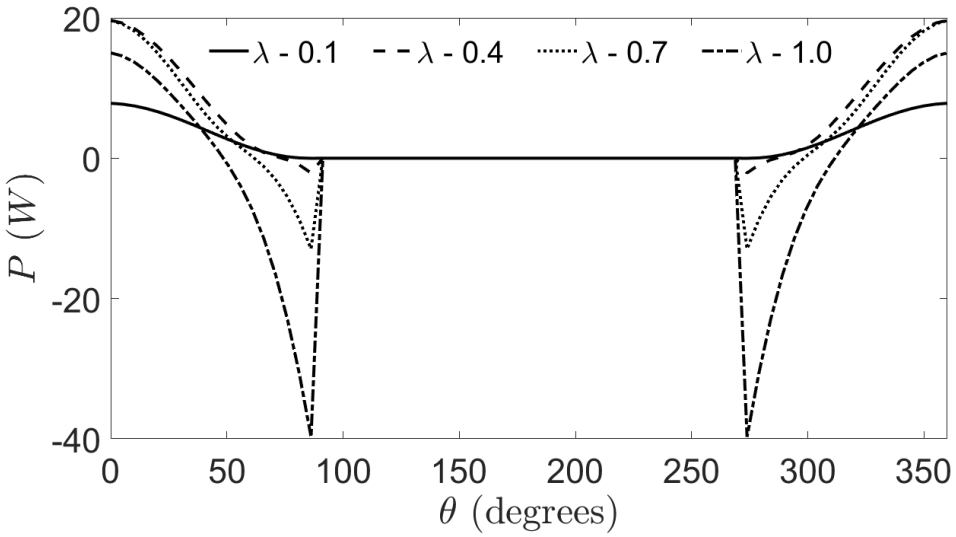

Figure 5.1: Power output variation from a CPT blade in one complete cycle showing power loss at certain azimuth angles.

5.1 Active Drive Stroke Angle

The active drive stroke angle, β is the measure of the size of the angle during which a turbine blade stays vertical (angle of attack of 90°) and actively harnesses energy from fluid flow. Or simply, it is the as the range of angle between the beginning and the end of the drive stroke. As described in previous chapters, the value of β can be smaller than 180°, as indicated in Fig. 5.2 which can be achieved by changing the location where the turbine blades pitch by the 90°. This is practically achieved by designing the cam surface so that the cam ridges match the required pitching

locations as described in section 6.1. To achieve a positive outcome, the pitching of the turbine blades from passive to being active is done well after they pass the $-90°$ azimuth angle and then the pitching back to passive is to be done well ahead of the $+90°$ azimuth mark.

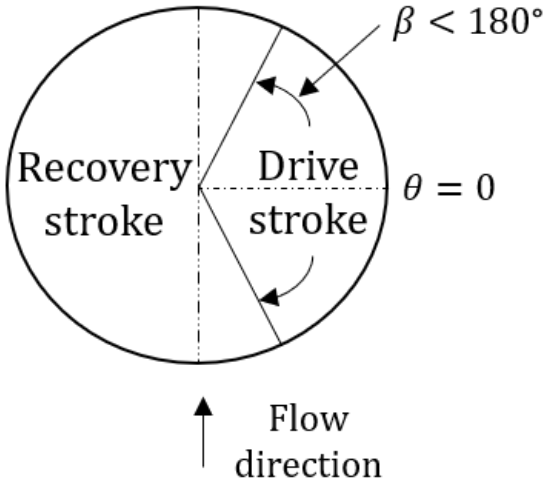

Figure 5.2: Illustration of an active drive stroke angle of less than 180°. Consequently, recovery stroke angle is increased to greater than 180°

The effect of reducing the active drive stroke angle is apparent by observing the power output from the CPT for one whole rotation of the turbine. The CPT cycle can be optimized to avoid the two regions of negative power apparent in Fig. 5.1 by following two design changes. The first change is to start orienting the blades horizontally a few degrees before the end of the drive stroke (for eg. at 75° instead of 90°) to avoid the first negative power region. The second step is to delay the blades rotating back to their vertical orientation right after the recovery stroke (for eg. at $-75°$ instead of $-90°$) to avoid the second negative power zone shown in Fig. 5.1. The result would be having an active drive stroke angle of less than 180°. The effect of having smaller than 180° active drive strokes on the coefficient of power, C_P is depicted in Fig. 5.3 for several tip speed ratio values. The plot is generated using the mathematical model developed and the different lines in the plot indicate different tip speed ratios ranging from 0.1 to 0.9. The figure shows that the CPT turbine performs very poorly for very

small values of β. For very small tip speed ratios like 0.1 and 0.3, the plot shows that the coefficient of power, C_P increases to about its peak value at about $\beta = 140°$ and does not change for any increase in β up to 180°. For higher tip speed ratios like 0.5, 0.7 and 0.9 calculated, when the active drive stroke angle increases, the coefficient of power increases to its maximum possible value depending on its tip speed ratio and drops for further increase in β. Overall an active drive stroke angle of about $\beta = 130°$ seems to be the most optimal for the highest C_P.

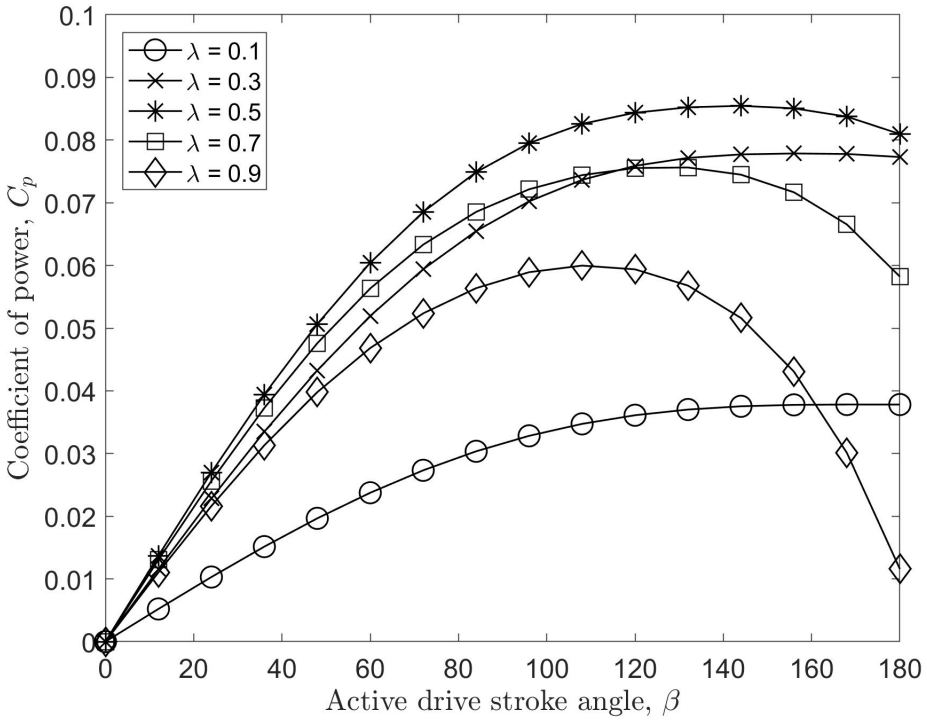

Figure 5.3: Optimization of C_P with active drive stroke angle, β at several tip speed ratios.

5.2 Tip Speed Ratio

The dynamic analysis on CPT is conducted to determine the most optimal tip speed ratio, λ for the maximum turbine performance. The coefficient of power, C_P, is calculated using the mathematical model developed and plotted in Fig. 5.4 as tip

speed ratio changes from 0.1 to a value of 0.9 for several values of β ranging from 60° all the way to 180° indicated using different lines and associated markers. The figure shows that for all active drive stroke angles, the coefficient of power is very low for very small (0.1 to 0.3) as well as very large ($\lambda > 0.7$) tip speed ratios. Coeff of power, C_P is maximum for all values of β at values of λ ranging between 0.4 and 0.6 depending on β. The most optimal λ value of around 0.5 which is less than a value of 1 is typical of drag based turbine including Savonius where maximum power generation/performance is observed (Zhao *et al.*, 2009), (Kang *et al.*, 2014).

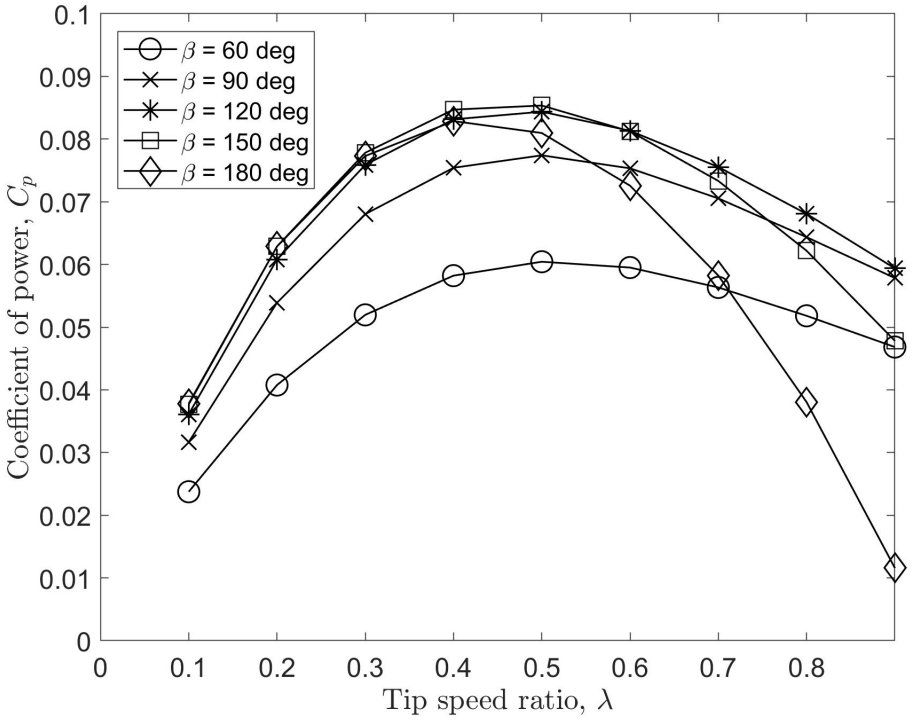

Figure 5.4: Optimization of C_P with tip speed ratios λ at several active drive stroke angles.

5.3 Optimal CPT Configuration

The coefficient of power, C_P is optimized as a combined function of the two parameters λ and β simultaneously and the resulting surface plot is shown in Fig. 5.5. The figure

shows that the turbine performs its worst and consumes power for an active drive stroke angle of 180° and a tip speed ratio of 1 which are the maximum values tested. The cyclic pitch turbine performs badly at very low tip speed ratios or very low active drive stroke angles. The best CPT performance is observed for a configuration with $\lambda \sim 0.5$ and $\beta \sim 130°$. Despite the clear indication from the analytical results, of positive turbine performance and minimal recovery stroke losses, experiments are necessary to validate the claims and are performed in the following chapters.

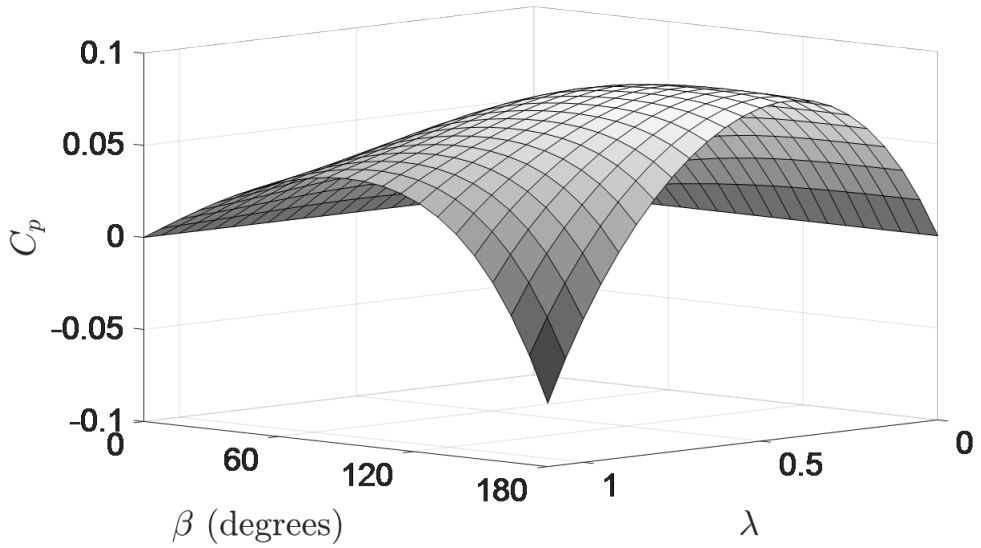

Figure 5.5: Optimization of C_P as a simultaneous function of λ and β.

Chapter 6

Prototype Fabrication

The cyclic pitch turbine concept described and modeled in chapter 2 is designed and fabricated for experimental testing in wind tunnel and water channel. Rapid prototyping methods and some conventional machines are used to fabricate the different parts that go into the turbine assembly. A brief explanation of the design parameters chosen for the different parts is given below.

6.1 Cams

Cam surface design governs the motion of the followers which slide and pitch across their surface. The 360° circumference of the inner cam is divided into 4 sections which are the elevated, lowered surfaces and the raising and lowering ridges corresponding to the drive stroke, recovery stroke, and the two pitching motions. The cam circumference is depicted on a linear cam as shown in Fig. 6.1 for simplicity. For the first prototype, the 90° blade pitching motion is mechanized to start 10° before the end of each stroke and end 10° after the beginning of the next stroke as shown in the figure. As a result, the 90° blade pitching motion is smoother and occurs over a 20° rotation of the turbine. This allows the blades to tilt gradually and avoid sudden vibrations. These parameters can be adjusted by changing the length of the elevated and lowered surfaces on the cams and the location and length of the ridge between the two surfaces of the dual cams. After the cam angles are chosen, the circular cam, which is more complex than the linear cam is designed on CAD software and fabricated using

a precision 3D printer. Since the cam surfaces are not part of the control surfaces, their surface roughness caused by the 3-D printers are not a cause for concern.

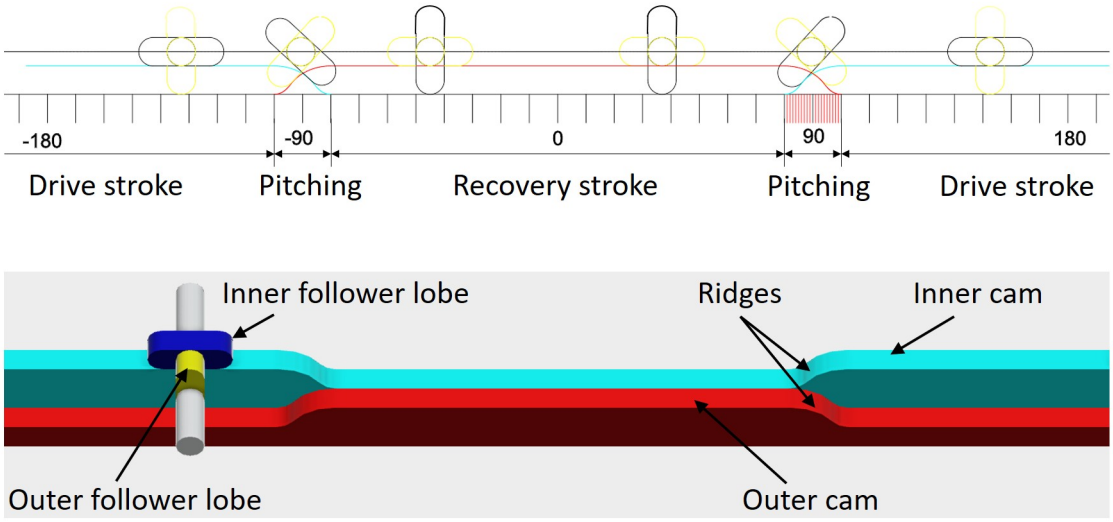

Figure 6.1: Cam surface design depicted as a linear cam to show the blade pitching locations the pitching rate with respect to the cam.

The early initiation and the delayed completion of the drive stroke are, in later chapters, discovered to incur losses to energy generation. It is also found that most of the energy is harvested in the middle of drive stroke and having a drive stroke to be longer than about 140° (exact angle depends on tip speed ratio) leads to a loss of power. For these reasons, in the second prototype, the location of pitching is changed to start 20° before the 90° mark on the linear cam as shown in Fig. 6.1. The initiation of the drive stroke is also designed to start after reaching an azimuth angle of $-90°$. In addition, the second prototype also uses ball bearings to reduce mechanism friction as described in the next section.

6.2 Followers

The follower lobes slide over the cam surfaces in order to hold the vertical or horizontal orientation of a blade. In order to eliminate the sliding friction between the lobes and

the cam surface, bearings are incorporated in the followers of the second prototype. Bearings are located at the followers' contact surfaces instead of the lobes to convert sliding friction into low resistance rolling friction. Figure 6.2 shows the different parts of the follower assembly to allow for roller ball bearings at the sliding surfaces. It can be observed that one end is to be connected to the central hub and the other end of the follower is designed to hold the turbine blade.

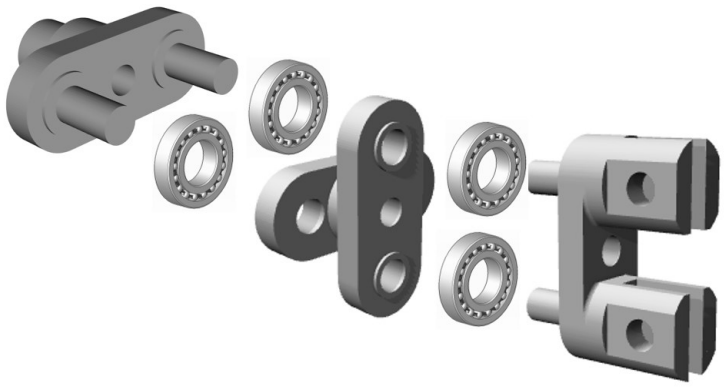

Figure 6.2: Exploded view of the follower arm assembly showing the implementation of bearings at the follower contact surfaces.

6.3 Blades

A three-bladed prototype is selected for testing in order to have at least one blade in the drive stroke at all times while keeping the design simple. Also, a three-bladed design is predicted to have a more uniform power output than a two-bladed turbine as shown by the theoretical results indicated in Fig. 4.1. Additional blades could be added but shadowing effects could become prominent, where one blade is in the wake of another reducing its effectiveness and also complicating the design. The turbine blades which are flat plates are attached to the end of the follower arm and follow the movements and orientations of the followers. For the initial design, thin rectangular blades, 160 mm long and 60 mm wide, are used for simplicity, ease of analysis and comparison with other drag based VAWTs. Different blades shapes are tested and

compared as well. The drag forces on the blades are transmitted to a central hub located at the center of the cams through the follower arms in the assembly.

6.4 Fabrication

Central hub and the cap in the turbine assembly as shown in section 2.4 are also 3D printed. All the parts are fabricated to a scale that fits inside an available water channel and wind tunnel testing facilities and to have enough clearance from the side walls to minimize boundary layer effects. The parts of the dual cam and follower mechanism are 3D printed using detail plastic and the blades are machined out of smooth PVC sheets of thickness 3 mm. Off the shelf plastic bearings with glass balls are chosen and used to avoid corrosion during water channel testing. The fabricated and assembled prototypes 1 and 2 are shown in Fig. 6.3. The difference between the first and the second prototypes is the addition of bearings on the followers for lower friction in the mechanism and also the reduced duration of the drive stroke for the second prototype. Operation of the two prototypes indicated smoother operation of prototype 2 as expected.

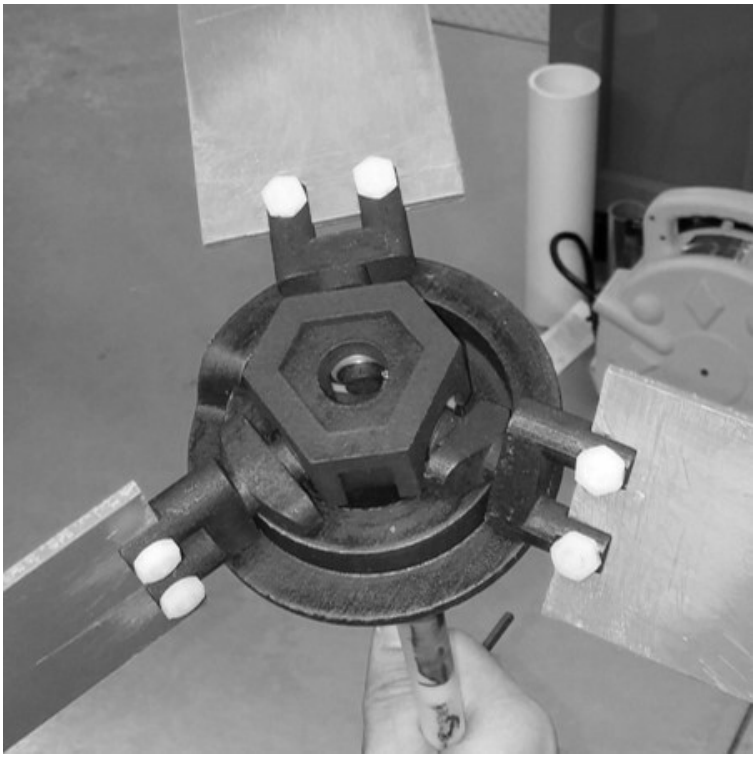

(a)

(b)

Figure 6.3: Photographs showing the fabricated and assembled CPT prototypes 1 and 2.

Chapter 7

Experiments

Experiments on the fabricated cyclic pitch turbines are conducted to prove the concept and to validate the theoretical model and its results as seen in chapters 3-5. The different experimental methods used and the observed results are discussed in this chapter.

7.1 Methods

Experiments are conducted in a wind tunnel as well as a water channel to measure various turbine parameters like rotation speed, torque, and power coefficients under different conditions of free stream velocity. The different experimental setups built, instrumentation used, procedures followed and the test conducted are described in this section.

7.1.1 Prototypes

The two prototypes built are tested to prove the concept and also to experimentally determine the performance of the cyclic pitch turbine. The first prototype is tested in air flow using a blower and in a water tunnel for proof of concept experiments and also to determine torque and power output trends. The second turbine which uses the bearings and also has a shorter drive stroke angle of $\beta \sim 150$ is used for extensive testing in all the remaining experiments indicated in this chapter.

The prototypes of the cyclic pitch turbine, both included 3 blades equally spaced as shown in prototype pictures indicated in Fig. 6.3. The blade shape selected for most experiments is rectangular with zero camber. The blades are 160 mm long and their width is 60 mm. The maximum projected blade area is 9600 sq. mm.

7.1.2 Tested Blade Shapes

Blades of different shapes and sizes are tested to determine the most optimal design for maximum power generation for the cyclic pitch turbine. In order to maintain the same flow and blockage (Ross & Altman, 2011) conditions, the blade area is maintained constant at 9600 sq. mm, where ever possible. Due to limitations on the wind tunnel testing section cross-section, while testing different aspect ratios, the area was reduced to 4800 sq. mm, which is half of the original value. The different blade shapes tested are shown in Fig. 7.1 and listed in table 7.1 where all the dimensions are indicated in millimeters. The blade shapes include rectangular blades of different aspect ratios, trapezoids, T- shaped blades, etc. The blade plan forms selected are such that extreme blade shapes are tested. For example, two T shaped blades are tested with one blade shape having most of the area close to the blade root while the other having most of its area towards its tip while both of them have the same projected area as well as the same blade length so that they can be compared at the same tip speed ratios.

Table 7.1: Blade shapes proposed for experimental testing

S.No.	Shape	Length	Root width	Mid width	Tip width	Area
1	Rectangle - 1	160	60	60	60	9600
2	Rectangle - 2	160	30	30	30	4800
3	Rectangle - 3	80	120	120	120	9600
4	Rectangle - 4	80	60	60	60	4800
5	Rectangle - Holes	160	60	60	60	9600
6	Trapezoid - 1	160	90	60	30	9600
7	Trapezoid - 2	160	30	60	90	9600
8	Diamond	160	30	75	30	9600
9	T shape - 1	160	120	30	30	9600
10	T shape - 2	160	30	30	120	9600
11	Plus shape	160	30	120	30	9600

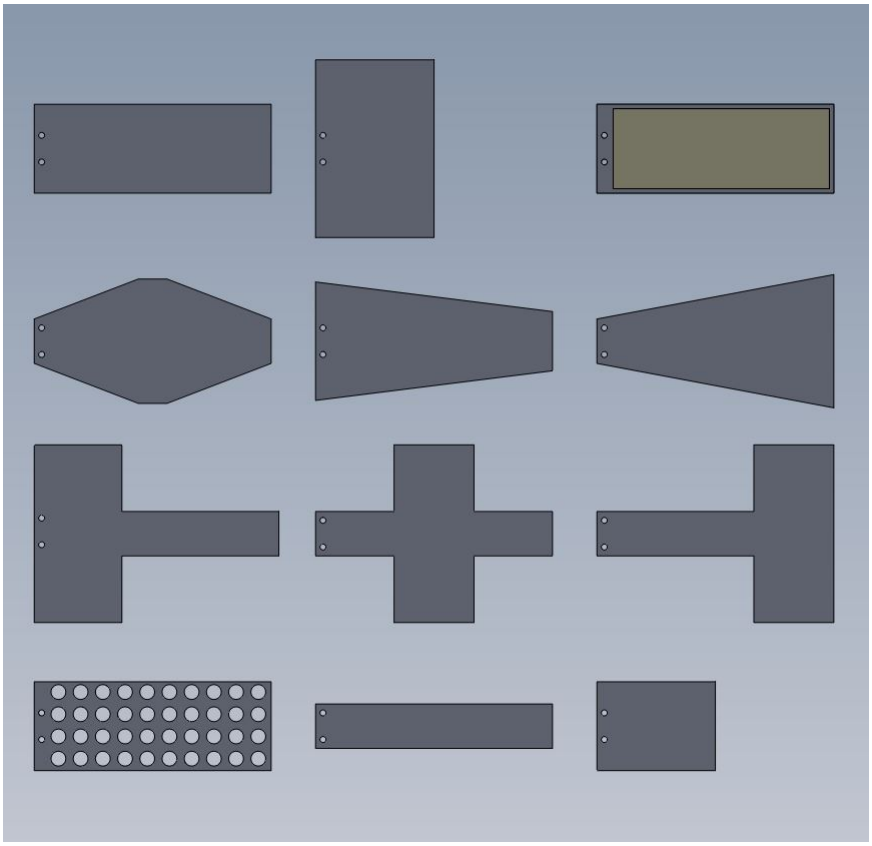

Figure 7.1: Different blade shapes proposed for testing to determine the optimal blade shape.

7.1.3 Water Channel

The Cyclic pitch turbine prototypes are tested in a water channel at Rutgers University, Mechanical and Aerospace Engineering Department for functionality tests and to quantify turbine performance. Several parameters like average and instantaneous rotational speed, torque output are measured from which torque and power coefficients are calculated. The Savonius turbine, as well as several blade shapes for CPT turbine, are tested as well.

Water channel layout

The water channel, as shown in Fig. 7.2, is a recirculating type water channel with a controllable pump to change flow velocity. The maximum flow velocity in the channel is 0.4 m/s (Re = 24,000) and can be filled up to a water depth of 1200 mm. The turbine is located in the long test section suspended upside down. The water channel has a reservoir where the water is collected before being pumped back into the channel. A pair of honeycomb meshes removes the turbulence in the flow before the water converges as a laminar flow into the test section. The width of the test section is 560 mm and the height of the glass panels is about 1500 mm high from the base of the water channel. A pump controller with a knob aids in adjusting the frequency of the pump to control the flow rate and consequently the flow velocity. Calibration of the water channel flow velocity is done by tracing neutrally buoyant particles in water using PIV technique.

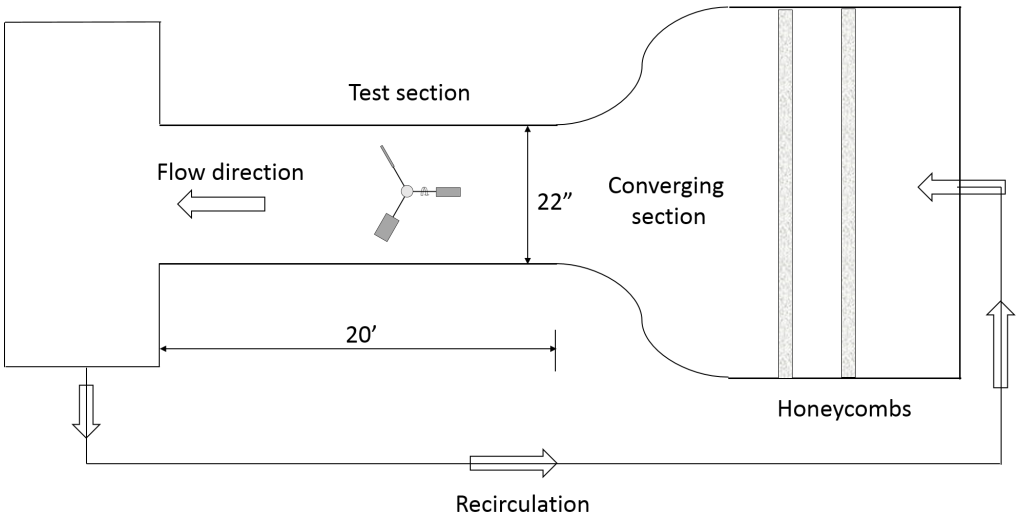

Figure 7.2: Top view sketch of the water channel indicating the test section, flow direction and location of the turbine.

Experimental setup

Multiple experimental setups are used, depending on the test being conducted, which includes the turbine and the measuring instruments as shown for example in Fig. 7.3. The turbine is vertically suspended upside down in the water channel and the turbine's drive shaft extends up out of the water. The turbine's drive shafts connects, via a set of pulleys with a toothed belt, to a gearbox. This step-up gearbox, with a $\sim$50 gear ratio, transfers power from the pulleys to a DC motor used here as a generator. A voltmeter, ammeter, and a potentiometer are in a circuit along with the generator. The ammeter is connected to a pc to record current readings. Water is filled up to a height of about 600 mm resulting in a blockage of about 8.5 % considering a 160×60 mm blade and the support structure used.

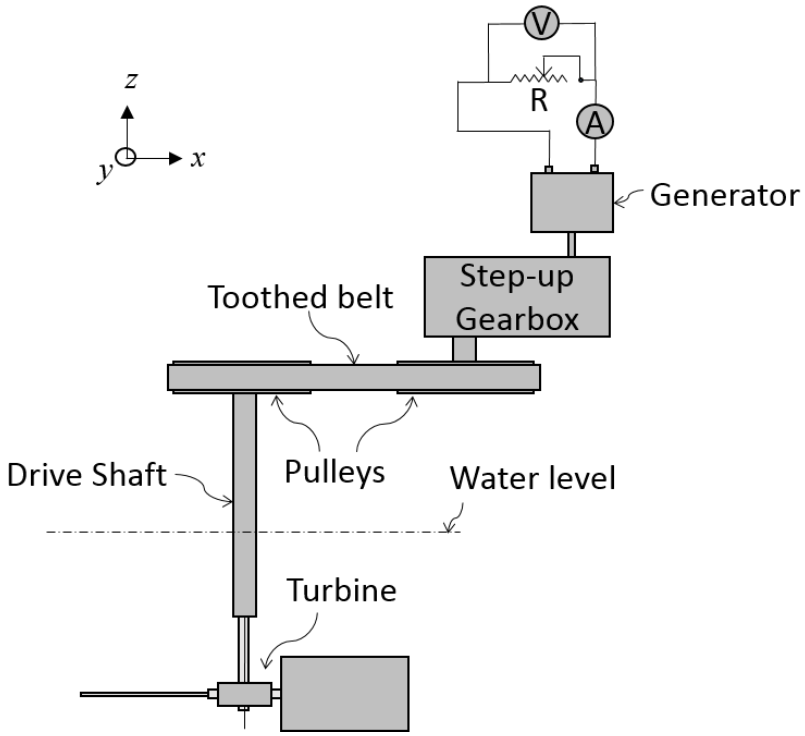

Figure 7.3: Front view sketch of an experimental set up used to test cyclic pitch turbine in the water channel.

A sophisticated torsion sensor is used in another experimental setup in the water channel to measure the true torque output directly instead of the dc generator setup for which the generator constants are unknown. A clutch style slip disc brake dynamometer is built that can deliver an adjustable load on the turbine through a screw and a spring. It consists of two machined matching plates which act like a clutch. The top plate is facing down and is rigidly fixed to the torsion sensor above it. The second is concentric to the first plate and is directly under it. It is fixed rigidly to the driven shaft which rotates along with the turbine. When the spring is compressed using the screw, the top plate applies more force onto the bottom plate creating more friction and a corresponding higher torque loading on the turbine. This setup also includes an optical rotary encoder to measure turbine rotational speed. An Arduino and torque sensor chip is used for the acquisition of rotary encoder and torsion sensor data.

Experimental procedure

The operating procedures for the two experimental setups in the water channel are discussed below. The proof of concept and torque and power output trend determination is done using the electrical generator setup shown in Fig. 7.3. For a fixed fluid flow velocity, resistance, R on the potentiometer is varied and current I in the circuit is recorded from a multimeter onto a computer. Power output P, from the turbine is calculated using Eq. 7.1. Resistance is varied to vary the turbine load and speed or the pump controller is adjusted to change the flow velocity before recording more current readings. The load applied, T to the turbine by the generator depends on the resistance offered by the potentiometer and motor constants, Φ and K_T, as given by Eq. 7.2.

$$P = I^2 R \tag{7.1}$$

$$T = \Phi K_T I \tag{7.2}$$

For the torsion sensor experimental setup, the spring load on the clutch is reduced to its minimum value to be able to obtain the highest turbine speed. The flow speed is adjusted in the water channel, using the pump controller, to the lowest possible setting where the turbine starts to rotate under the smallest loading. The torque and rotational speed readings which fluctuate due to sensor noise and cyclic variations of the turbine and instruments are recorded for over 5 minutes or 300 seconds to obtain a good average value using an Arduino onto a pc for post-processing. Average Power output is calculated from the average of the recorded readings using Eq. 7.3.

$$P = T\omega \tag{7.3}$$

7.1.4 Wind Tunnel

Experiments are conducted in an open-return type low-speed subsonic wind tunnel at Rutgers University. Turbine performance parameters like coefficient of power, the coefficient of torque as well as rotation speeds of different blade shapes are measured. Due to the lower density of air compared to water, larger flow velocities of up to 15 m/s (Re = 61,000) were tested and as a result higher rotation speeds are achieved. Description of the wind tunnel and the experimental setup and procedure is given below.

Wind tunnel layout

The wind tunnel used is similar to the one shown in Fig. 7.4 and the exit vents out of the room into the outside which sometimes affects the wind speeds inside the tunnel during wind gusts. The wind tunnel is a suction type, which helps to avoid turbulence caused by the rotating fan in front of the test section. The length of the wind tunnel is about 8 m with a 600 mm square test cross-section. The test section has slots at the wind tunnel base to mount or screw the test device. It also has a few small slots to insert sensors into the test section. The test section has glass doors on either side as well as a glass panel on the top to observe the turbine motion inside the wind tunnel during operation. The wind tunnel has a fan frequency controller to adjust the air flow velocity.

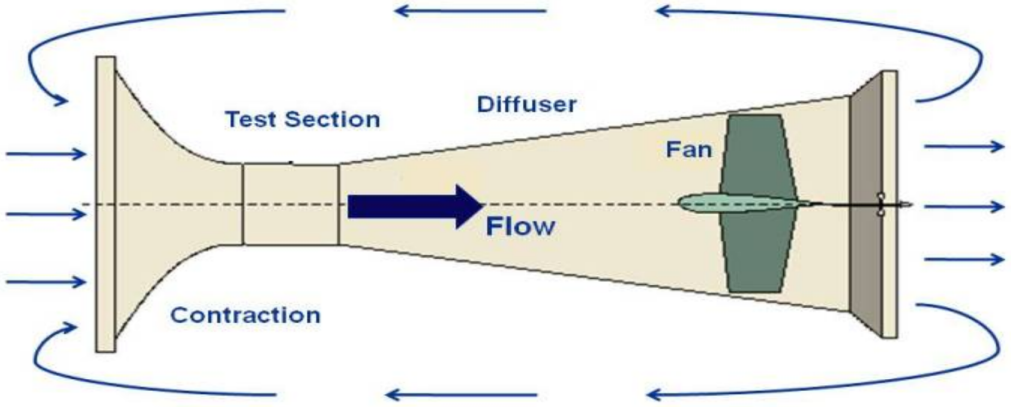

Figure 7.4: A representation of an open return type wind tunnel used for the CPT experiments. Reference: www.grc.nasa.gov

Experimental setup

The wind tunnel test setup involves the cyclic pitch turbine mounted on an acrylic cylindrical tower which is mounted onto the wind tunnel base as seen in Fig. 7.5. The support structure, the cam mechanism, and a 160 × 60 mm blade lead to a blockage of about 9 % at which some deviation from true results is expected (Ross & Altman, 2011). yet, using the same blade size helps to maintain same blockage ratio which results in consistent variations in measurements. The two narrow support arms extending into the test section as seen in the figure behind the turbine tower are lowered to the maximum extent possible and remain in the same location for all the experiments conducted. The airspeed/ fan speed controller and the display board can also be seen in the picture in the lower left corner. The CPT turbine's shaft running through the center of the acrylic tower is coupled to a driven shaft using a plastic precision flexible coupling. The steel driven shaft extends out of the wind tunnel base through a slot where a rotary encoder is attached which detects every rotation of the turbine and the time taken for each. A load sensor, pulley, dead weight and a nylon string connecting these parts act together as a rope brake dynamo-meter and is used to measure the torque output of the turbine. The aluminum pulley of diameter D

units is mounted and fixed to the steel driven shaft, onto which the nylon thread of diameter, d loops around a couple of times to provide frictional torque load on the shaft. One end of the nylon thread is attached to a variable dead weight, under the wind tunnel base, through a vertical pulley which is free to rotate. The other end of the nylon thread is perpendicularly attached to a load cell which measures the frictional force on the driven shaft by the nylon string when properly calibrated. The load on the turbine is increased by increasing the dead weight or by having additional loops of the strings over the pulley. A self-calibrating hot wire anemometer is inserted through one of the slots on the top wall 50 cm in front of the turbine at the same height as the turbine blades in the test section to measure and record the average airspeed reading once every second onto a pc. The pc also records string tension and turbine rotational speed readings from the load sensor and the rotary encoder through an Arduino and a load sensor HX711 chip.

Figure 7.5: Test section of the wind tunnel showing the mounted cyclic pitch turbine and the controllers.

Experimental procedure

The wind tunnel experimental procedure to test CPT involved adjusting the load on the driven shaft, calibrating the instruments, adjusting wind tunnel speed and data collection. It involves many iterative steps to obtain the right amount of loading on the turbine using the dead weight W and the rope brake. The tension in the string directly impacts the loading on the turbine shaft which helps adjust the rotational speed of the turbine. The electronics are turned on and the hot wire anemometer and the load cell readings are tared at zero loading and reset. Then, the fan in the wind tunnel is sped up using the controller to obtain a certain required wind speed in the wind tunnel. Then, using the Arduino setup and the anemometer connected to a pc, data is collected for about two to three minutes to obtain a reliable average reading from the anemometer, the load cell, and the rotary encoder. The load cell reads the dead weight loading W when the wind tunnel is off. When the turbine starts to rotate, the frictional force between the nylon thread and the pulley reduce the load sensor reading and a new lower reading S is indicated by the load cell and is used to determine the brake torque output T from the turbine using Eq. 7.4 (Al-Faruk & Sharifian, 2016), (Mahmoud *et al.*, 2012), (Kadam & Patil, 2013). Using the torque output and turbine rotational speed, N from the rotary encoder's reading, brake power output, P is determined using Eq. 7.5. The experiment is stopped and repeated if any external wind gusts affect wind speeds in the tunnel during an experiment. Once the data collection is done, the data is saved and the setup is adjusted for another experiment by adjusting either the wind speed, load on the turbine or by changing the blades of the turbine to test a differently shaped blade. Turbine rotational speed comparison experiments for testing multiple blade shapes exclude the rope brake dynamo-meter and involve measuring just the turbine rotational speed using a laser tachometer.

$$T = (W - S)\frac{D + d}{2} \tag{7.4}$$

$$P = \frac{2\pi NT}{60} \tag{7.5}$$

7.1.5 Evaluation Metrics

Several performance indicators of the cyclic pitch turbine are selected as evaluation metrics to test and compare different blade designs and fluid flow conditions. The selected evaluation metrics are:

- Average rotational speed
- Instantaneous rotational speed
- Tip speed ratio
- Torque output
- Coefficient of static torque
- Coefficient of dynamic torque
- Power output and
- Coefficient of power

The significance of these evaluation metrics is described below.

Average rotational speed

Rotation of turbine's blades, when exposed to a fluid flow, under any loading, is a proof to its ability to harness energy. For a fixed, known or unknown torque loading on a turbine, higher mean rotation speeds indicate higher power output and a higher coefficient of power with all other parameters like flow velocity and blade area being the same. Hence, when it is difficult to accurately measure torque output, a change in turbine rotational speed is chosen as a clear indicator of performance for a selected design. The average rotational speed of the turbine in different experiments was tested using different methods like post-processing of video recordings, manual stopwatch, non-contact laser tachometer or a high precision rotary encoder connected to a pc. Average turbine speed in rotations per minute, RPM is measured and plotted against fluid free stream velocity or the resultant Reynolds number considering the width of the blade to be the characteristic dimension.

Instantaneous rotational speed

Instantaneous rotational speed measurements are used to detect any variations in the observed turbine speeds in one cycle. In the theoretical modeling, the angular velocity of the turbine is kept constant and torque generated is allowed to vary in a rotation cycle. During experiments, the torque loading applied is kept constant while the turbine rotational speed is allowed to vary. Variations in instantaneous rotational speed are detected in experiments in the water channel based on the location of the blades with respect to the fluid flow direction. Such variations in the wind tunnel were absent due to higher average turbine speed and the rotating mass acting as a flywheel to normalize the fluctuations. US Digital E5 optical rotary encoder with 4096 ticks per rotation is used to accurately determine the speed variations in each cycle especially for the low speed water tunnel experiments. These variations are determined as a function of the azimuth angle varying from 0° to 360°.

Tip speed ratio

Tip speed ratio is calculated from the average rotational speeds of the turbine and the free stream fluid velocity. It is used as a non-dimensional alternative to average rotational speed comparisons between two designs. Tip speed ratio is used to compare results from experiments with different free stream fluid velocities and indicate turbine performance similar to turbine rotational speed. Tip speed ratios are plotted against the fluid flow velocity at which the experiment is conducted.

Static torque coefficient

The static torque coefficient is measured by constraining the turbine's driven shaft and measuring the torque generated by the blades on the shaft at different azimuth angles. A torsion sensor and a custom built slip disc clutch are used to measure the torque and consequently, the coefficient of static torque is calculated.

Dynamic torque coefficient

Dynamic torque coefficient is calculated from the torque readings measured while the turbine is allowed to rotate and it is plotted against the tip speed ratio. Since the torque is applied by the experimenter, the dynamic torque coefficient is closely known prior to the experiment. Yet, as a result, the turbine rotational speed and the tip speed ratio are affected. In general, the dynamic torque coefficient has an inverse relationship with the turbine rotational speed.

Coefficient of power

The coefficient of power is the most popular turbine metric and is a measure of efficiency and power output for a given flow velocity. It is measured using the flow

velocity and turbine power output and it is plotted against the tip speed ratio, λ, as well.

7.1.6 Uncertainity Analysis

Uncertainty analysis is an important consideration for experiments involving very small measurements as expected in our experiments due to its small scales. Errors in the experimental results arise from inaccuracies, low resolution and calibration errors, user errors related to measuring instruments (Gustavsson, 2017) like laser tachometer, hot wire anemometer, load cells and water flow velocity and blade length and width measurements. The errors could also be due to sampling errors or test procedural errors which are minimized by taking several readings for each data point and repeating measurements and in different orders. Uncertainty analysis of turbine speed, tip speed ratio measurements, the coefficient of torque and power calculations are conducted here. Table 7.2 indicates the accuracy and resolution specifications of the various sensors used. The uncertainty in blade dimensions is assumed to 1 mm and the accuracy of water velocity calibration is assumed as 3% of the measured value.

Table 7.2: Accuracy and resolution values of instruments used in the experiments

S.No.	Instrument	Accuracy	Resolution
1	Digital tachometer	±0.05%	0.1 RPM
2	Rotary encoder	±0.5%	0.1 RPM
3	Load cell	±2%	-
4	Torsion sensor	±0.3%	-
5	Hot wire anemometer	±3%	0.01 m/s

The uncertainty of rotational speed sensors is given to be ±0.05% of the value measured and for water channel experiments which involves rotational speeds of about 10 RPM, the error is $\pm 0.005 RPM\%$ which is lower than the resolution of the device which is 0.1 RPM. For the wind tunnel experiments having rotation speeds of more

than 100 RPM, the uncertainty is $\pm 0.05 RPM$ which is again less than its resolution. For tip speed ratio calculations, errors arise due to inaccuracies in blade length, flow velocity and turbine rotational speed measurements. For the water tunnel experiments considering typical values experienced, a variation of 0.03 in tip speed ratio measurements is observed which corresponds to a 4.3 % deviation from a value of 0.55. Wind tunnel experiments have an uncertainty value of 5.0% for tip speed ratio measurements.

When torque is measured in the wind tunnel using the rope brake dynamometer, a 2.4% uncertainty in measurement is observed due to the uncertainties in the measurement of the diameters of the pulley and the rope and the inaccuracies in the load cell readings. A 10.2% and a 9.7% uncertainty in measurements are observed in C_T and C_P respectively for the wind tunnel tests. Similarly, a 9.9% and a 9.4% uncertainty lies in C_T and C_P measurements respectively for the water channel experiments. Some of the errors in measurements are merely biases which shift the values for all experiments but still hold the comparisons especially when the tests are conducted successively.

7.2 Results

Experiments conducted on the cyclic pitch turbine in the water channel and the wind tunnel show proof of concept of the energy harvesting device as well as validate the analytical model developed in chapter 3. The results give insight into the characteristics and trends of the turbine as well as its performance under various flow and load conditions.

7.2.1 Proof of Concept Tests

Proof of concept experiments conducted on the first prototype in the water tunnel uses the dc generator setup to prove the functionality and to determine the torque and power output trends. The flow velocity, u is increased from 0.17 m/s (Re = 10,200)to a max value u_{max} of 0.23 m/s (Re = 13,800)in the water channel while current measurements are recorded. Normalized power output, P is plotted versus normalized fluid flow velocity in Fig. 7.6 (a) which shows that power output increases monotonically to a maximum value, P_{max} and seemingly linearly in the range of fluid velocities tested. It is to be noted that the energy in a fluid flow is proportional to the cubic power of the flow velocity and is plotted alongside for reference. Blockage factor corrections which tend to increase the local fluid flow velocity and hence the power output is not considered in the calculations. Power output, for a fixed flow velocity, from the CPT turbine for torque loads T up to a maximum torque loading, T_{max} on the turbine applied through a rheostat is shown in Fig. 7.6 (b). The measured values are joined using a shape-preserving curve and it shows that the turbine captures maximum energy from a fluid flow at an optimum load/torque value which corresponds to a certain optimal rotational speed and tip speed ratio. Both plots indicate that the turbine performs similar to conventional wind turbines whose power output increases with wind speed and have their certain peak performance at some intermediate load values or wind speeds (Bowen *et al.*, 2009). And similarly, for the same reasons, these results also do not indicate any deviations from the theoretical formulation developed in chapter 3. The following experiments involved the use of only the second prototype fabricated and described in the previous chapter.

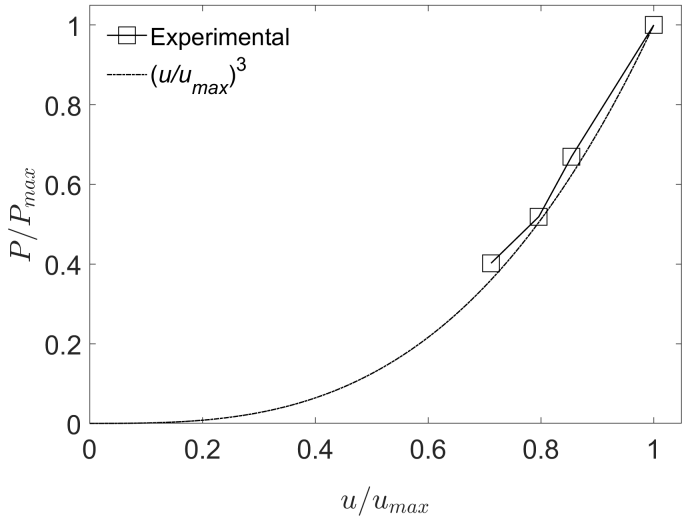

(a)

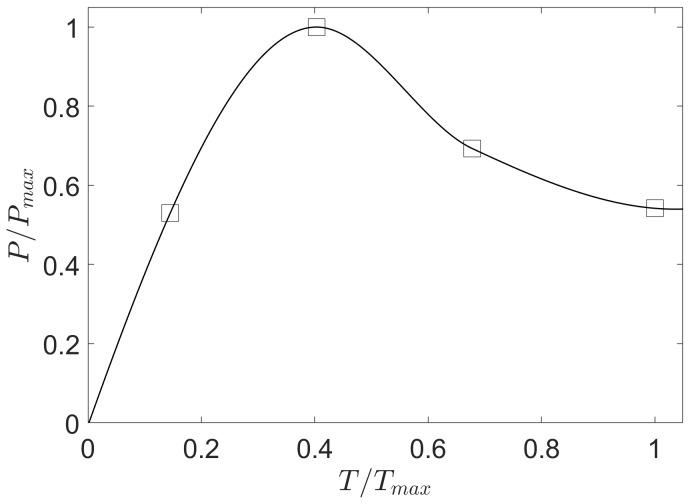

(b)

Figure 7.6: Water channel experimental results showing (a)Power variation with changing fluid velocity and (b) Power output variation with applied torque.

7.2.2 Water Channel Results

The torsion sensor setup is used to measure instantaneous as well as the mean rotational speed of the turbine, static torque coefficient, dynamic torque and power

coefficient of the CPT prototypes with the rectangular 160 × 60 mm blades. The following plots characterize the mean as well as instantaneous cyclic properties of the CPT turbine.

Static torque measurements

Static torque is measured by braking the turbine prototypes at several azimuth angles to determine the self-starting behavior and also to observe the improvements made in the second prototype. Figure 7.7 (a) and (b) show the measured static torque outputs for the first and the second prototype. Three flow velocities are investigated from 0.22 m/s to 0.31 m/s which correspond to Reynolds numbers ranging from 13,200 to 18,600 and they show similar trends with increasing magnitude for a higher flow velocity. The readings for each flow velocity show three peaks and three troughs due to the presence of three blades. The peaks in static torque readings are observed when a blade is perpendicular to the flow which occurs at azimuth angles 0°, 120° and 240° (Rao & Diez, 2017) and the troughs are located in between any two peaks. It should be noted that these three azimuth angles relating to the location of the reference blade form the same configuration since the blades are 120° apart. This peak and trough behavior is typical of any drag or vertical axis turbine with the number of peaks in one rotation cycle in the static torque plot being equal to the number of blades on the turbine (Ali, 2013). Also, the magnitude of static torque is positive at all azimuth angle indicating that the turbine is always self-starting. Comparing the two plots, it is clear that adding bearings and reducing the active drive stroke angle increases the static torque values which implies a higher power output and a higher coefficient of power of the turbine.

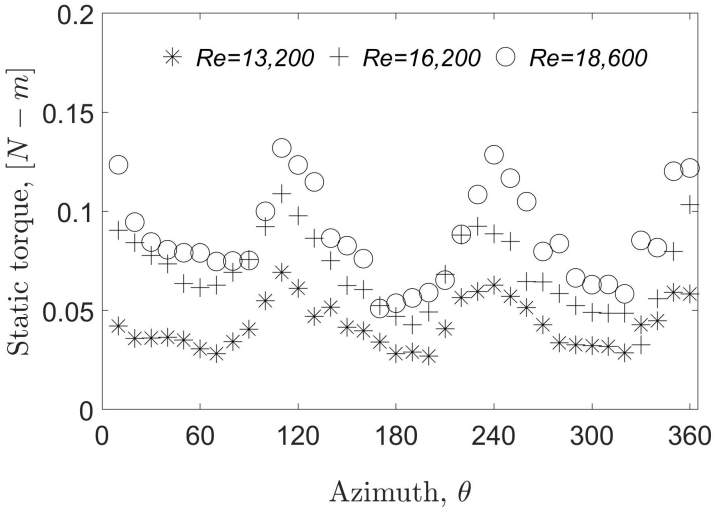

(a)

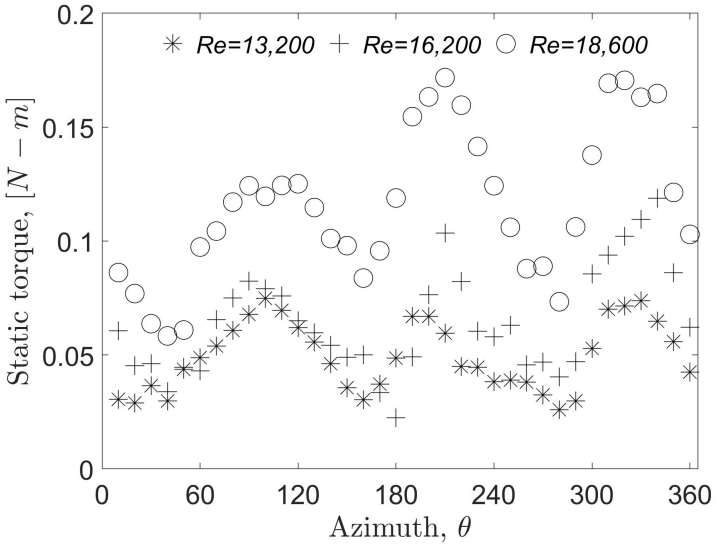

(b)

Figure 7.7: Static torque measurements at several azimuth angles for CPT prototypes 1 (top figure) and 2 (bottom figure) in order tested in water at several flow velocities.

Similarly, the static torque coefficient for the second prototype is plotted in Fig. 7.8 and compared to the theoretical values obtained in chapter 4. The plot shows that the 3 individual sets of values corresponding to the three velocities shown in Fig. 7.7 (b) collapse into almost one band of values. The crest and trough pattern

still remains with 3 peaks similar to the theoretical results. Also, the maximum and minimum values for the coefficient of static torque match very closely with the theoretical values albeit a small shift in the azimuth values.

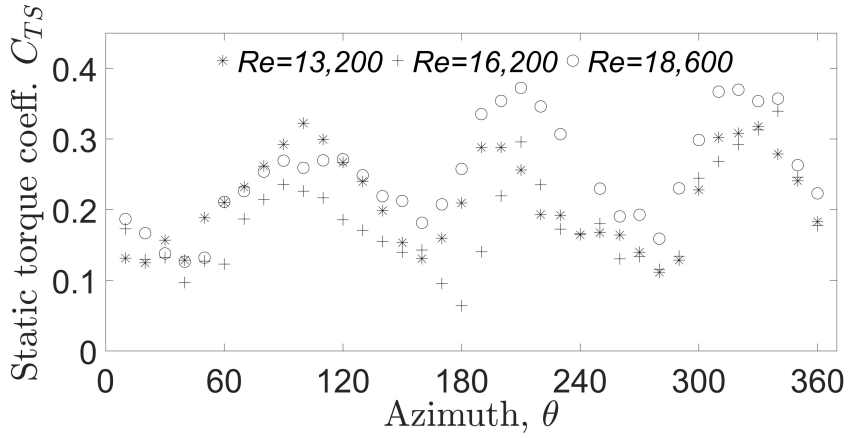

(a)

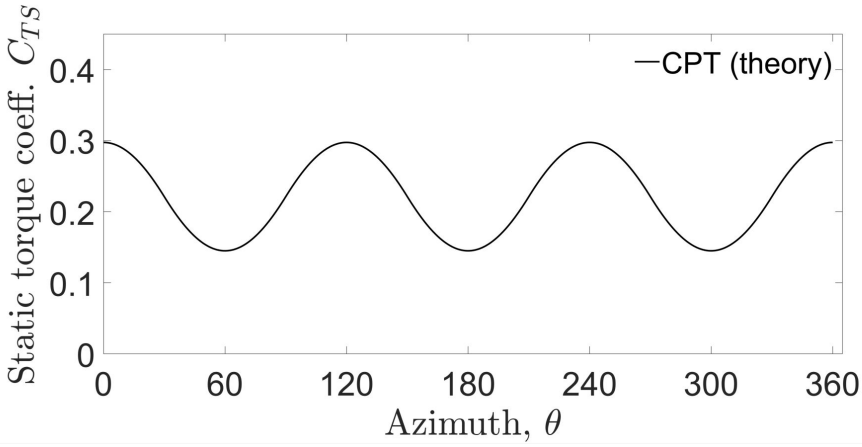

(b)

Figure 7.8: Static torque coefficient of a 3 bladed CPT turbine at several azimuth angles for one rotation cycle obtained from water channel experiments for 3 different flow velocities and theoretical results from the developed mathematical model.

Mean and instantaneous rotational speeds

In separate tests, prototypes 1 and 2 are allowed to freely rotate to observe the rate of increase in rotation speed under no load condition while the flow speed is increased in steps. Figure 7.9 indicates the no-load rotational speed readings when

the flow velocity is increased from 0.17 m/s (Re = 10,200) to 0.34 m/s (Re = 20,400). The plot indicates that the turbine rotational speed monotonically increases for both prototypes. It increases from about 5 RPM to 14 and 10 RPM respectively for the first and second prototypes for the tested free stream velocity range. The trend is almost linear as well which is typical of wind turbines. Though the turbine is undergoing free rotations and does not generate any power, frictional torque in the mechanism still exits and consumes some power. Similar results with lower slopes are observed when a constant load acts on the turbine and power is being generated.

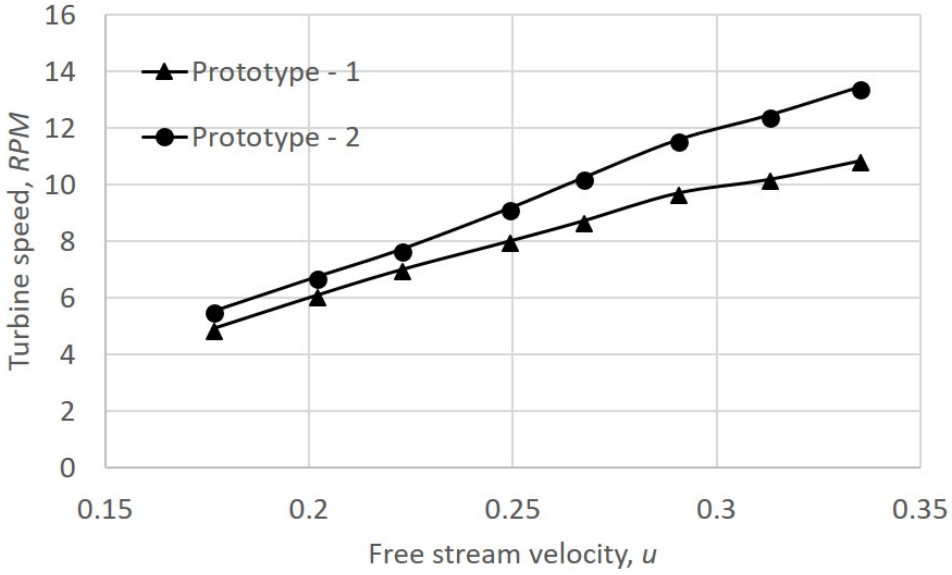

Figure 7.9: No-load mean rotation speeds of prototype - 1 and Prototype - 2 while free stream velocity is increased in steps.

The rotational speed of the CPT turbine varies depending on its azimuth location as the blades rotate around the turbine axis. It is called the instantaneous rotational speed and is in addition to the variation in average turbine rotational speed which is a result of changing free stream velocity. When the load is kept constant, the turbine blades rotate at different speeds at different azimuth locations in reaction to the varying relative normal velocity and the consequent forces on the blades. Figure

7.10 depicts the cyclic variations in rotational speeds for prototype 2 by plotting instantaneous turbine speed for one whole rotation. The trend is similar to that of the static torque plot shown in Fig. 7.7. It depicts the three peaks and three troughs located at the same azimuth angles of 0°, 120° and 240° where one of the three blades experiences maximum normal relative fluid velocity. Also it can be seen that when the free stream velocity is increased from 0.22 m/s (Re = 13,200) to 0.29 m/s (Re = 17,400) and then to 0.31 m/s (Re = 18,600), the readings shift up indicating an increase in the mean turbine rotational speed. A shift in the peak values by about 10 to 15 degrees to the right for the highest free stream velocity tested is observed indicating a slight delay in rotational speed increase as a result of higher force at the above-indicated azimuth angles.

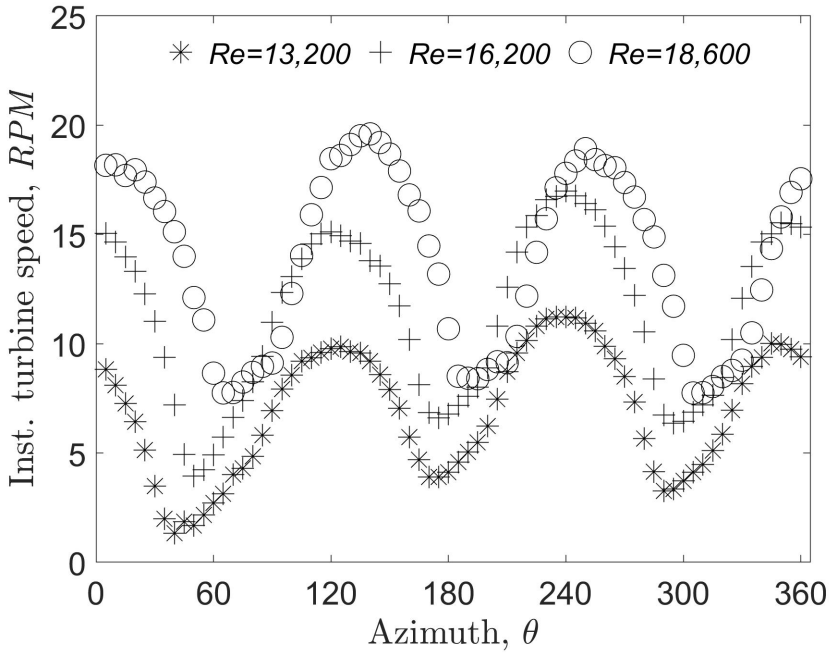

Figure 7.10: Variation in instantaneous rotational speeds of CPT turbine in one complete rotation.

Coefficient of torque

The coefficient of dynamic torque is measured for the CPT turbine and compared to the theoretical model to validate the equations developed. Figure 7.11 shows the experimental values for two free stream velocities $u = 0.29m/s(Re = 17,400)$ and $u = 0.33m/s(Re = 19,800)$ and the values calculated from the theory for an active drive stroke angle of 160°. It is observed that the experimental measurements align very well with the theoretical values calculated for most of the optimal tip speed ratios The coefficient of torque values gradually reduce with increase in tip speed ratio as expected since torque and speed are inversely related. When the turbine rotates faster resulting in higher tip speed ratios, the prototype underperforms compared to the theory and the causes for this could be the increase in mechanism friction and the blade pitching motion losses.

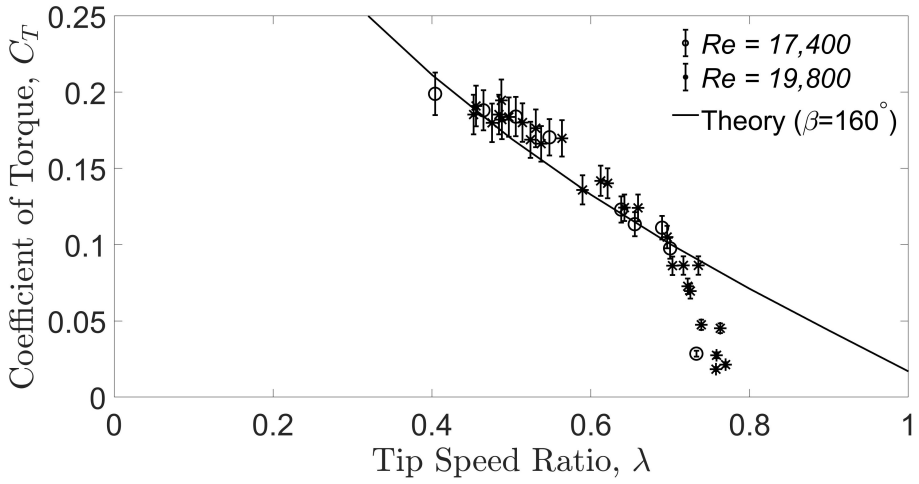

Figure 7.11: Coefficient of torque values for CPT turbine calculated from water channel experiments and compared to those from the developed theory.

Coefficient of power

Similarly, the coefficient of power for CPT turbine is calculated from experimental measurements and compared to those from the theory. The rectangular blade of

dimensions 160 × 60 mm blades are used for the experiments and the results are plotted in Fig. 7.12. The same two free stream velocities are tested by varying the load on the turbine to achieve different rotational speeds. A maximum C_P value of about 10% is observed in the experimental results close to a tip speed ratio of about 0.5. Lower tip speed ratios are hard to obtain since the turbine stalls at higher loads due to a degrading performance. The experimental and analytical power coefficient values have similar maximum magnitudes and the peaks are observed around the same tip speed ratio. Yet, similar to torque coefficient values, the trends diverge at higher tip speed ratios where an increase in losses is expected due to mechanism friction and blade pitching which are not considered in the mathematical model.

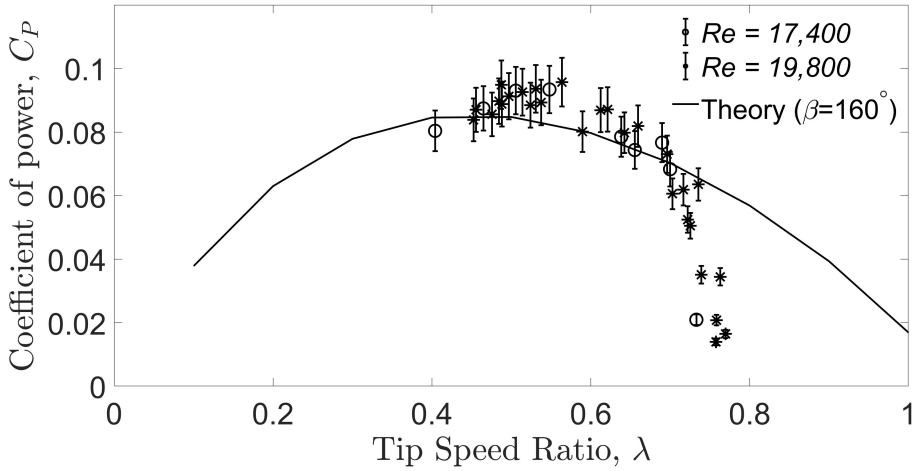

Figure 7.12: Coefficient of power values for CPT turbine calculated from water channel experiments and compared to those from the developed theory.

7.2.3 Wind Tunnel Results

Experiments in the wind tunnel are conducted to observe the cyclic pitch turbine characteristics in air and compare the performances of different blade shapes. Since the air density is comparably very small to that of water, higher flow speeds, corresponding to higher Reynolds numbers, are required and as a result higher rotation rates are expected. Several parameters measured are plotted in the following sections.

Mean rotational speeds

Rotation rates for the rectangular blade under zero load are measured in the wind tunnel to determine the rate of increase in rotational speed with an increase in wind speeds. The tests are repeated several times, each indicated by a different color, to test the repeatability of the results as shown in Fig. 7.13. Results from all tests match very closely indicating that rotational speed measurements as a valid performance indicator. Turbine rotational speed values increased from about 45 RPM at 4.5 m/s (Re = 18,200) which is the minimum starting wind speed to about 180 RPM at 9 m/s (Re = 36,500). Turbine rotational speed increased at a rate of about 26 RPM for every 1 m/s increase in wind speed. The tip speed ratio values increase at a faster rate at lower wind speeds and stabilize at about a value of 0.4.

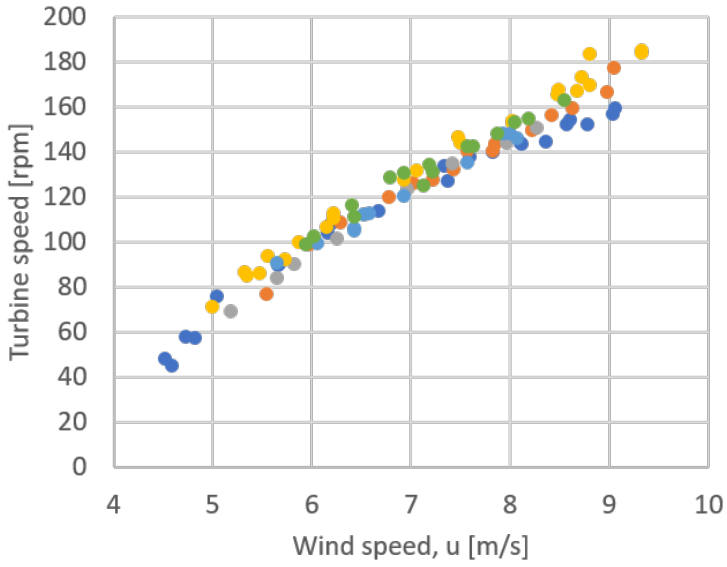

(a)

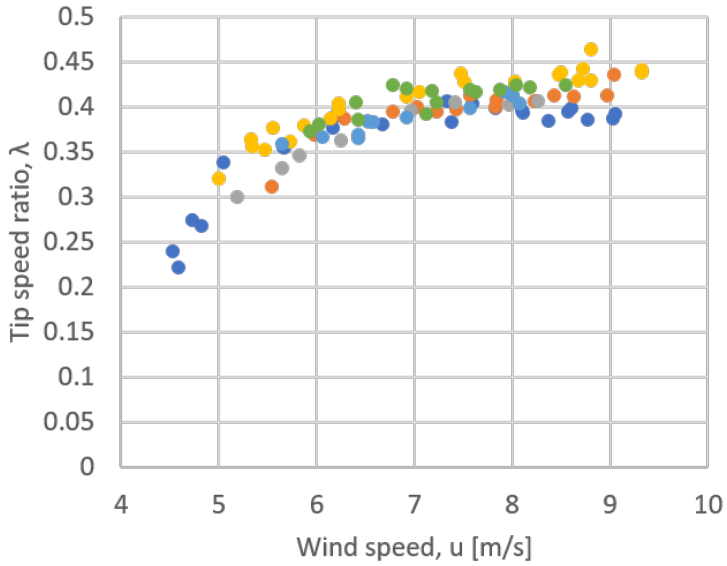

(b)

Figure 7.13: Mean rotational speeds measured and tip speed ratios calculated for rectangular 160 × 60 mm blade for various wind speeds from 6 independent tests indicated using different colors.

Coefficient of torque

The coefficient of torque from dynamic testing is calculated using wind tunnel experiments for a rectangular blade of dimensions 160 × 60 mm. The dead weight is fixed and the wind speed is changed from about 6.5 m/s (Re = 26,400) to 10 m/s (Re = 40,500) to obtain the plotted data points as shown in Fig. 7.14. The torque coefficient is plotted against the tip speed ratio and the results show the same trend as seen from water tunnel testing and acts as a continuation to those values. The torque coefficient values decrease from about 0.4 to about 0.23 for tip speed ratio increase from 0.15 to 0.35.

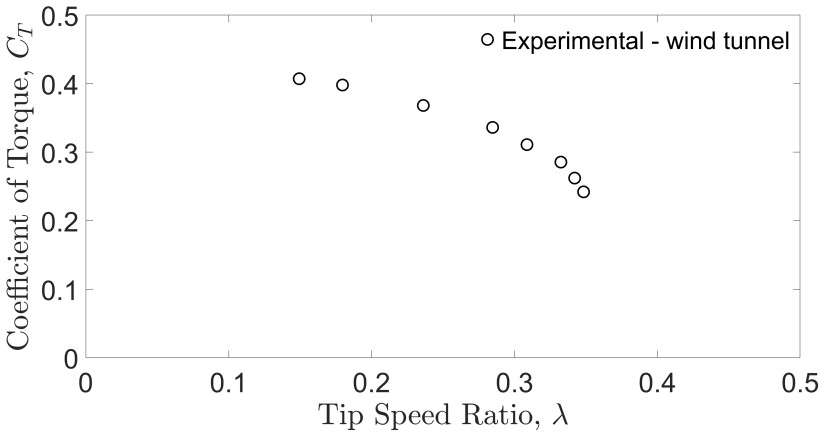

Figure 7.14: Coefficient of torque values from wind tunnel testing of CPT turbine using rectangular 160 × 60 mm blades.

Coefficient of power

The coefficient of power is also calculated with 160 × 60 mm blades from the wind tunnel experiments. The maximum C_P value is close to 10% as shown in Fig. 7.15 which is similar to that from water tunnel experiments. The plot shows the C_P plotted against the λ and that, the C_P peak shifted to left to about 0.35 λ. The magnitude and shape of the curve still match very closely with the predicted values from the mathematical model as well as the water tunnel experimental results.

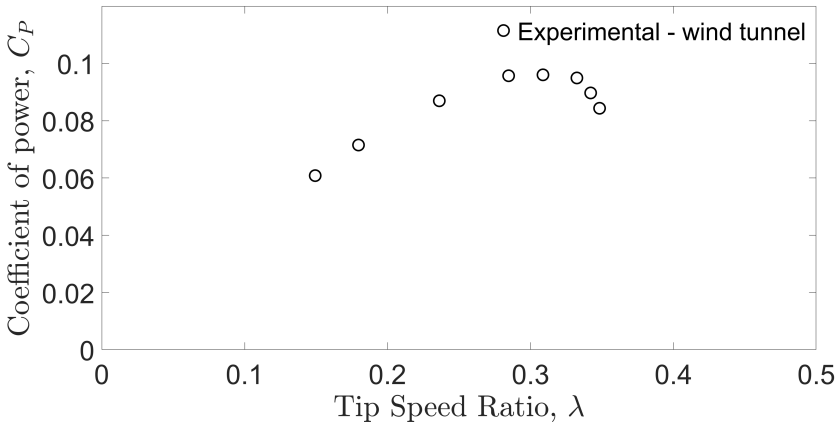

Figure 7.15: Coefficient of power values from wind tunnel testing of CPT turbine using rectangular 160 × 60 mm blades.

7.2.4 Blade Shapes

Several blade shapes depicted in Fig. 7.1 and their parameters listed in table 7.1 are tested in the wind tunnel to determine the best shape and dimensions for maximum and most efficient power generation. The tests include no-load rotational speed measurements, tip speed ratio calculations and torque and power coefficient calculation.

No-load rotational speeds

The no-load or free rotational speed measurements and tip speed ratios for several wind speeds ranging from 4 m/s (Re = 16,200) to about 10 m/s (Re = 40,500) in the wind tunnel for the different blade shapes (tabulated in table 7.1) tested is depicted in Fig. 7.16. The turbine blades overcome the mechanism friction while rotating and hence the free rotational speed measurements are an indication of power output and efficiency of the system when blade area is kept the same for different blades shapes. The change in blade area affects the efficiency calculations since a larger blade, even though is producing the same power as a shorter blade, it is working at a lower efficiency since it is absorbing energy from a larger area. Also, a larger blade

has more mass and has more mechanism friction to overcome.

From the figure, it can be noticed that the 160×30 mm blade with the highest aspect ratio of 5.34 rotates at the highest rotational speed indicating that long and narrow blades perform much better than the opposite dimensions as can be seen with 80×60 mm blades which have the same blade area but has much lower speeds. The 160×30 mm blades also outperform the regular 160×60 mm blades indicating they more power and have higher C_P as well. Comparing the two trapezoid shaped blades and the diamond shaped blades, it can be observed that the trapezoid with the wider side at the root and narrow side at the tip rotates faster and produces more power than the opposite shape. Also, at lower wind speeds, the trapezoid shape with the wider part near the root produces the highest rotational speeds. The diamond shape blade which is a transition shape in between the two and also has the same area falls in between at least for the higher wind speeds.

T shaped blades of the blade area (9600 sq. mm) are tested with the wide side towards the root as well as the tip. In addition, an intermediate shape "plus" is also tested to observe its performance. T shape with the wider side at the root performed slightly better than the opposite with the plus-shaped blades almost performing the same as the T shape blades with the wider side at the root. The reason for T and plus-shaped blades to be performing poorly could be a result of more blade area present far away from the blade pitching axis which causes the blades' edges to move at higher velocities during pitching motion resulting in more losses than narrow blades. This is more pronounced in the T shaped blade with more area towards the tip which moves at a higher velocity than its root. Rectangular blade with holes of the same blade area performed worse than the one without the blades. Rectangular blades with half the length and twice the width i.e four times the aspect ratio of the regular 160×60 mm blades performed the worst out of all the blades tested. Rectangular blades of area half as the regular blades with dimensions 80×60 mm are also tested and their

rotational speeds are slightly lower than that of the regular blades. Tip speed ratios for all those measurements are also indicated in the figure and show that a maximum tip speed ratio of about 0.5 is achieved for the long and narrow 160 × 30 mm blades and the rest of the blades fall around 0.4 or less with the lowest tip speed ratio for a maximum tested wind velocity of about 10 m/s (Re = 40,500) being about 0.25 for the blade that is half the length of the other blades. The results indicate the possibility that wider blades or having more blade area far away from the pitching axis of the blade could be resulting in lower rotation speeds and consequently lower performance. This could be due to the fact that the blades are pitching twice the number of times for every rotation and the blades need to push the fluid around them to be able to pitch which could cause aerodynamic losses which are not considered in the theoretical analysis.

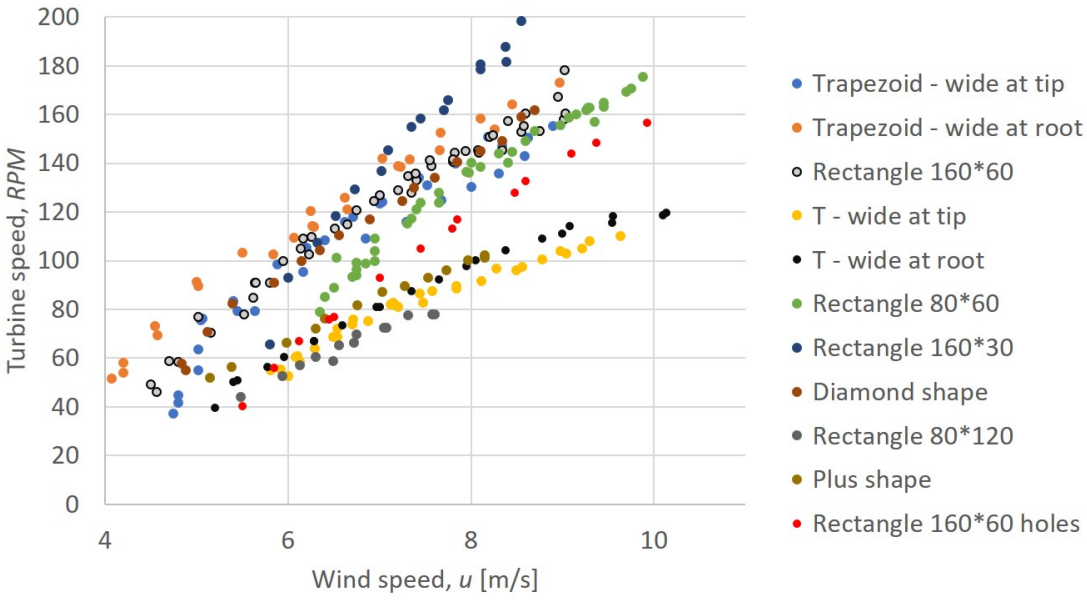

(a)

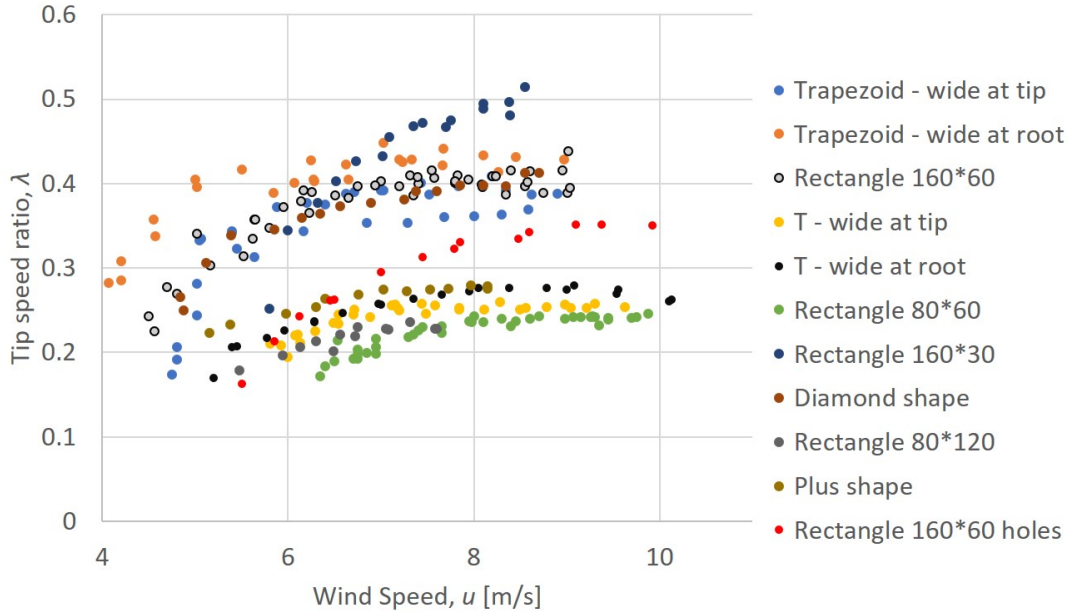

(b)

Figure 7.16: Mean rotational speeds and tip speed ratios for 11 different blade shapes tested in wind tunnel for wind speeds ranging from 4 m/s to 10 m/s (Re = 16,200 to 40,500.

Coefficient of torque

The coefficient of torque is measured for several blade shapes having the same blade area by having the same torque loading while changing wind speeds and conducting all the experiments in a single run. The results are plotted in Fig. 7.17 showing the coefficient of torque values for the rectangle, diamond, trapezoidal, plus and T shaped blades. All the tested blade shapes generate the same trend as observed in previous experiments for the coefficient of torque. The lowest performance is observed for T shaped blades with the wider part at the root of the turbine since most of the blade area is close to the root which does not generate large torque due to lower arm length. The highest coefficient of torque values for most of the tip speed ratios is observed for the trapezoid blades with the wider part towards the root of the blade which is consistent with free rotational speed measurements indicated in Fig. 7.16.

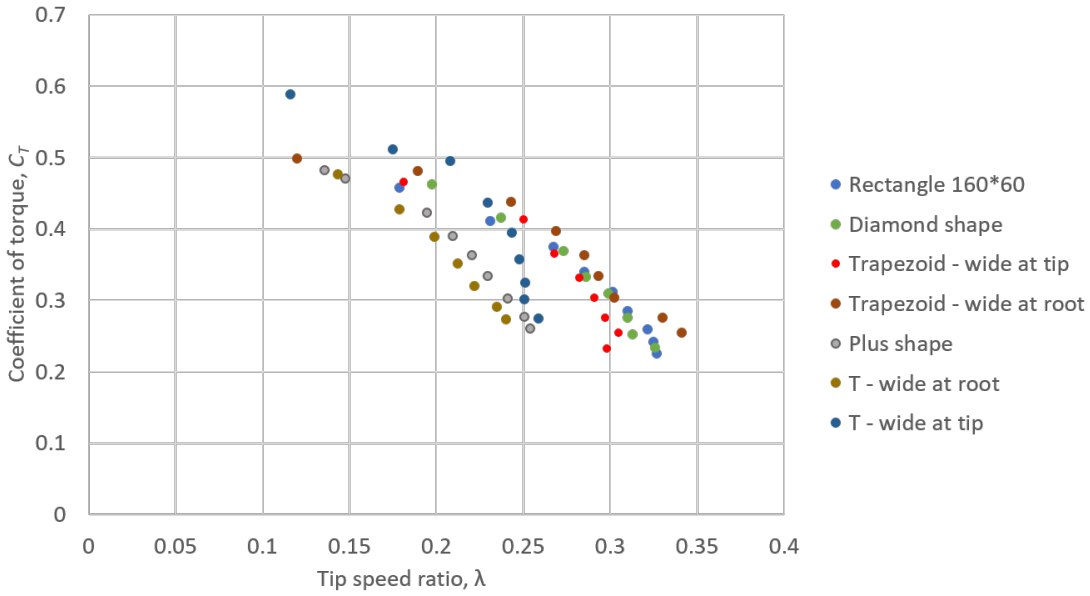

Figure 7.17: Coefficient of torque values from wind tunnel testing of CPT turbine for 6 different blade shapes having the same area.

Coefficient of power

The coefficient of power for the same blades is also calculated and plotted in Fig. 7.18. The results indicate a similar trend for all the blades to that of the one plotted for the rectangular blade but slightly shifted. Again similar to the coefficient of torque, highest coefficient of power is observed for the trapezoid shaped blades with the wider part at the root of the blade for most of the tip speed ratio spectrum observed and the lowest for the T shaped blades with the widest part at the root. The trapezoidal shaped blades with the wider part towards the tip of the blade perform slightly worse than the other trapezoidal shaped blades with the intermediate diamond shaped blades having C_P values in between the two as expected. Also, the plus-shaped blades have C_P values in between the two T shaped blades. The rectangular 160×60 mm blades are observed to be the second most efficient blades out of the tested blade shapes.

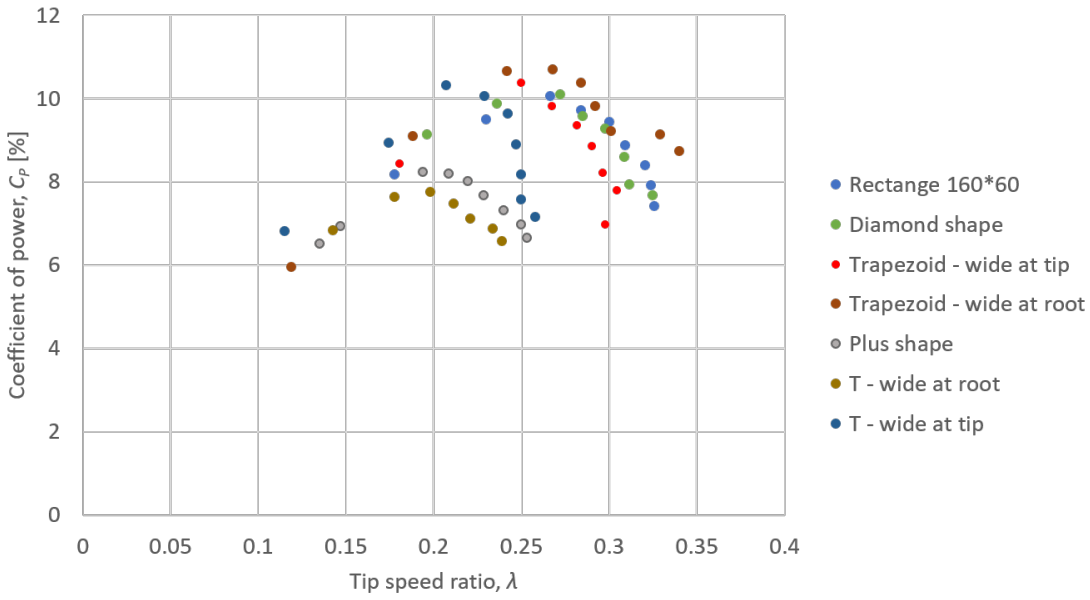

Figure 7.18: Coefficient of power values from wind tunnel testing of CPT turbine for 6 different blade shapes having the same area.

7.2.5 Airfoil Section Blades

Water channel free rotational speed measurements are taken by using elliptical airfoil sectioned blades and compared to the flat plates used so far. The rectangle 160×60 mm blade size is used and the elliptical airfoil blades are 3D printed with the same mass and also coated to have smooth surfaces. Elliptical airfoils, which are wings with camber are experimentally proven to have a lower coefficient of drag values at low (less than 10°) angle of attacks compared to wings without camber (Mueller & Torres, 2001) which could help minimize the recovery stroke drag force to improve performance. Also, it is shown that their drag coefficient at angles of attack less than 6° decreases with increase in angle of attack and has the least drag coefficient at an angle of attack of 4° (Sun *et al.*, 2015). Pressure drag dominates friction drag and together they combine to add up to a combined coefficient of drag value of about 0.025 (Sun *et al.*, 2015) which is negligible compared to a value of 1.2 for a vertical flat plate. No load rotation speed measurements are taken for about 10 complete rotations for both the blades for 4 different free stream velocities ranging from 0.29 m/s (Re = 17,400) to 0.36 m/s (Re = 21,600). The results are indicated in Fig. 7.19 along with uncertainty in measurements and it is observed that the airfoil sectioned blades performed better with a 14% to 24% increase in turbine rotational speeds over the flat plate blades. During the experiments, it is noticed that the flat plate blades were inclining by a couple of degrees and not perfectly horizontal during the recovery stroke while it was easier for the airfoil section blades to be held parallel to the flow during the passive stroke as indicated by Mueller & Torres (2001). This helps in reducing losses associated with recovery stroke drag and increase CPT performance as indicated by the plotted results.

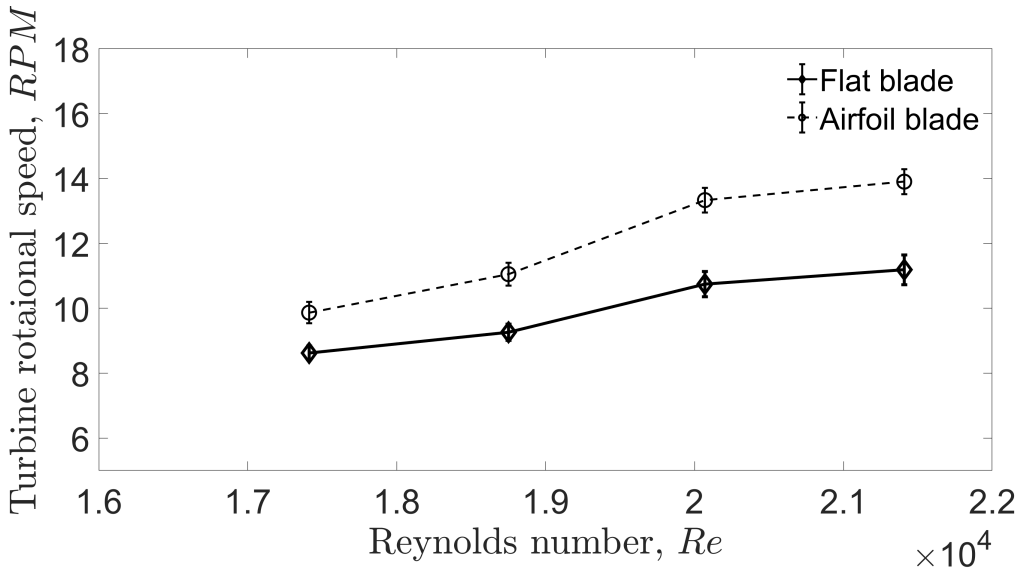

Figure 7.19: Mean turbine speeds for CPT with a flat plate blade compared to that of an airfoil sectioned blade in water channel testing.

7.2.6 Comparison to Savonius

The CPT turbine setup is used to test the Savonius turbine and compare with the CPT turbine in the water tunnel. Savonius blades are 3D printed to match the size, in terms of frontal area and length of the blades as shown in Fig. 7.20 to that of the 160×60 mm blades to which it is compared. It needs to be noted that, in this design, the bucket height is 40% that of the diameter and is not the most optimal aspect ratio for a Savonius turbine. The typical height of Savonius buckets ranges from one to four times the diameter of the buckets (Tang *et al.*, 2013). Other beneficial modifications to Savonius like end plates and overlap are also not utilized in this design. In order to use the same structure to test Savonius, the followers of the CPT cam mechanism are modified so that they do not pitch during turbine operation which, as a consequence reduces mechanism friction for Savonius. The Savonius turbine built is tested and compared to the CPT turbine and the measurements along with the uncertainty bars as shown in Fig. 7.21. The experimental results clearly show that the Savonius turbine rotated at a very low rate compared to that of the CPT. Yet, it was observed

that the turbine has much lower fluctuation in rotational speeds during each rotation cycle than that observed for the CPT turbine. This is due to the friction and energy needed to overcome the pitching motion which, if optimized will lead to lower losses and turbine speed fluctuations. These fluctuations also directly affect the loading on the different parts of the turbine and could cause the CPT turbine to have a lower fatigue life which is a structural concern and is not discussed here. As indicated before, no-load rotational speeds relate directly to the power output under the same torque loading and indicate the performance of a turbine. Hence, it can be stated that the cyclic pitch turbine has better power performance than a Savonius turbine.

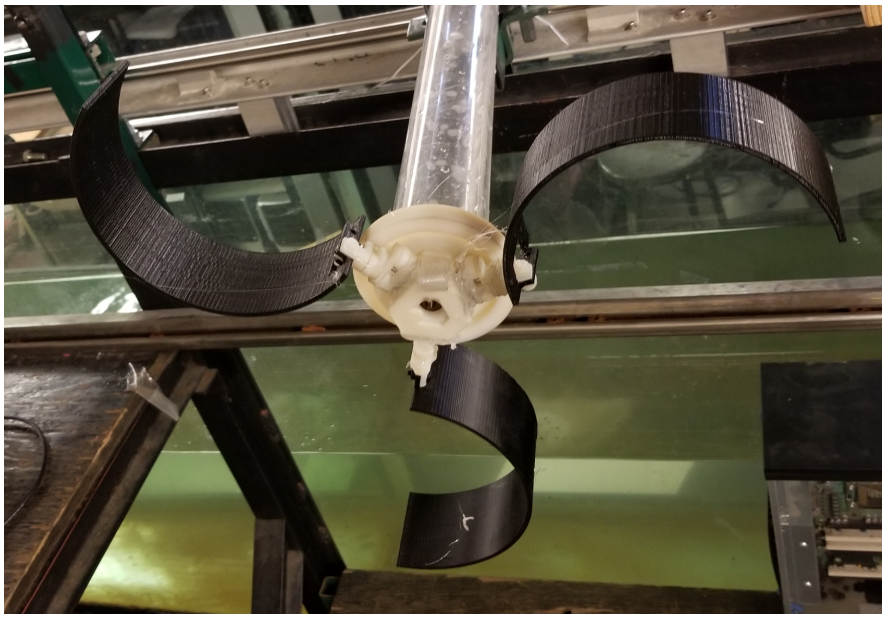

Figure 7.20: Three bladed Savonius turbine built for comparison with the CPT turbine.

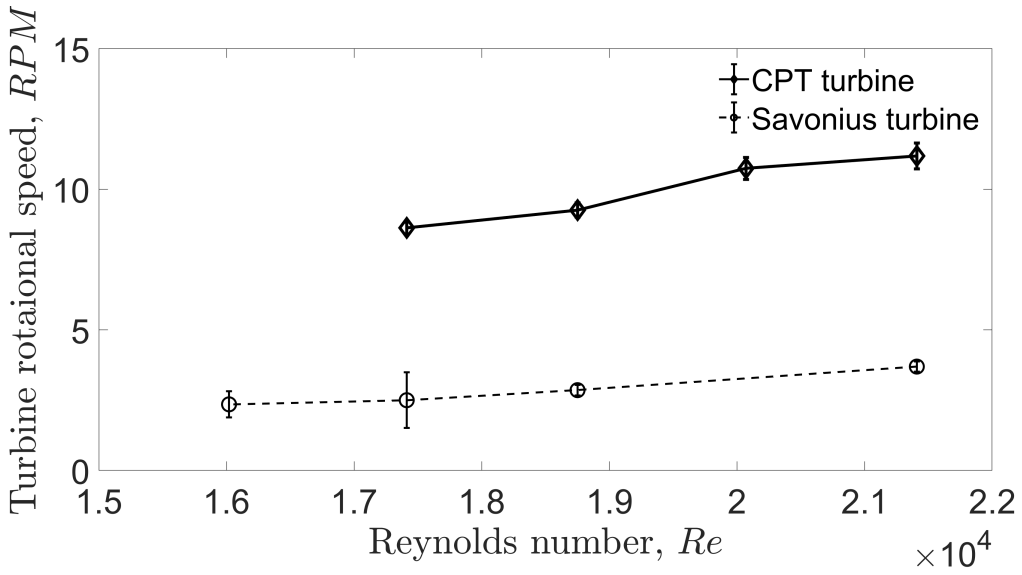

Figure 7.21: Mean turbine speed of a Savonius turbine compared to that of CPT turbine with regular flat plate blades from water channel experiments.

Chapter 8

Conclusion and Future Work

8.1 Conclusions

A novel vertical axis drag based fluid turbine called the cyclic pitch turbine (CPT) is conceptualized, modeled, built and experimentally tested. The turbine aims to eliminate recovery stroke drag force which adversely affects turbine performance as seen in drag based turbines like Savonius. Reduction of losses is achieved by using flat plate blades and utilizing the two strokes observed in the sport of rowing to harness energy from fluid motion. The turbine's drive stroke involves a vertically oriented turbine blade being pushed by fluid flow with maximum drag force and the blades moving upstream at 0° angle of attack to experience relatively negligible adverse drag during the recovery stroke. The important conclusions drawn from this work are:

1. A functional vertical axis drag turbine which uses blade pitching to achieve relatively negligible recovery stroke losses is conceptualized and built. A novel dual cam mechanism to achieve the custom blade pitching motion is also developed.

2. A theoretical model of the turbine is developed and validated by testing prototypes in a wind tunnel and a water channel. The developed equations show that CPT turbine has 7% higher and more uniform static torque coefficient values and indicate to a better dynamic performance compared to Savonius.

3. Optimization of turbine parameters indicates that an active drive stroke angle of $\beta \sim 140°$ and a tip speed ratio of $\lambda \sim 0.5$ result in optimal turbine performance.

4. Wind tunnel experiments show that long and narrow continuous blade shapes with less area towards blade tips result in better power performance of the turbine.

5. Water channel no-load turbine speed measurements indicate that CPT turbine outperforms Savonius turbine and that CPT turbine performs better with airfoil sectioned blades than with flat plate blades.

8.2 Future Work

This thesis stands as a proof of concept work on the novel cyclic pitch turbine to efficiently harvest energy from a fluid flow using the principle of drag maximization and minimization between the two strokes of a turbine using flat plate blades. The characteristics of the turbine make it apt for residential locations with lower wind speeds and with higher turbulence generated due to man-made structures and trees. Also, since the flow on the recovery side is not significantly disturbed, a second turbine at close proximity behind a first turbine could be used to harness energy which increases packing density. The turbine is also practical for energy harvesting from tidal flows and river streams where multiple stacks of the turbine could be used to capture energy from the entire height of the water column.

Areas of interest for future investigations on CPT turbines include:

- Understanding the effect of blade pitching speed and mechanism friction on performance and ways to increase turbine performance.

- Experimental testing of larger models to determine the effects of scaling for possible commercial use.

- Building a compact fully functional minimum viable product for energy harvesting from wind or water flow for emergency use in remote areas.

Bibliography

Abbott, Ira H, Von Doenhoff, Albert E & Stivers Jr, Louis 1945 Summary of airfoil data .

Adib, Rana, Murdock, HE, Appavou, F, Brown, A, Epp, B, Leidreiter, A, Lins, C, Murdock, HE, Musolino, E, Petrichenko, K & others 2015 Renewables 2015 global status report. *Paris: REN21 Secretariat* .

Akwa, JV, Vielmo, HA & Petry, AP 2012 A review on the performance of savonius wind turbines. *Renewable and Sustainable Energy Reviews* **16** (3), 3054–3064.

Al-Faruk, Abdullah & Sharifian, Ahmad 2016 Geometrical optimization of a swirling savonius wind turbine using an open jet wind tunnel. *Alexandria Engineering Journal* **55** (3), 2055–2064.

Alaimo, A, Esposito, A, Milazzo, A, Orlando, C & Trentacosti, F 2013 On the effect of slotted blades on savonius wind generator performances by cfd analysis. *energies* **6**, 6335–6351.

Ali, Mohammed Hadi 2013 Experimental comparison study for savonius wind turbine of two & three blades at low wind speed. *International Journal of Modern Engineering Research* .

Altan, Burcin Deda, Atilgan, Mehmet & Özdamar, Aydoğan 2008 An experimental study on improvement of a savonius rotor performance with curtaining. *Experimental thermal and fluid science* **32** (8), 1673–1678.

Bhutta, Muhammad Mahmood Aslam, Hayat, Nasir, Farooq, Ahmed Uzair, Ali, Zain, Jamil, Sh Rehan & Hussain, Zahid 2012 Vertical axis wind turbine–a review of various configurations and design techniques. *Renewable and Sustainable Energy Reviews* **16** (4), 1926–1939.

Bianchi, Fernando D, Mantz, Ricardo J & De Battista, Hernán 2007 *The wind and wind turbines*. Springer.

Bowen, Amy, Huskey, Arlinda, Link, Hal, Sinclair, Karin, Forsyth, Trudy, Jager, David, van Dam, Jeroen & Smith, Joe 2009 Small wind turbine testing results from the national renewable energy lab. *Tech. Rep.*. National Renewable Energy Lab.(NREL), Golden, CO (United States).

Brown, RHJ 1963 The flight of birds. *Biological Reviews* **38** (4), 460–489.

Caplan, Nicholas & Gardner, Trevor N 2007 A fluid dynamic investigation of the big blade and macon oar blade designs in rowing propulsion. *Journal of sports sciences* **25** (6), 643–650.

Carter, Robert 2006 Boat remains and maritime trade in the persian gulf during the sixth and fifth millennia bc. *antiquity* **80** (307), 52–63.

Cengel, Yunus A & Ghajar, AJ 2011 *Heat and mass transfer (a practical approach, SI version)*. McGraw-Hill Education,.

Cooper, P & Kennedy, OC 2004 Development and analysis of a novel vertical axis wind turbine. *Proceedings Solar 2004 - Life, The Universe and Renewables* pp. 1–9.

DAlessandro, V, Montelpare, S, Ricci, R & Secchiaroli, A 2010 Unsteady aerodynamics of a savonius wind rotor: a new computational approach for the simulation of energy performance. *Energy* **35** (8), 3349–3363.

Deb, Bachu, Gupta, Rajat & Misra, RD 2014 Experimental analysis of a 20 twist helical savonius rotor at different overlap conditions. In *Applied Mechanics and Materials*, , vol. 592, pp. 1060–1064. Trans Tech Publ.

Demin, VF 2002 Health and environmental impacts of electricity generation systems: procedures for comparative assessments. *Atomnaya Tekhnika za Rubezhom* pp. 16–19.

EIA, U.S. 2017 U.s. electricity generation by source, amount and share of total in 2017.

Freeman, Janine M 2012 Testing of a combined savonius-darrieus wind turbine. Master's thesis, Rensselaer Polytechnic Institute.

Gasch, R & Twele, J 2012 *Wind Power Plants, Fundamentals, Design, Construction and Operation*. Springer.

Gavalda, Jna, Massons, J & Diaz, F 1990 Experimental study on a self-adapting darrieussavonius wind machine. *Solar & Wind Technology* **7** (4), 457–461.

Gleick, Peter H 2009 Three gorges dam project, yangtze river, china. In *The world's water 2008–2009: the biennial report on freshwater resources*, pp. 139–150. Island Press Washington DC.

Golecha, K, Eldho, TI & Prabhu, SV 2011 Influence of the deflector plate on the performance of modified savonius water turbine. *Applied Energy* **88** (9), 3207 – 3217.

Gupta, R, Biswas, A & Sharma, KK 2008 Comparative study of a three-bucket savonius rotor with a combined three-bucket savonius–three-bladed darrieus rotor. *Renewable Energy* **33** (9), 1974–1981.

Gustavsson, Lars T 2017 Uncertainty Analysis.

GWEC, Global Wind Energy Council 2014 Global wind report: Annual market update 2015. *URL http://gwec. net/global-figures/graphs/.[Accessed May 18, 2017]* .

Hau, E 2006 *Wind Turbines Fundamentals, Technologies, Application, Economics*, 2nd edn. Springer.

Hayashi, Tsutomu, Li, Yan & Hara, Yutaka 2005 Wind tunnel tests on a different phase three-stage savonius rotor. *JSME International Journal Series B Fluids and Thermal Engineering* **48** (1), 9–16.

Howard, Brian Clark 2017 Iran's Centuries-Old Windmills May Soon Stop Turning.

Ingram, Grant 2005 Wind turbine blade analysis using the blade element momentum method version 1.0. *School of Engineering, Durham University, UK* .

Kacprzak, Konrad, Liskiewicz, Grzegorz & Sobczak, Krzysztof 2013 Numerical investigation of conventional and modified savonius wind turbines. *Renewable energy* **60**, 578–585.

Kadam, AA & Patil, SS 2013 A review study on savonius wind rotors for accessing the power performance. *IOSR Journal of Mechanical and Civil Engineering* **5**, 18–24.

Kamoji, MA, Kedare, SB & Prabhu, SV 2009 Performance tests on helical savonius rotors. *Renewable Energy* **34**, 521–529.

Kang, Can, Liu, Haixia & Yang, Xin 2014 Review of fluid dynamics aspects of savonius-rotor-based vertical-axis wind rotors. *Renewable and Sustainable Energy Reviews* **33**, 499–508.

Kumar, Palanisamy Mohan, Ajit, Kulkarni Rohan, Surya, Mohan Ram, Srikanth, Narasimalu & Lim, Teik-Cheng 2017 On the self starting of darrieus turbine: An experimental investigation with secondary rotor. In *Energy, Power and Transportation Electrification (ACEPT), 2017 Asian Conference on*, pp. 1–7. IEEE.

Kumar, Rakesh, Raahemifar, Kaamran & Fung, Alan S 2018 A critical review of vertical axis wind turbines for urban applications. *Renewable and Sustainable Energy Reviews* **89**, 281–291.

Kundu, PK, Cohen, IM & Dowling, DR 2009 *Fluid Mechanics*, 5th edn. Academic Press.

Lindsey, Walter Frank 1938 Drag of cylinders of simple shapes. *Tech. Rep.*.

MacPhee, David & Beyene, Asfaw 2012 Recent advances in rotor design of vertical axis wind turbines. *Wind Engineering* **36** (6), 647–665.

Mahmoud, NH, El-Haroun, AA, Wahba, E & Nasef, MH 2012 An experimental study on improvement of savonius rotor performance. *Alexandria Engineering Journal* **51** (1), 19–25.

Mohamed, MH 2012 Performance investigation of h-rotor darrieus turbine with new airfoil shapes. *Energy* **47** (1), 522–530.

Mohamed, MH, Janiga, G, Pap, E & Thevenin, D 2010 Optimization of savonius turbines using an obstacle shielding the returning blade. *Renewable Energy* **35** (11), 2618–2626.

Moretti, Peter M & Divone, Louis V 1986 Modern windmills. *Scientific American* **254** (6), 110–119.

Mueller, Thomas J & Torres, Gabriel E 2001 Aerodynamics of low aspect ratio wings at low reynolds numbers with applications to micro air vehicle design and optimization. *Tech. Rep.*. NOTRE DAME UNIV IN OFFICE OF RESEARCH.

Muller, G, Jentsch, F & Stoddart, E 2009 Vertical axis resistance type wind turbines for use in buildings. *Renewable Energy* **34** (5), 1407–1412.

Munson, Bruce R, Young, Donald F, Okiishi, Theodore H & Huebsch, Wade W 1998 *Fundamentals of fluid mechanics*, , vol. 69. John Wiley & Sons.

Nedić, J, Ganapathisubramani, Bharath & Vassilicos, JC 2013 Drag and near wake characteristics of flat plates normal to the flow with fractal edge geometries. *Fluid Dynamics Research* **45** (6), 061406.

Ortiz, Xavier, Hemmatti, Arman, Rival, David & Wood, David 2012 Instantaneous forces and moments on inclined flat plates. In *The Seventh International Colloquium on Bluff Body Aerodynamics and Applications (BBAA7)*, pp. 2–6.

Ragheb, Magdi 2011 Vertical axis wind turbines. *University of Illinois at Urbana-Champaign* **1**.

Ragheb, M 2014 Wind energy conversion theory, betz equation. *Wind Energie* .

Ragheb, M & Ragheb, AM 2011 *Fundamental and Advanced Topics in Wind Power*. Intech.

Rao, Jubilee Prasad & Diez, F Javier 2015 Development of a cyclic pitch turbine. In *ASME/JSME/KSME 2015 Joint Fluids Engineering Conference*, pp. V002T34A010–V002T34A010. American Society of Mechanical Engineers.

Rao, Jubilee Prasad & Diez, F Javier 2017 Experimental analysis of a cyclic pitch turbine. In *ASME 2017 Fluids Engineering Division Summer Meeting*, pp. V01BT07A002–V01BT07A002. American Society of Mechanical Engineers.

Rao, Jubilee Prasad, Villegas, Arturo & Diez, F Javier 2016 Theoretical analysis of a cyclic pitch turbine. In *ASME 2016 Fluids Engineering Division Summer Meeting*, pp. V01BT29A008–V01BT29A008. American Society of Mechanical Engineers.

Ricci, Renato, Romagnoli, Roberto, Montelpare, Sergio & Vitali, Daniele 2016 Experimental study on a savonius wind rotor for street lighting systems. *Applied Energy* **161**, 143–152.

Ross, Ian & Altman, Aaron 2011 Wind tunnel blockage corrections: Review and application to savonius vertical-axis wind turbines. *Journal of Wind Engineering and Industrial Aerodynamics* **99** (5), 523–538.

Rourke, Fergal O, Boyle, Fergal & Reynolds, Anthony 2010 Tidal energy update 2009. *Applied Energy* **87** (2), 398–409.

Roy, Sukanta & Saha, Ujjwal K 2013 Review on the numerical investigations into the design and development of savonius wind rotors. *Renewable and Sustainable Energy Reviews* **24**, 73–83.

Sadraey, Mohammad 2009 *Aircraft Performance: Analysis*. VDM Publishing.

Savonius, S.J 1931 The s-rotor and its applications. *Mechanical Engineering* **53** (5), 333–338.

Schubel, PJ & Crossley, RJ 2012 Wind turbine blade design. *Energies* **5** (9), 3425–3449.

Sharma, Kaushal Kumar, Biswas, Agnimitra & Gupta, Rajat 2013 Performance measurement of a three-bladed combined darrieus-savonius rotor. *International Journal of Renewable Energy Research* **3** (4), 885–891.

Shigetomi, Akinari, Murai, Yuichi, Tasaka, Yuji & Takeda, Yasushi 2011 Interactive flow field around two savonius turbines. *Renewable Energy* **36** (2), 536–545.

Singh, Bharat Raj & Singh, Onkar 2012 Global trends of fossil fuel reserves and climate change in the 21st century. In *Fossil Fuel and the Environment*. InTech.

Sumner, D, Sprigings, EJ, Bugg, JD & Heseltine, JL 2003 Fluid forces on kayak paddle blades of different design. *Sports Engineering* **6** (1), 11–19.

Sun, Wei, Gao, Zhenghong, Du, Yiming & Xu, Fang 2015 Mechanism of unconventional aerodynamic characteristics of an elliptic airfoil. *Chinese Journal of Aeronautics* **28** (3), 687–694.

Sun, Xiaojing, Luo, Daihai, Huang, Diangui & Wu, Guoqing 2012 Numerical study on coupling effects among multiple savonius turbines. *Journal of Renewable and Sustainable Energy* **4** (5), 053107.

Tang, Zhi Peng, Yao, Ying Xue, Zhou, Liang & Yu, Bo Wen 2013 A review on the new structure of savonius wind turbines. In *Advanced Materials Research*, , vol. 608, pp. 467–478. Trans Tech Publ.

Timmer, WA & Van Rooij, RPJOM 2003 Summary of the delft university wind turbine dedicated airfoils. *Journal of solar energy engineering* **125** (4), 488–496.

Trevor, L 2017 *Wind Energy Engineering, A Handbook for Onshore and Offshore Wind Turbines*. Academic Press, Elsevier [Links].

Tummala, Abhishiktha, Velamati, Ratna Kishore, Sinha, Dipankur Kumar, Indraja, V & Krishna, V Hari 2016 A review on small scale wind turbines. *Renewable and Sustainable Energy Reviews* **56**, 1351–1371.

Weiss, Samuel Bruce 2010 Vertical axis wind turbine with continuous blade angle adjustment. Master's thesis, Massachusetts Institute of Technology.

Wenehenubun, Frederikus, Saputra, Andy & Sutanto, Hadi 2015 An experimental study on the performance of savonius wind turbines related with the number of blades. *Energy Procedia* **68**, 297–304.

Wu, Bin, Lang, Yongqiang, Zargari, Navid & Kouro, Samir 2011 *Power conversion and control of wind energy systems*, , vol. 76. John Wiley & Sons.

Zhang, Yi, Finger, Susan & Behrens, S 2006 Rapid design through virtual and physical prototyping.

Zhao, Zhenzhou, Zheng, Yuan, Xu, Xiaoyun, Liu, Wenming & Hu, Guoxiang 2009 Research on the improvement of the performance of savonius rotor based on numerical study. In *Sustainable Power Generation and Supply, 2009. SUPERGEN'09. International Conference on*, pp. 1–6. IEEE.